POLITECNICO
MILANO 1863

SCUOLA DI INGEGNERIA INDUSTRIALE
E DELL'INFORMAZIONE

Motorcycle aerodynamics: a CFD study from airfoil selection to winglet design for downforce increase and lap time reduction

Tesi di Laurea Magistrale in
Ingegneria aeronautica

Author: **Giulio Peri, Jonathan Capuana**

Student ID: 928550, 953648
Advisor: Prof. Paolo Schito
Co-advisors: Francesco Fabio Semeraro
Academic Year: 2022-23

Contents

List of Figures

List of Tables

Acknowledgements

We would like to thank first of all Professor Paolo Schito for giving us the opportunity to work in an area in which we are particularly interested and for supporting us throughout the work and helping us promptly. Thanks also go to PhD student Fabio Semeraro for guiding us through the technical and aerodynamic analysis parts. The biggest thanks go to our families for supporting us financially, but most of all, morally throughout our studies, for guiding us as we grew and for always being present in the important moments of our journey; without them we could never have achieved this great goal. Special and reciprocal thanks also go to our thesis partner, as well as longtime friend, companion of passions and life, without whom this work would never have even begun. Last but not least, we would like to thank our long-time friends and university friends, thank you for giving us wonderful times full of fun and unique emotions, even in the worst of times.

Abstract

The work of this thesis consists in analyzing the aerodynamic behaviour of a racing motorcycle. More specifically, the study main focus is the development of an aerodynamic appendix capable of generating high levels of downforce, and the consequences on the aerodynamics and dynamics of the vehicle. Despite the abundance of recent studies on the topic, only a restricted portion of the final results have been disclosed to public domain, due to the racing teams' competitiveness and secrecy. Therefore, this study starts from the fundamentals of the focus-driven design of a brand new winglets, proceeding that to the evaluation of their influence on the vehicle during principal working conditions. Referring to literature available on low Reynolds number aerodynamic and on aerodynamic appendix for automotive purpose, the study begins from airfoil section choice that will be characterized through CFD analysis. Once decreed the most suitable airfoil to the peculiar operating conditions, we proceed with finite winglets design. After analyzing the typical phenomenology of low aspect ratio wings, and comparing that with literature available on the micro aerial vehicle (MAV) and unmanned aerial vehicle (UAV) field, which presents common charactristics to our case study, we did a sensitivity study on some geometrical parameter as aspect ratio, taper ratio, sweep angle and endplates addition.
In the last phase, we analyzed the whole motorbike aerodynamic, comparing results obtained with and without winglets. Force coefficients from CFD simulation was used than in a simplified dynamic model built in Matlab^{TM}. In this way has been possible to obtain an extimation for maximum acceleration and deceleration during rectilinear motion, for maximum speed at mid-corner but also an extimation for lap time. CFD results of whole motorbike were compared with experimental test done by Polimi Motorcyle Factory team in order to validate our numerical model.
This thesis work show that high lift winglets, installed on high power motorbike, can lead to a performance increase during rectilinear motion. Any advantage has been encountered instead during cornering motion. Finally, performance differencies reduce with motorbike power, till they become negative for little displacement motorbike.

Abstract in italiano

Il lavoro di questa tesi consiste nell'analizzare il comportamento aerodinamico di una moto da corsa. Più in dettaglio, lo studio si concentra principalmente sullo svliuppo di un appendice aerodinamica ad alta deportanza e sui suoi effetti sull'aerodinamica e la dinamica complessiva della moto. Negli ultimi anni sono stati svolti molti studi a riguardo, tuttavia, per ragioni legate alla segretezza e alla competitività tra i vari team da corsa, pochi risultati e nozioni affidabili sono stati resi pubblici. Pertanto, il presente studio vuole partire dalle basi, con la progettazione di una nuova aletta aerodinamica specifica per questo scopo, fino a studiarne l'influenza sull'intero veicolo nelle principali condizioni di manovra. Appoggiandosi alla letteratura disponibile riguardante l'aerodinamica per bassi numeri di Reynolds e alla progettazione di appendici aerodinamiche per applicazioni automobilistiche, lo studio inizia con la scelta del profilo alare, che verrà caratterizzato tramite analisi CFD. Una volta decretato il profilo più adatto alle peculiari condizioni operative, si è proceduto alla progettazione della aletta vera e propria. Dopo aver analizzato la fenomenologia tipica delle ali a basso aspect ratio, confrontandola con la letteratura disponibile nel campo dei MAV e degli UAV, che presentano caratteristiche comuni, è stato svolto uno studio di sensitività su alcuni parametri geometrici come l'Aspect Ratio, il Taper Ratio, l'angolo di freccia e l'aggiunta di endplates. Nell'ultima fase, è stata analizzata l'aerodinamica dell'intera moto, confrontando i risultati ottenuti con e senza l'uso delle alette. I coefficienti e le forze ricavati dal modello CFD sono stati successivamente riportati all'interno di un modello dinamico semplificato, scritto tramite il software Matlab^{TM}. In questo modo è stato possibile ottenere una stima dell'accelerazione e della decelerazione massime in moto rettilineo e della velocità massima a centro curva, ma anche una stima del tempo sul giro. I risultati CFD dell'intera moto sono stati confrontati con i test sperimentali in galleria del vento effettuati dal team Polimi Motorcyle Factory, al fine di validare il nostro modello. Questo lavoro di tesi dimostra che le appendici aerodinamiche, applicate a un motoveicolo con elevata potenza, possono portare un aumento di performance durante la fase di accelerazione e frenata. Nessun vantaggio è stato riscontrato invece in termini di velocità massima in curva. Infine, la differenza di performance dovuta alle alette si riduce drasticamente riducendo la potenza motrice, fino a diventare

negativa per moto di piccola cilindrata.

1 | Introduction

Since 2015, in high level motorcycle races, motorbikes are equipped with aerodynamics appendices, which shape is strictly conditioned from technical rules. They are improperly called winglets, a term probably coined by sports journalism.
Aerodynamic analysis around a motorbike presents some peculiarity: first of all, the importance of rider and his position. Different pilot position can drastically change the flow around the motorbike. In many studies, the motorcycle rider is represented as a rather simplified dummy, as in the work from M.Palanivendhan et al. [22], in which they discussed on what causes the limitations in aerodynamics of a motorbike and tried to overcome them by changing its shape; in other cases a more detailed CAD model of the rider was used, as in the work from D. Fintelman et al. [13].
Van Dijck [36] described the evaluation of the aerodynamic forces acting upon a road going sport motorcycle (modified for racing purposes) during a high speed, high lean angle cornering manoeuvre using commercial computational fluid dynamics software. After a characterization of aerodynamic forces in a range of lean angle between 45 and 55, he focused on modifications of windscreen and bellypan to show methods of influencing the magnitude of developed lift and side-force. He observed an increase in aerodynamic drag and lift force proportional to the vehicle's lean angle.
Gerald M.Angle [3] works on motorbike drag reduction by means of using commercial vortex generator that generate counter-rotating vortices. He performed Wind tunnel tests on a full-scale racing motorcycle in a Closed Loop Tunnel obtaining a reduction up to 10% in drag forces. Motorcycle aerodynamic and his performance increase, so, has been studied from different perspectives, however there are few studies in the literature strictly regarding winglets functionality. Therefore, in this work, the aim is to study, from an aerodynamic point of view, the effects of the winglets on whole motorbike aerodynamic and, by means of a simplified dynamic model, have an initial estimation of their dynamic effects. We will not refer to a specific motorbike category or to a specific technical regulation so that we can provide a more general overview on the topic. However, even if no regulation are imposed for this work, we will consider a maximum planform constraint in order to obtain winglets that would be installable on a motorbike without:

- obstruct pilot movement
- obstruct motorbike maximum lean angle
- represent a security risk for the other competitors

for these reasons we will consider a maximum span of 150mm and a mean aerodynamic chord of the same length.

1.1. History of motorcycle aerodynamics

As we can imagine, in motorcycle racing, aerodynamics plays a fundamental role, especially when it comes to speed races. For this reason the various teams and manufacturers throughout history have tried to adopt solutions from which they could benefit in terms of speed and performance increase. In the early years when aerodynamics began to be considered, manufacturers focused on making fairly simple fairings that covered as much as possible the rider, the chassis and mechanical parts in order to obtain a wake as clean as possible. This solution was banned in 1957 by the FIM and, in fact, these huge fairings gave the pilots problems in terms of freedom of movement especially in making the curves. Moreover this kind of fairings was dangerous in case of lateral wind. Therefore, the use of less bulky fairings became more traditional, so-called 'dolphin' as we see in figure 1.1.

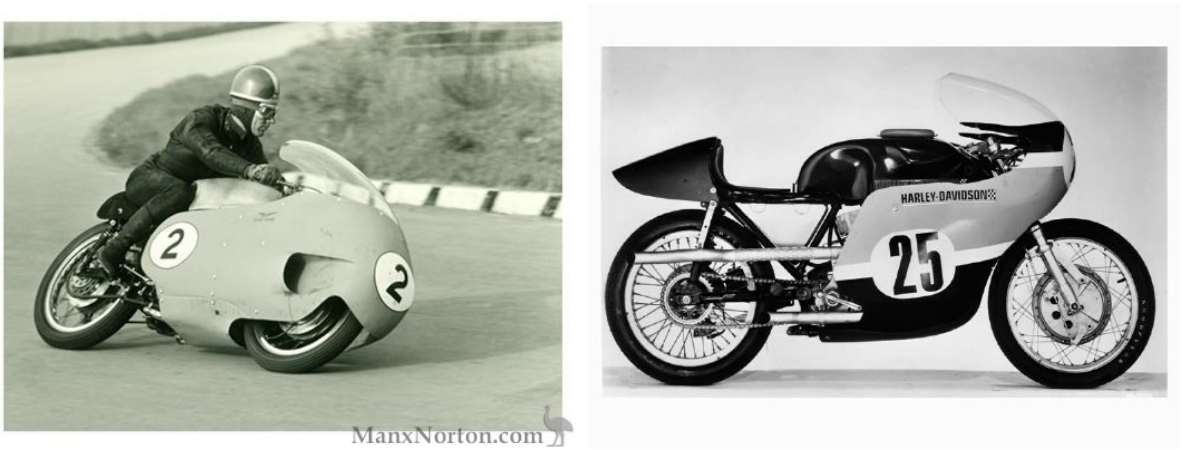

Figure 1.1: 'dustbin' VS 'dolphin' fairing

It is therefore clear that the solutions adopted so far penalize the driving dynamics in corners in order to reach higher top speeds in straight lines. However, from the figure below that represents the map of the famous Assen circuit of the world championship Figure 1.2, we can see how great part of the track is made up of corners, especially considering the fact that the curves of the circuit do not absolutely coincide with the trajectories that the pilots perform. In fact they use, as much as they can, the width of the track in order to 'stretch' the curves increasing curve radius, anticipating the beginning of the corner and posticipate the exit. As a result they run across most of the straight parts of the track with leaning with the bike. It is therefore thought that aerodynamics can help, by positioning wings, that create downforce, to increase cornering speed.

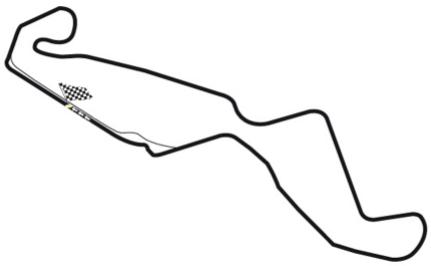

Figure 1.2: TT Circuit Assen

Naturally, when a motorcycle is leaning, the force generated by the wings is then decomposed in a radial direction to the curve and normal to the ground (1.3).

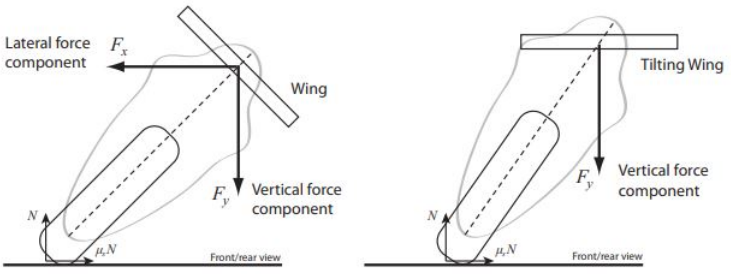

Figure 1.3: Winglets force decomposition on ground axes

According to the leaning angle these two components play an opposite role: the higher the leaning angle, the greater the radial component, helping thus the loss of grip and a possible crash. In the following photo we find one of the first ailerons solutions mounted on a motorcycle that had the intent of generating downforce and therefore cornering grip and traction. This is the case of Rodger Freeth's Yamaha Tz 750 from 1977 (Figure 1.4). Probably in those years the lean angles were not as exasperated as they are today,maybe not even going to scratch the knee on the ground. In this way the normal component to the ground was predominant. Many have also thought of untie the behavior of the wing from the lean angle of the bike, by mounting these aerodynamic appendices on gyroscopic devices that kept the wing horizontal even when the bike is leaning. However, despite this was not allowed by the competition regulations for safety reasons, it would have led to high complications in the design and assembly.

Figure 1.4: Yamaha Tz 750 1977

Throughout history we find other examples of using aerodynamic devices to improve performances. Suzuki tried to mount in 1979 some small wings on the front part of the fairing of the suzuki RG500 of the famous Barry Sheene (Figure 1.5). These devices were used to reduce the lift that the motorcycle made at high speeds, causing a lightening of the load on the front, which led to an instability of the bike on the fast straights. This type of device can also be found on the BMW R1000RS (1977). Suzuki, however, soon gave up this idea because it compromised too much handling in curves.

Figure 1.5: Suzuki RG500 1979

Ducati (Figure 1.6) also tried to adopt a similar concept in 2009 towards the end of the season but again the idea was abandoned in the winter tests of the following years. As regards the latter, some not official statements affirm that these wings also performed another purely thermodynamic function: the assembly of these fins would create a vacuum by increasing the flow of air through the water and oil radiators thus reducing the operating temperatures of the engine.

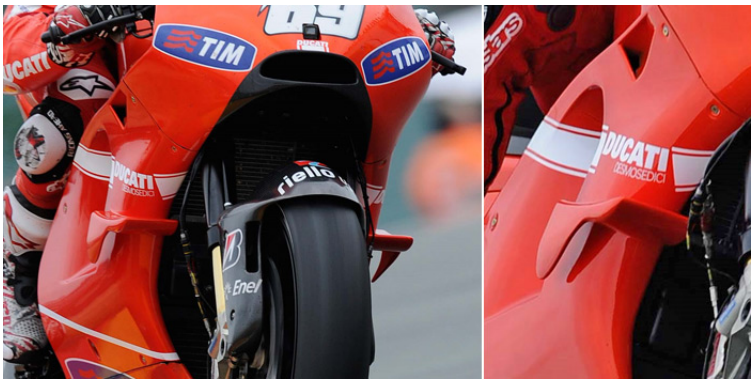

Figure 1.6: Ducati DesmosediciGP 2010

1.2. State of the art

In recent years, in the racing departments of all motorcycle manufacturers has been given an additional boost to aerodynamics developments, consistently increasing the budget devoted to this sector. Economic availability for aerodynamic research is however much less than the one available in automotive case, but still sufficient to complete an accurate development cycle, which, briefly, develops as follows:

- high fidelity method as computational fluid dynamics (CFD)
- wind tunnel testing
- road test, in the circuit or airports

Numerical simulations, as in many other areas, are used mainly during the design of a new component, such as fairing or aerodynamic appendices, in order to be able to make some preliminary choiches, avoiding a too much intensive and costly use of wind tunnel. In fact, wind tunnel experiment, involves not only the cost of the wind tunnel itself, but also the cost of model or component realization that, in case of motorbike fairings, is almost always made with composite material. Concerning wind tunnel testing, full scale model are usually used and three different types of activities take place: validation of cfd model, visualization and data acquisitions and, finally, pilot training. Validation of CFD model, until recently, was done without any riding pilot or mannequin because of the difficulties encountered in obtaining a reliable CAD model. Only in recently years, through the use of 3d-scanner some progress in that field was done. It is however very difficult to have a realistic scan during cornering motion because pilots encounter some difficulties in maintaining the correct position when lateral acceleration is not present. To overcome this problem, Ducati Corse, the racing division of Ducati, is developing a complex sensorized motorcycle suit that, through the use of accelerometers, can reconstruct the movements and the position of the pilot during a real ride. Regarding data acquisition, particular interest is given to forces and moments, velocity, in particular for internal aerodynamics, and pressure. Some examples are reported in next figure.

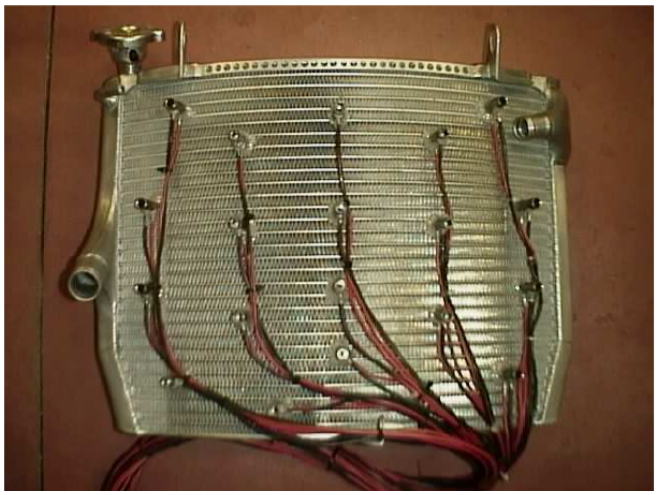

(a) Experimental setup for radiator velocity measurement

(b) Experimental setup for pressure field measurement on frontal fairings

Figure 1.7: Examples of experimental setup for motorbike wind tunnel tests

Concerning visualization, most used techniques involves both the use of woolen threads to visualize on-body streamlines both smoke wire visualization, as in next figure

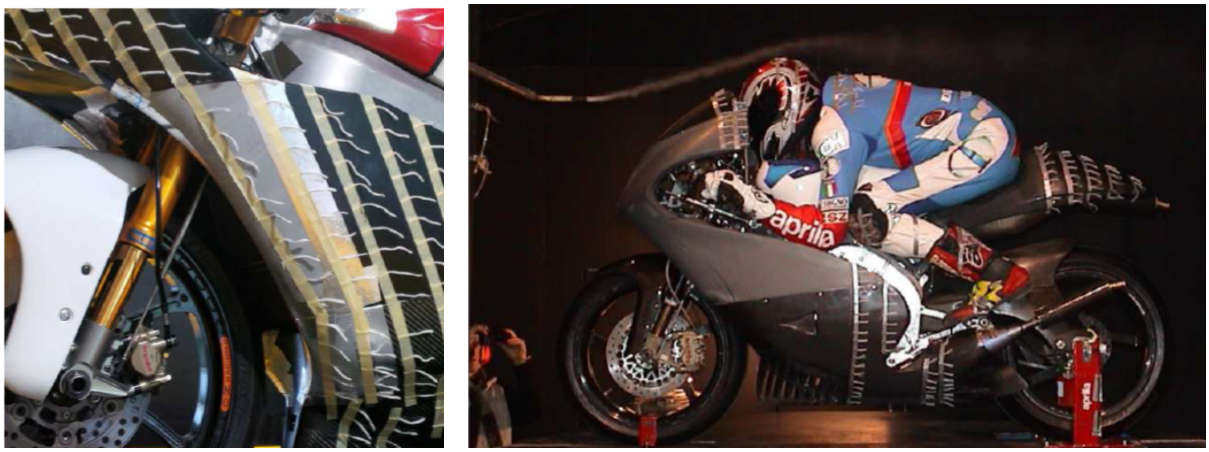

Figure 1.8: Example of experimental setup for flow visualization on motorbike fairing

Last kind of wind tunnel activity, as said before, is pilot training. During this training, pilot, with the aids of the engineer, looks for the position that guarantee less drag force. In motorbike dashboard is usually report the forces output from the balance, so that pilot can read it in real time.
Minimum drag position can be tested also in airport runway with the aids of photocells and possibly a weather station to monitor wind direction and intensity.
Last step of designing process is to test on a real circuit. In this phase pilot can give

to engineers a feedback on the handling of the motorbike and can also approve or reject the changes made. It is not uncommon for the pilot to discard some solutions that in preliminary tests seems to be a possible source of improvement.
Thanks to the methodology just presented, some advances in therms of aerodynamics was done. One of the most relevant result obtained is the re-introduction of winglets. In 2015, for the first time, Ducati starts to adopt aerodynamic appendices applied to the fairings in a more consistent way, stimulating the other teams to follow this path and leaving plenty of room for the imagination of the engineers who began to test wings of increasingly complex shapes. Soon in 2019 FIM wanted to ban the use of fins from Gran Prix competition, also because some pilots had complained saying that they were dangerous and calling them 'knives'. In fact, from the 2019 season it was possible to continue to use the fins as long as they were an integral part of the hull checked and approved at the beginning of the season. In other competition such as Superbike instead, there is still much more design freedom.
As the engineer Giulio Bernardelle (former Technical Manager of the 500 class Team) explains in an interview, these fins serve to better distribute the downforce between front wheel and back wheel, similar to what the ailerons do in Formula 1. Due to the way the MotoGP fairings have been made up to now, at high speed the aerodynamics tend to unload the front wheel and load the rear wheel. This generates an unbalanced load of the bike, which changes according to the speed. The fins allow you to find the load on the front end much more effectively, also allowing you to profile the rest of the motorcycle fairing for the purpose of improving the penetration coefficient. With the wings, therefore, a better fairing can be designed in terms of aerodynamic resistance, without this leading to shifting the aerodynamic load towards the front.
Vojtech Sedlak conducted some studies, looking for an improvement also at high lean angle. [25] During cornering motion, rider changes is position, moving towards the center of the curve and opening the internal leg (the one nearest the center of the curve) till the knee touch the ground. This position change affects flow field around the motorbike and may disturb the internal winglet. If pilot is capable of "deactivate" the internal wing it is possible to install winglets with a negative dihedral angle so that the external wing, during cornering, will be placed horizontally and will generate a pure vertical force, instead the internal one will be place vertically but will not produce any horizontal force thanks to pilot interaction, as in next figure extracted from [25].

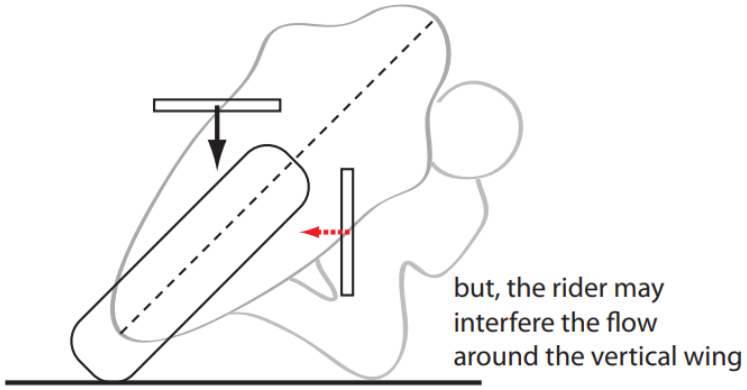

Figure 1.9: Concept of dihedral angle an rider interference

In this way winglets can be beneficial also in cornering motion.
To evaluate this interference he proceeded with a CFD preliminary 2d study in which a circular geometry was placed behind an airfoil and evaluating the interaction between the two bodies, varying main geometric dimensions as circle radius and position with respect to the airfoil and the airfoil angle of attack. He did also a simplified 3d study placing behind a simple rectangular planform wing, once a rounded cilinder and once a flat semi infinite cigar. Also a preliminary cfd on whole motorbike was done, using this concept of dihedral angle but numerical results are not reported.
Because of the strong confidentiality of all racing teams no other literature is available strictly concerning motorcycle winglets. However a more general view on works done in the field of automotive application can be useful to lay the foundation for our thesis work. We start from a general view of motorsport aerodynamic problems and difficulties, than we analyze some previous works on high lift airfoil design and finally we will pass to 3d, low aspect ratio wings, presenting some works done in MAV field, in which Reynolds number and aspect ratio are similar to the one of our problem.

1.2.1. Aerodynamics for motorsport application

Transferring the design methodology for high-lift wings directly from the aerospace world to motorsport applications involves some difficulties and is not such an immediate job. Several issues arise when trying to do this work. The Downforce that helps both cars and motorcycles to improve traction and grip, in general, can be created by modifying the shape of the vehicle itself, as in the case of cars (exploiting the ground effect) or in the case of motorcycles, by mounting wings that have the same task. A first aspect that must be considered is their narrow range of action compared with that of aircraft

wings. Furthermore, their shape cannot be free like that of airplanes because they often have to satisfy the constraints that the racing regulations require. Many or all of these wings are optimized for maximum lift. However, as explained in the report [16] these profile optimization techniques cannot be directly transferred to the wing construction as the aerodynamic behavior of a profile results very different when analyzing its wing in a complex three-dimensional flow that flows around the vehicle itself. In fact, some non-negligible aspects must be taken into account:

- The strong influence of the ground effect, especially in the field of cars, where the front wings are mounted very close to the asphalt. Many racing cars, especially with open wheels such as Formula cars, have ailerons placed in front of the wheels and very close to the asphalt. This type of configuration, if we think about it, is not at all common in aircraft. The Figure 1.10 below shows the pressure distribution of a two-element aileron. The wing is positioned at two different heights from the ground (h/c = h/c = 0.3, Aspect Ratio 4.7). The difference that is created in terms of pressure distribution is very significant only by approaching or moving the wing away from the ground. This problem does not really interest our study in fact the wing on the bike will be positioned not particularly close to the asphalt, however there could be an influence of this type when the bike leans, bringing the wing very close to the ground.

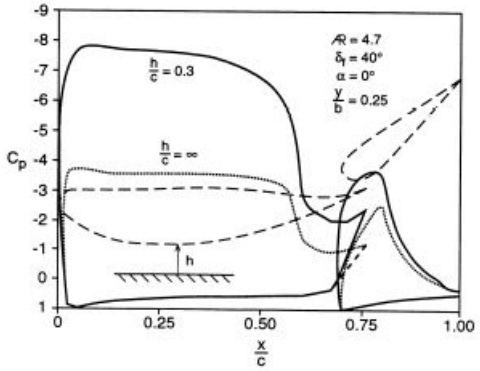

Figure 1.10: Ground effect on a open-wheel front wing

In Figure 1.11a, on the left, we see the pressure distribution of a wing consisting of two elements positioned in the undisturbed stream and mounted on the car. It is interesting, in this case, to note how the Cp trend of the queued profile practically does not undergo any changes. This tells us that when we have to make any changes to an 'airplane type' profile in a wing consisting of two elements, these changes must be made mainly on the main element. In Figure 1.11a, on the right, instead we

see how the interaction with the vehicle body changes the lift distribution along the wing, compared to the free wing case. In this case, for example, the flow is in fact diverted from the rear wheel fender, increasing the angle of attack on the wing tip. Consequently, the induced drag induced at the tip of the wing with respect to the center also increases.

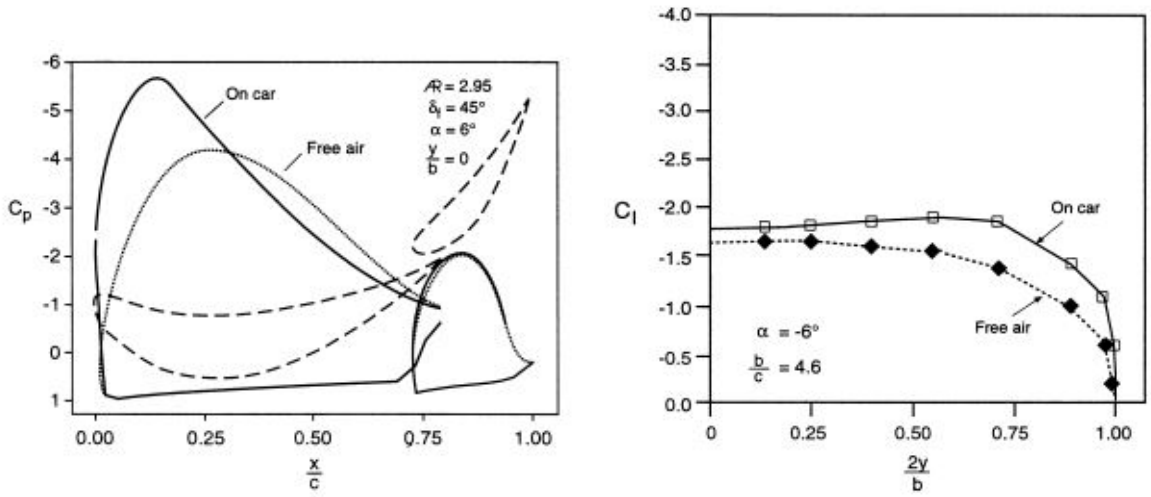

(a) Comparison between pressure distribution of 2-element wing installed on the car and in uniform flow

(b) Comparison between Cl distribution of 2-element wing installed on the car and in uniform flow

Figure 1.11: Comparison between wing behaviour installed on a car and in uniform flow

- The strong interaction between the wing and the components of the vehicle/driver himself. The second important difference between the design of a wing for an airplane and one for motorsport concerns the different interaction they have with the body of the aircraft/vehicle itself. On a car/motorcycle, the wing must interact with the complex three-dimensional flow that is created around the geometry of the vehicle itself. This is very different from aerospace where the current lines around the aircraft fuselage are rather straight and tidy.The Figure 1.12 plots the pressure distribution of the center line section of a wing mounted on the 1991 Mazda RX-7 GTO. The 'Free air' line represents the pressure distribution of the wing positioned in a totally undisturbed flow. The other line is the pressure distribution of the wing mounted on the car. The difference is really marked! This is mainly due to the deviation of the air flow that passes over the roof creating the Downwash effect.

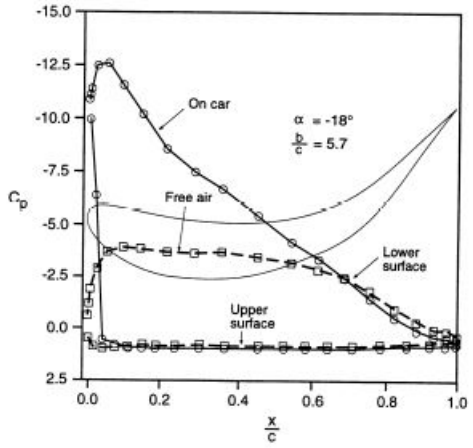

Figure 1.12: Comparison between pressure distribution on the car and in undisturbed flow

- The influence of low Aspect Ratio on the pressure distribution on the wing. In the Figure 1.13 the pressure as a function of the chord is plotted by comparing a 2d profile (infinite wing) with a low aspect ratio (AR1.9). While in the 3d case the flux on the wing is attached if we look at the graph of the 2d case we notice a peak of Cp that reaches -12 (potential flow) at the leading edge, this induces a separation. We can therefore conclude by saying that a wing cannot be drawn based exclusively on specific techniques for 2d studies. In fact, a potential profile optimized for 2d and used for a low Aspect Ratio wing would give us a very different pressure distribution and all the benefits obtained by optimizing it in 2d would then be lost.

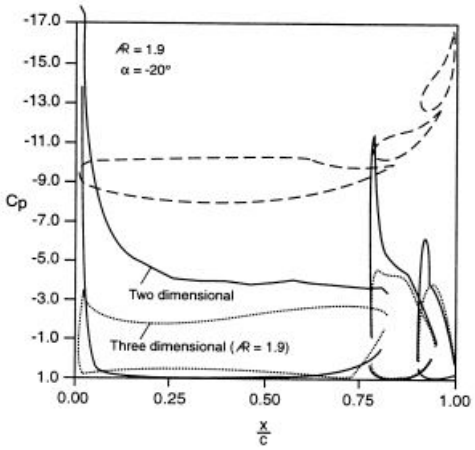

Figure 1.13: Comparison between pressure distribution on AR 1.9 wing and 2d profile

We have therefore seen how the use of wings in motorsport requires some precautions in the design and planning phase. We have listed with various examples previously illustrated some of the major problems affecting the use of wings on ground vehicles. Some of these will interest our study, others less, but in any case it was worth it to present all of them. We have also seen that if we start to build a wing with an apparently excellent profile in the two-dimensional case, the performance and behavior change radically by going into a three-dimensional flow.

1.2.2. Airfoil design method for high-lift and low Reynolds numbers

P. Sriram et al. in their work [33] illustrate techniques and design methodology for high-lift profiles for ground vehicles purpose. In particular, for designing high lift wings for motorsport, they focus on the aft loading technique. In the first part of their work the aft loading method is presented and a high lift profile is shown, highlighting strengths and weaknesses when it comes to vehicles applications. The use of PROFOIL [27] has been fundamental for this report, in fact several geometries has been generated and then tested by XFOIL. Unlike aircraft-oriented high-lift airfoils, the constraints of the pitching moment can be eliminated and this allows more design freedom in the pursuit of downforce. The stern loading also guarantees high consistency in performance over a wide range of angles of attack. As mentioned before, an aerodynamic profile with these characteristics was designed by PROFOIL for low reynolds numbers, obtaining a maximum Cl of 2.5 at Re 300000. At the beginning, profiles already developed for various aeronautical areas for low Reynolds numbers such as low speed aircraft are presented. These profiles

were designed taking into account the approaches presented by Liebek[1], Worthmann[40], Eppler[12] and Selig[26].

To study the applicability of 'aft loading', we must first compare some of these existing high lift profiles for low Reynolds numbers and analyze their differences. It is well known by Selig that as pitching moment increases, maximum lift coefficient increases along with the pressure recovery becoming convex, as is represented in Figure 1.14. Other observable trends from the same figure indicate that, as an airfoil tends towards a more concave loading, high lift is achievable along with an increase in the rapidity with which stall is reached. Two distinct methodologies were developed in the quest for high lift. Several Liebeck airfoils are good examples of the first type where a large rooftop suction level is employed followed by a Stratford pressure recovery (or concave pressure recovery)[11]. This leads to hard stall characteristics and high lift with low pitching moment. The second approach is that used by the some of the Wortmann airfoils where the suction peak is reduced and more emphasis is placed on aft loading (convex pressure recovery) in order to provide softer stall characteristics.

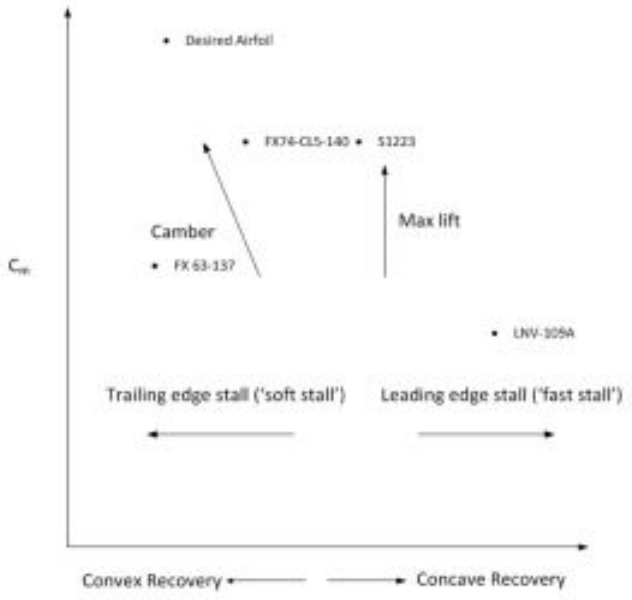

Figure 1.14: Schematic of airfoils lift and stall trends as function of pressure recovery type

A third methodology is reflected by the Selig and Eppler high lift airfoils where a combination of the two philosophies is utilized to provide high lift at low Reynolds number. The Liebeck airfoils rely on a Stratford boundary-layer inverse solution whereby a pressure recovery distribution can be found that continuously avoids separation of the turbulent boundary layer. It is meant to recover the maximum possible pressure rise in the shortest

possible distance. The Stratford recovery also represents the best distribution to obtain an excellent aerodynamic efficiency. However, these profiles are characterized by a high sensitivity of the boundary layer on the back from imperfections. This is a problem as there are many agents on the track (such as dirt and small stones from the asphalt) that could ruin and scratch the back of the wing. Furthermore Stratford recovery causes a very fast stall (hard stall). In the context of motorsport, precisely because the vehicle continues to accelerate and brake, we see a very high range of Reynolds numbers (from 200,000 to 600,000 for example for Formula SAE). This change in terms of Re causes an increase in adverse pressure gradient, which then causes a fast moving of the turbulent separation point. Eppler suggested that a Stratford-like pressure distribution is too excessive and the profiles should have had a more concave pressure distribution.This forms the basis for Eppler's and Selig's high lift airfoil designs where a moderated degree of concavity is allowed into the pressure recovery along with aft loading. Another feature concerns the fact that a wing mounted on a vehicle does not see as much variation in terms of angle of attack however it is necessary that the wing has a sufficiently high range of action in order to give many more possibilities to the track engineers in assembly phase. The low aspect ratio also determines that most of the drag is due to induced drag. Therefore, the drag of the profile is much lower than the overall drag, this in fact allows during the design phase to focus mainly on maximizing the downforce (and therefore the Cl) and not so much on efficiency. In fact, the goal is to obtain a profile that has high lift values for a high range of angles of attack. Therefore a Stratford type distribution profile is not the ideal solution for motorsport. Wortmann's approach with the FX-63-137 consisted of aft loading with more gradual initial gradients. The design approach with this airfoil was to increase Cl max primarily by adding pitching moment. This gives the FX63-137 a convex pressure distribution, as seen in Figure 1.15b. Eppler showed that the lift of an airfoil with concave recovery could be improved using aft loading and this was meant to espouse both concave pressure recovery and aft loading as a means to enhance high lift performance. An example of this design direction is the Wortmann FX74- CL5-140 Figure 1.15d. Selig adapted concave recovery and aft loading to produce airfoils optimized for high lift at LRN. The S1223, shown in Figure 1.15c, produces the maximum lift currently for airfoils operating in this regime.

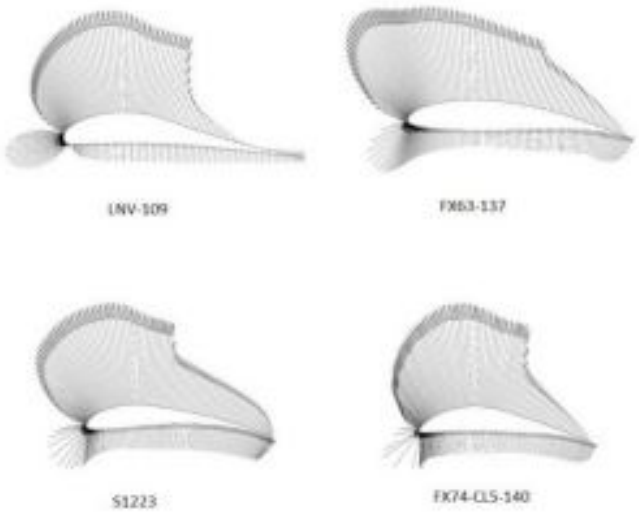

Figure 1.15: Pressure distribution profiles for different airfoils

The approach of Selig Worthmann and Eppler has led to excellent results by generating profiles with a high maximum lift coefficient, however, due to some constraints of the aeronautical world, an approach more consistent with our case by eliminating these last constraints can lead to the generation of a dedicated profile for the motorsport sector. This approach eliminates any pitching moment constraints imposed in previous designs and attempts to use aft loading as the chief driver towards maximizing downforce while maintaining a rudimentary level of concave pressure recovery that has been kept gradual to ensure airfoil stability under varying operational conditions.

The metodology used in the referred report [33] led to the birth of the single-element MSHD (Motor Sport High Downforce) airfoil shown in Figure 1.16 of which we summarize the characteristics:

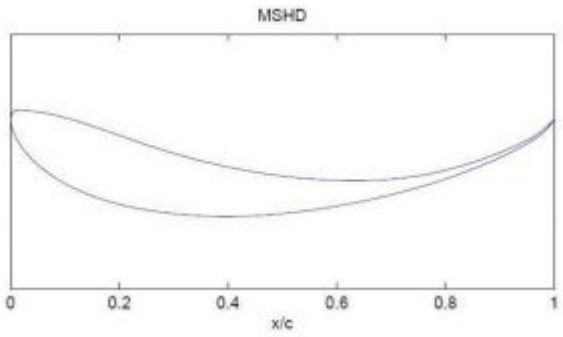

Figure 1.16: Representation of single element, high downforce airfoil for motorsport application: MSHD

- Extension of aft loading to increase downforce
- Characteristics of 'soft stall'
- High leading edge radius to prevent the formation of LSBs even at high angles of attack
- Correction of the profile thickness to shift the adverse pressure gradient forward and minimize the dependence on the laminar boundary layer
- High downforce even with trailing edge gaps
- Consistency of performance even in case of surface scratching from external agents
- Performance as similar as possible over a high range of angle of attack and Reynolds

1.2.3. Theoretical background on finite wing

A wing can generate lift by having, on the upper surface, a suction side, in which low pressure is achieved, and a pressure side on the bottom. This pressure difference generate, however, a secondary effect: the flow near the wings tips is forced by the high pressure field to curl around the tips. Downstream of the wing two counter-rotating vortex is formed, named tip-vortex. The flow field becomes highly three-dimensional, especially on the tip region of the wing, modifying the wing performances compared to the 2D case. Moreover an induced downward velocity is experienced, forming an induced angle of attack that we will call α_{ind}.
Furthermore an additional drag force, called induced drag, must be experienced by a wing of finite span. [2]
Another peculiar characteristics of a finite wing is the reduction, if compared with 2d airfoil section, of the slope of the Cl curve. The first attempt to quantitatively model such a phenomena was made by Prandtl with the classical lifting-line theory, that we report in Appendix A **??**. It is necessary to remark that the classic lifting-line theory is linear, i.e. the relation $c_l = f(\alpha)$ is linear. This could be a good approximation at low angle of attack but at pre-stall angle a strong assumption is done. A non linear version of lifting-line theory was implemented and have been found to agree much closer with experimental data at high angle of attack.
Very important is to understand the limitation of this theory. *The calculations are subject to the limitations of lifting-line theory and should not be expected to give accurate results for wings of low aspect ratio and large amounts of sweep.* [29] Since, as specified before, we are dealing with wings with aspect ratio equal to 2, flying at low/moderate Reynolds number, more detailed analysis is required.

1.2.4. Low aspect ratio wings at low Reynolds number

As said before this case study is quite particular and strictly related to this application and there is little literature about that, however lot of studies was made in fields that has some analogy with our case.

Particular attention to the tip vortex structure and influence was given in helicopter blades field because the trailing vortex from a rotor blade can be a relevant source of noise and vibration. Since there is some evidence [35] that the structure of vortices created by a rotor is basically the same generated by a fixed wing and centrifugal effect are negligible [32] .) we can extract some analogy between a low aspect ratio wing and the tip region of

a rotorblade. McAlister et Takahashi in their work evidenced that *the streamlines on the suction side, near the trailing edge, will be driven in outboard direction under the action of the vortex. This vortex also causes the pressure to be reduced on the surface of the wing beneath it and is therefore responsible for an increase in lift in this region. As a result The lift distribution (from pressure integrations) diminishes along the wing span as the tip is approached, but exhibits an abrupt increase over the outermost 4% of the wing in tip zone* [19]. In this work were analyzed three different AR and the least of all was 6.6, with a Reynolds equal to 1×10^6. Pressure measurements were made in upper and lower surfaces of the wing and then integrated to obtain a lift estimation. In the first stage, 12 span-wise station along the all wing were analyzed. In the following image 1.17 from [19], lift distribution along the span is presented for different AoA that confirmed the trend mentioned before.

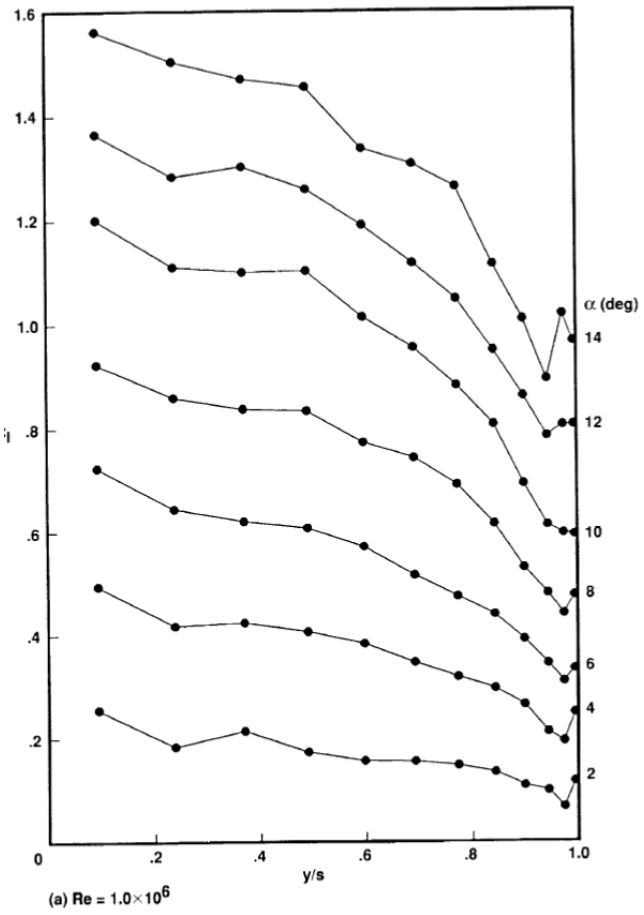

Figure 1.17: Cl span distribution on a 6.6 AR wing at different AoA [19]

For all the AoA there is a gradual reduction of the lift moving to the tip, but, at the end of the wing an increase of Cl is highlighted. Back along the span, near the root of the wing, the lift reach an asymptotic value, except for a slight increment due to the supporting

endplate.
For better understanding, pressure coefficient along the 12 analyzed chord at 12° AoA is reported in the next figure. 1.18

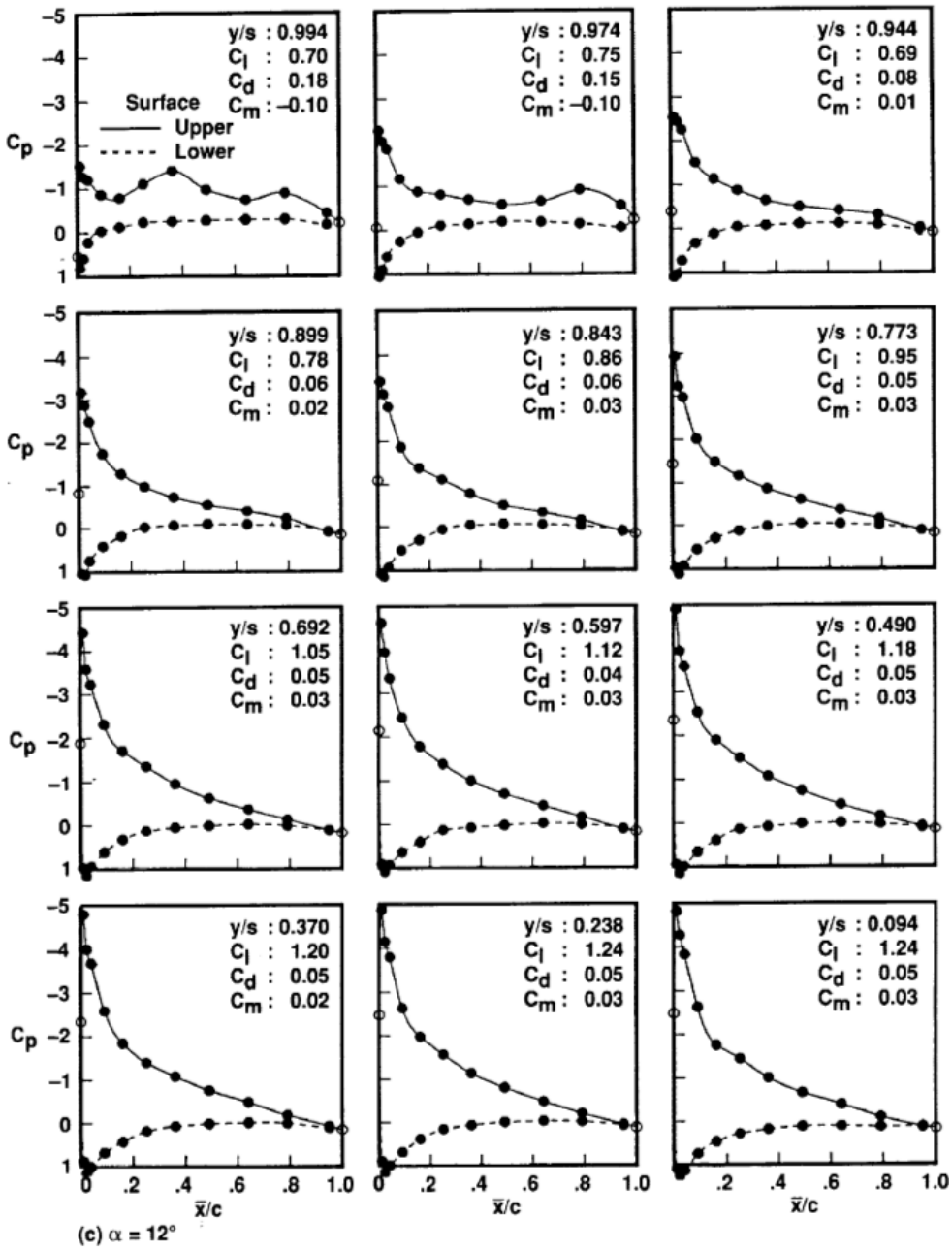

Figure 1.18: Pressure coefficient at different spanwise station for a 6.6 AR wing at 12° AoA

Moving to the tip we can clearly see, for all conditions, a gradual reduction in pressure and a distortion in the chord-wise pressure distribution over the upper surface. *This*

distortion is believed to be due to the tip vortex that forms on the suction side of the wing tip. [19] The literature just presented differs from our fields of application because the higher Reynolds number and the higher AR. As said before no much research have been done with our specific setup but there is another interesting field in which, as opposed to what we analyzed before, Reynolds number is lower than our case study. This field of interest is that of unmanned aerial vehicles (UAV) and micro air vehicles (MAV). Genç et al. conducted an experimental analysis of low aspect ratio, Naca 4421 wing at low Reynolds number (50000). [14] They found, thanks to smoke wire visualizations and forces measurements that *the effect of tip vortexes increased while aspect-ratio of wing decreased. Maximum lift coefficient and stall angle considerably increased as aspect-ratio was less or equal to 1.*[14]. Confirming this, they found that the value of maximum lift coefficient is 1.35 and stall angle is 38° for AR=1 at Reynolds number of 50000 instead the maximum lift coefficient is 1.25 and stall angle 14° when aspect-ratio has been increased from 1 to 3. Another important result is that the tip vortex starts forming, along the cord, at a position that strictly depends from the AoA as shown in next figure.

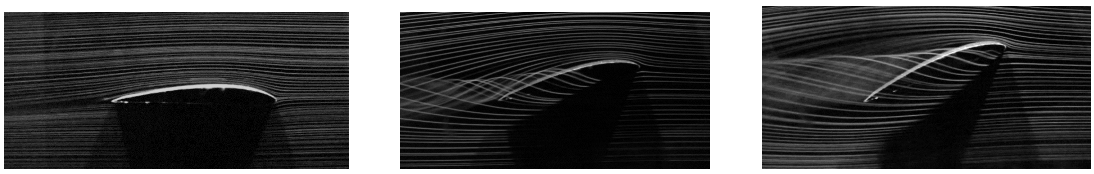

(a) 0 deg AoA. (b) 16 deg AoA. (c) 24 deg AoA.

Figure 1.19: flow visualization with smoke-wire test at Reynolds number of 50000 for AR = 3 and z/c = + 0.1

A study similar to that done by Mcalister and Takahashi [19] was done by Sathaye et al. [24] in which they measured pressure coefficient on different station along the span and the lift distribution of a AR 1 Naca 0012 wing at lower reynolds number. Results are similar to the one obtained from Mcalister and Takahashi. At the tip of the wing is present the same pressure reduction and distortion. In the next figure we report their Cp results for measurements done at $Re = 84122$ and $AoA = 15°$ at 93.75% of the span.

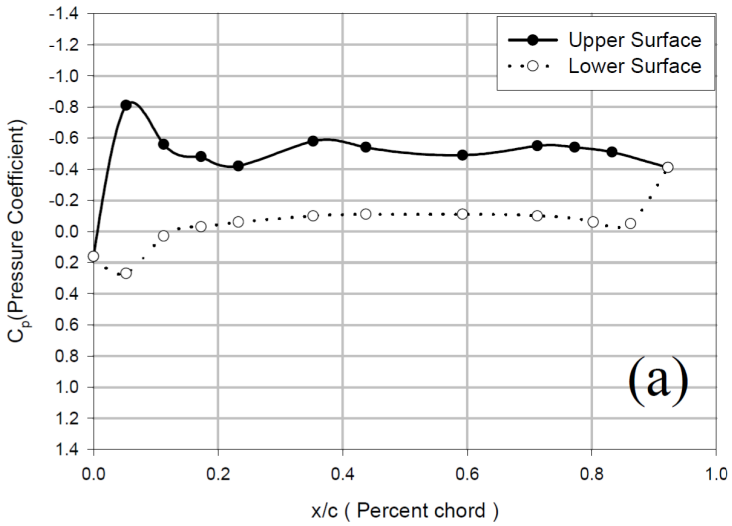

Figure 1.20: Cp vs x/c plots for Re = 84122, $\alpha = 15$ near the tip

Furthermore the lift distribution, also in this case, presents a peak near the tip at all the AoA tested. Results for $Re = 84122$ are reported in next figure:

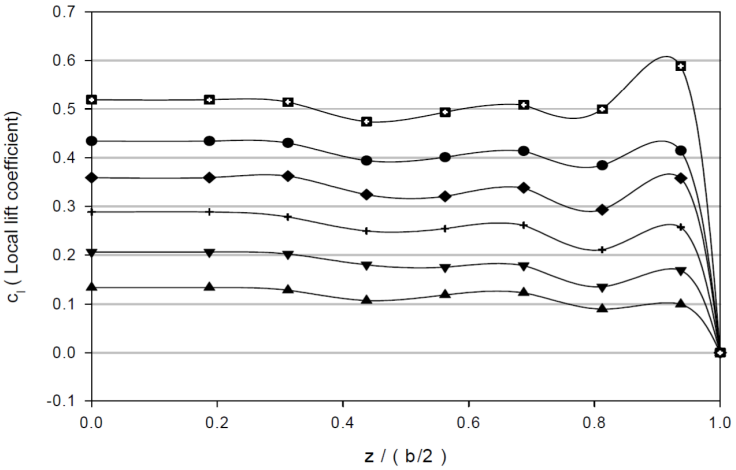

Figure 1.21: Lift distribution plots at Re = 84122

A relevant difference between the lift distributions in figure 1.21 and figure 1.17 is that, except in the peak area, the lift coefficient of AR1 wing is fairly constant along the span and do not present, moving toward the root, the significant increase present in the AR6.6 wing.

An extensive study on AR and planform influence was done by Torres and Mueller. [34] They found that the aspect ratio is the most relevant parameter on the aerodynamics

of low aspect ratio wings and, as clear in figure 1.22, notable change appears when AR become less then 1.5. We report their results for rectangular planform at $Re = 1 \times 10^5$

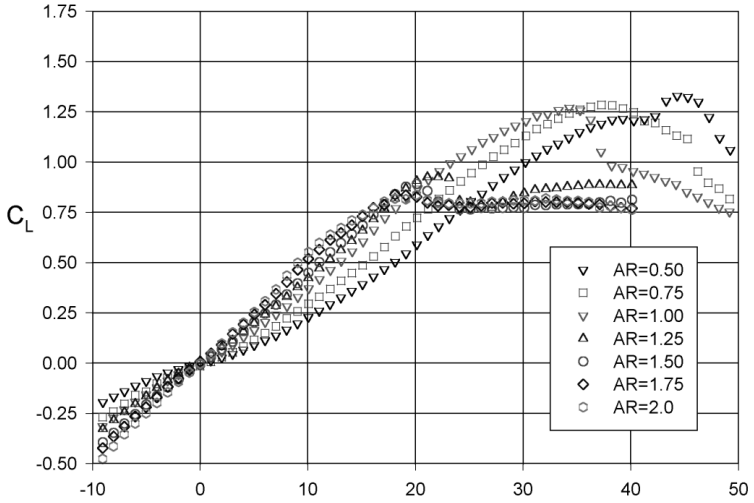

Figure 1.22: CL- α for rectangular planform wing of different AR at $Re = 1 \times 10^5$ [34]

We can clearly see a radical change in the behavior of $Cl - \alpha$ curve when AR decrease above 1.5:

- the $Cl - \alpha$ curve becomes non-linear and this is supposed to be due to the presence of the tip vortex
- stall angle dramatically increase
- maximum Cl continues to grow until about 35% more than the one reached from a AR2 wing

They also compared the lift slope of their experimental results with the one obtained both from classical lifting surface theory, both with the equation proposed by Lowry and Polhamus. In their work, Lowry and Polhamus proposed a correction of lifting surface theory in order to have a better accuracy in predicting lift slope for low AR. [17]

$$Cl_\alpha = \frac{2\pi AR}{2 + \sqrt{(\mathrm{AR}^2/\eta^2)(1 + (\tan \Lambda_{c/2})^2) + 4}} \tag{1.1}$$

where $\eta = a_0/2\pi$ and $\Lambda_{c/2}$ is the sweep angle at midchord.
Another proposal of modelling lift slope for thin, rectangular wing with $AR \leq 2.5$ is the

one from Hoerner and Borst [6]

$$Cl_\alpha = \frac{1}{36.5/AR + 2AR} \tag{1.2}$$

Sticking to the field of MAV, the need to obtain higher lift value and higher lift to drag ratio led to the development of contrivance that would reduce the negative effects of the tip vortex. Among all these we will focus on end plates. The main purpose of the end plates is to obstruct flow movement from higher pressure size to low pressure side. Viieru, Albertani et alter [37] conduct a numerical studies that concern simple rectangular end plates, as in figure 1.23 installed on a $AR \approx 1.5$ wing at $Re = 9 \times 10^4$.

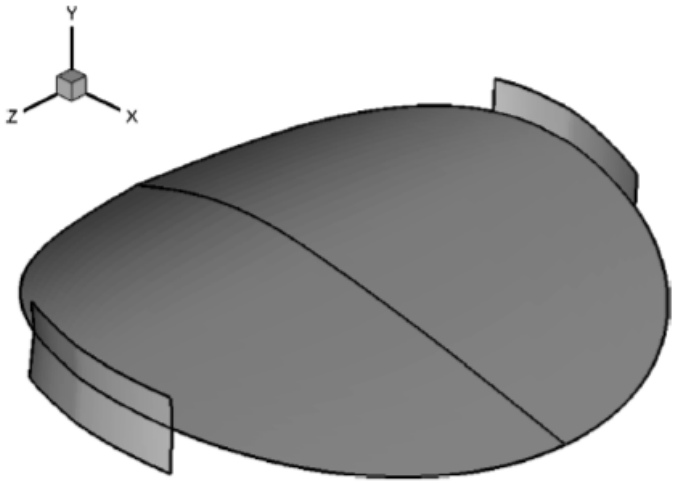

Figure 1.23: Wing geometry with end plates [37]

They experienced a reduction of the vertical velocity induced by the tip vortex, near the wing tip and an increase of the lift, at low angle of attack, without a significant increase in drag. The increase in lift, due to the end plates, is more relevant near the wing tip, where the end plates reduces the flow from pressure side to suction side. An higher pressure is reached on the lower surface of the wing, taking to the lift increase said before. When the AoA becomes higher, and so the vortex effects become greater, the end plates seem to be ineffective, untill they becomes underproductive for very high angle of attack. As we said before, in low AR, a not negligible part of the lift is due to the low pressure induced on the upper surface of the wing. By the use of an endplates also this phenomena is attenuated, the endplate is effective only if it can create a region of high-pressure on the lower surface of the wing to compensate for the low-pressure region generated by the wing tip vortex as the angle of attack is increased. Lot of geometry were tested, instead of a flat plate, and

a proper optimization could take consistent advantages in terms of drag reduction and efficiency increase but also could take significant increases in lift on the outboard region of the wing. Dr. Whitcomb introduced in 1976 the concept of winglets that are *vertical surfaces mounted on the rearward above the wing tip* [38]
. The need of mount this vertical surfaces downward is strictly related to the transonic regime for which this elements was, originally, born. In fact, if the winglets were mounted frontward, the increased velocities over the inner surface of the winglet would overlap with the high velocities over the forward region of the wing upper surface, taking the supersonic bubble to increase in dimension and intensity.
Interesting parameter to analyze, that could influence the wing performance are the sweep angle, the cant angle, the taper ratio of the winglet and the span length. [9]

1.3. Structure of the thesis

We will divide this study into three main phases. First we will do a two-dimensional study around three suitably chosen profiles: a classic NACA profile for aircraft purposes in particular the NACA0012, a profile studied and optimized to work at low Reynolds numbers such as the Eppler E-387, and the optimized profile for high downforce for low Reynolds numbers, the MSHD, that is the result of the optimization study of high lift for low Reynolds profiles of the report [16] using PROFOIL. In this preliminary phase we will go to see what are the aspects related to the two-dimensional by looking at the behavior of these three profiles that have been specifically chosen by us to be 'progressively' more and more suitable for our use. (In fact, we start with a generic NACA profile, move on to a profile for low RN and conclude with a specific profile for this pourpose). The flow around the three profiles will be analyzed, looking at speed and pressure, comparing the three different cases, helping us in the interpretations with the existing literature. Once this preliminary study of the two-dimensional profiles is finished, we move on to the 3d studies where we will instead analyze the real wings obtained by extruding the profiles studied in the previous chapter in the Z direction. In the first part of this chapter, after having properly validated the computational model, we will deal with comparing the three different wings obtained by analyzing those aspects and problems that we expected and that were mentioned in the report [16] passing from the study of 2d profiles to a three-dimensional stream. Once we have chosen the most appropriate wing for our project and fixed the Aspect Ratio, we will begin a sensitivity study of the wing to various geometric parameters including: influence of the joint on the wall, Taper Ratio, Arrow angle, modifications of the plan and different configurations of Endplates. Of

each geometric modification we will analyze the improvements/disadvantages that we will obtain.We will justify our design choices as much as possible by studying the phenomena that these geometric modifications create in the field of motion, helping us with what is explained in the literature. Once a satisfactory configuration has been found in terms of a single wing rigidly fixed to the wall, the intent is to carry out a study of the entire bike with and without fins. In this section we will mainly deal with the interaction that these fins have with the whole bike and with the rider. The idea is to position the fins on the front fairing of the bike in a position that resembles as much as possible that of a wing fixed to the wall. Once the field of motion with and without fins has been analyzed and compared, everything will be simulated and compared using a simple dynamic model to draw final conclusions in terms of maximum acceleration and lap time-

2 | Dynamic models

2.1. Introduction

The need of a dynamic model arises to assess, at the end of the work, the effectiveness of wings on overall motorbike performance, but also to evaluate the pitching angle of a typical motorbike. This parameter is of fundamental importance because we must ensure that during braking phase winglets do not reach the stall angle and during acceleration phase do not overtake the zero-lift angle. In fact, as we do not consider active aerodynamic, the winglets are fixed to the motorbike and an increase in pitch angle necessarily involves an increase in winglets angle of attack and, on the contrary, a negative pitch angle can reduce the angle of attack of the winglets. Furthermore some pure dynamical consideration, apart from aerodynamics, can be made about the mounting position of the winglets which will be the result of a compromise between most convenient location in therms of aerodynamics (where the flow is as much as possible uniform and not slowed down by the motorbike geometry) and in therms of dynamics.
To meet this needs we used two different dynamic models.

2.2. VI-BikeRealTime

First one is an ADAMS-based multibody software, Vi-BikeRealTime^{TM} that is the the more accurate of the two but it can only consider the drag force, neglecting lift force and aerodynamics moments that are of fundamental importance in this work. For this reasons we used this model to evaluate the pitching angle along a test circuit. This test circuit, in figure 2.2, was design to mimic most dynamic situations such as braking from high and low speed, high and low speed cornering and acceleration from low and medium speed.

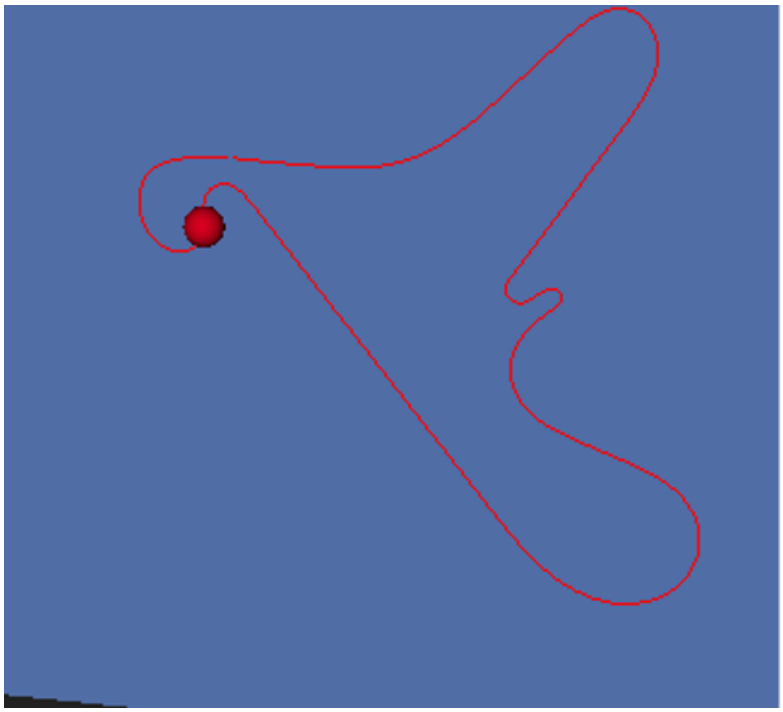

Figure 2.1: Test Circuit

Once track is defined an automatic tool of the software takes care of generating the best trajectory and a maximum performance analysis was done.

Figure 2.2: Maximum performance analysis

From this performance analysis we can get the complete virtual telemetry of our example motorbike. From the complete telemetry we extract data of interest such as the pitch angle but also throttle opening percentage, front and rear brake percentage and rear and front suspension stroke. Data are reported in next figure.

Figure 2.3: Simulated telemetry data

We can clearly see that during braking phase front suspension compresses, at the contrary, rear suspension extends, inducing negative a pitching angle, accordingly with the reference frame used in which the x axis is direct as the velocity, z axis lie on the symmetry plane directed upward and the y one is placed so as to form a right-handed triad. With this data we estimated a minimum pith angle of about 6° and a maximum about 1° for a total variation of about 7°. As said before the winglets have to guarantee a positive effects all along this range to be considered effective.

2.3. Quasi-steady model

In order to be able to take into account of lift forces and aerodynamic moments we wrote a simplified dynamic model that gives as output limit acceleration and deceleration and the maximum speed at mid-corner. At the end of the work this results will be used to implement also a very simplified lap time simulator that gives a firs guess of motorbike performance in terms of lap time. This dynamic model presents some simplifications that

can distort the absolute value of the results but however can be very useful in terms of comparison between different solution. Here are reported main simplification introduced in the model.

- Motorbike with pilot are considered as rigid body. We only considered a variation of center of gravity position between acceleration and braking phase due to the driver movement.
- Rear and front suspension are modeled as simple shocks, without damping. A look-up table was implemented in order to consider the effects of rear suspension kinematic.
- All rotational inertia was neglected because we considered just slow variation of pitch angle.
- A simplified tyre model was used, in which we neglect rolling resistance and we modeled maximum driving and braking force as linear with the vertical load.

$$F_{\mathrm{x_{max}}} = \mu F_{\mathrm{z}} \tag{2.1}$$

- Squat ratio is supposed to be negligible.
- A simplified aerodynamic model was used, in which we considered constant aerodynamic coefficients for all motorcycle trim. Aerodynamics forces and moments due to motorbike and due to winglets was separated and calculated as follows:

$$L = \frac{1}{2}\rho v^2 C_l \tag{2.2}$$

$$L_w = \frac{1}{2}\rho v^2 C_{lw} \tag{2.3}$$

$$D = \frac{1}{2}\rho v^2 C_d \tag{2.4}$$

$$D_w = \frac{1}{2}\rho v^2 C_{dw} \tag{2.5}$$

$$M = \frac{1}{2}\rho v p^2 C_M \tag{2.6}$$

$$M_w = \frac{1}{2}\rho v c^2 C_{Mw} \tag{2.7}$$

in which motorcycle aerodynamic moment was scaled with wheelbase and winglets one with the chord.

2.3.1. Rectilinear motion

Regarding rectilinear motion we wrote, accordingly with figure 2.6, forces equilibrium equations along x and z axis, and momentum equilibrium equation along y axis.

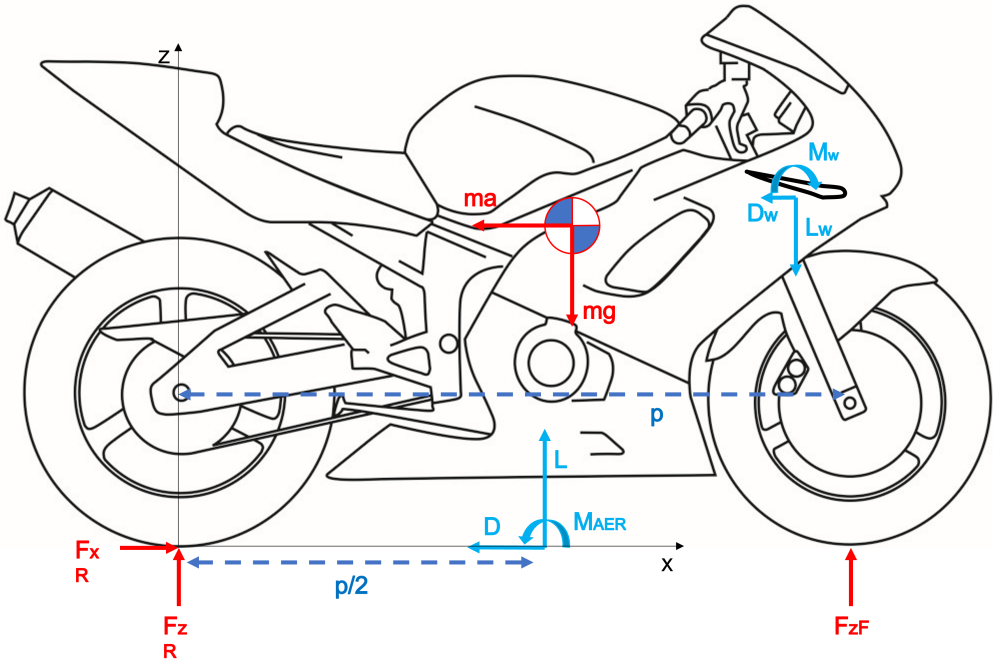

Figure 2.4: Forces and moments during accelerated rectilinear motion of motorcycle

We can notice that we have separated the aerodynamic forces due to the motorbike from those due to the winglets, so that we can rapidly investigate their influence varying their aerodynamics coefficients and their position. Regarding aerodynamics forces due to motorcycle, we have positioned their application centre at $z = 0$ at a distance equal to the half of the wheelbase from the rear contact point. We report:

- equilibrium of forces along z axis

$$F_{zR} + F_{zF} + L - L_w = mg \tag{2.8}$$

- equilibrium of forces along x axis

$$ma + D + D_w = F_{xR} \tag{2.9}$$

- equilibrium of momentum along y axis

$$L \cdot \frac{P}{2} + F_{zF} \cdot P + M_{AER} + ma \cdot h_G + D_w \cdot h_w = mg \cdot b + L_w \cdot x_w + M_w \tag{2.10}$$

- power balance at rear wheel

$$P_r = \eta P_M - I\omega_R\omega = F_{xR}v \tag{2.11}$$

Substituing $F_{\mathrm{x_r}}$ from equation 2.9 we obtain

$$\eta P_M - I\dot{\omega}_R\omega_R = ma \cdot v + Dv + D_w \cdot v \tag{2.12}$$

from which we can get the acceleration limit due to maximum engine power.

$$a_{ENG} = \frac{\eta P_M - I\dot{\omega}_R\omega_R - Dv - D_w}{m \cdot v} \tag{2.13}$$

From equation 2.10 we can obtain the expression of front wheel load

$$F_{zF} = \frac{mgb + L_w x_w + M_w - L\frac{P}{2} - M_{AER} - mah_G - D_w h_w}{P} \tag{2.14}$$

that can be replaced in equation 2.8 give us also the rear wheel load.

$$F_{zR} = \frac{mg\,(P - b) + L_w\,(P - x_w) - L\frac{P}{2} - M_w + M_{AER} + mah_G - D_w h_w}{P} \tag{2.15}$$

We define acceleration limit due to wheelie the acceleration for which front wheel load becomes zero.

$$a_{Wheelie} = \frac{mgb + L_w x_w + M_w - L\frac{P}{2} - M_{Aer} - D_w h_w}{mh_G} \tag{2.16}$$

Last kind of limit in motorbike acceleration is the one due to the grip of rear tyre. We

can obtain the expression starting from equation 2.9, rewriting as follows,

$$a_{Grip} = \frac{F_{xR} - D - D_w}{m} \tag{2.17}$$

introducing the simple tyre model of equation 2.1, and the rear wheel load obtained in equation 2.15. The expression for the limit acceleration due to the grip is presented in next equation.

$$a_{Grip} = \frac{\frac{\mu}{P}\left(mg\,(P-b) + L_w\,(P-x_w) - \frac{L}{2}P - M_w + \ M_{AER} + D_w h_w\right) - D - D_w}{m(1 - \frac{h_G}{P}M)} \tag{2.18}$$

Regarding braking phase we proceed in an analogous way just considering a negative F_{xR} and introducing a F_{xF} also with direction opposite to that of the x-axis, as in next figure. Their sum will form the braking force $F_{Braking}$.

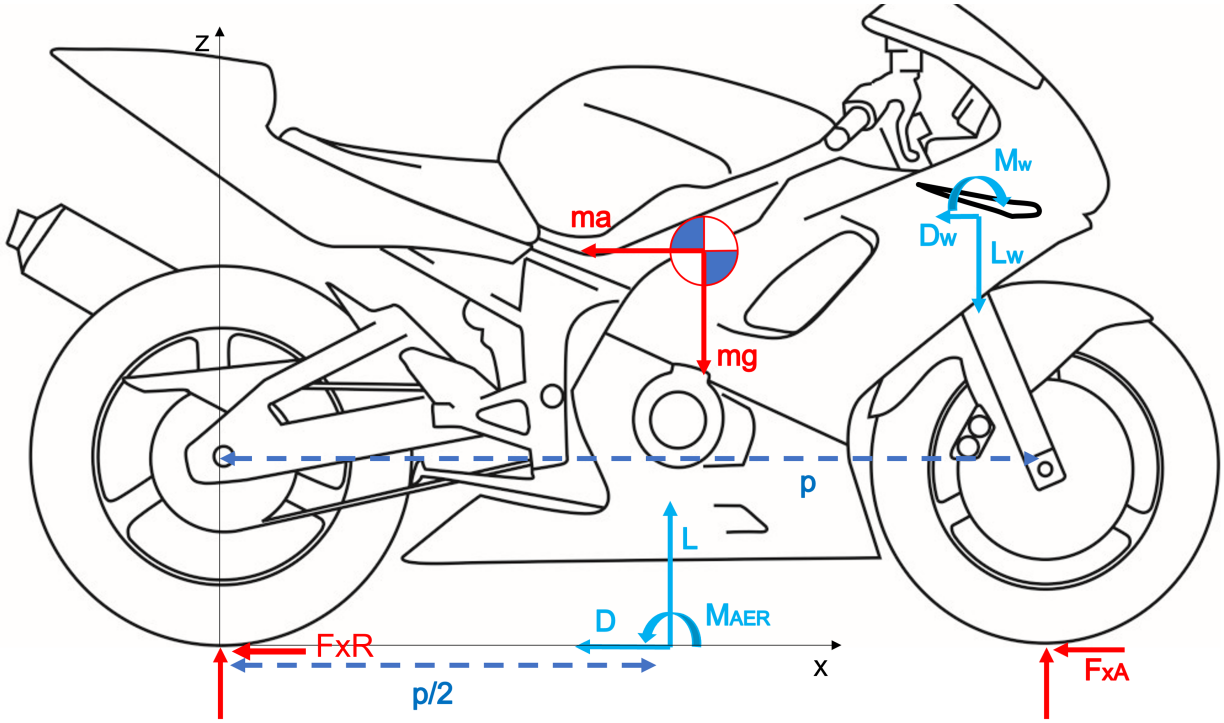

Figure 2.5: Forces and moments during decelerated rectilinear motion of motorcycle

Equilibrium equations of the forces along z-axis and of the moments along y-axis remain unchanged, instead the equilibrium along x-axis becomes

$$ma + D + D_w = -F_{xR} - F_{xA} \tag{2.19}$$

For braking phase we just considered two limits:

- limit due to tipping forward which, in motorbike jargon, is called stoppie
- limit due to the grip of the tyres

We didn't consider the limit due to the power of the braking system because in any motorbike it is design so that it largely exceeds the other two limits in any situation.
We considered maximum deceleration due to stoppie as the deceleration for which rear vertical load becomes zero. So imposing in equation 2.15 $F - zR = 0$ and rearranging the equation we get

$$a_{Stoppie} = \frac{-mg(p-b) + L_w(p-x_w) + M_w + L\frac{P}{2} - M_{Aer} - D_w h_w}{mh_G} \tag{2.20}$$

Regarding the limit due to maximum grip we can proceed as in the acceleration case. We considered two different coefficient of friction for front and rear tyre. The equation for maximum deceleration due to tyre grip is

$$\begin{aligned} a_{Grip} = & \frac{\frac{\mu_r}{P}\left(mg\,(P-b) + L_w\,(P-x_w) - \frac{L}{2}P - M_w + \ M_{AER} + D_w h_w\right)}{m(1 - \frac{h_G}{P}\mu_r - \frac{h_G}{P}\mu_a)} \\ & + \frac{\frac{\mu_a}{P}\left(mgb + L_w x_w - \frac{L}{2}P + M_w - \ M_{AER} - D_w h_w\right) + D + D_w}{m(1 - \frac{h_G}{P}\mu_r - \frac{h_G}{P}\mu_a)} \end{aligned} \tag{2.21}$$

Once the equations to determine maximum acceleration and deceleration are defined, we moved on to suspension modeling. Different link desing for rear suspension are available. Some example are reported in next figure, from V.Cossalter. [8]

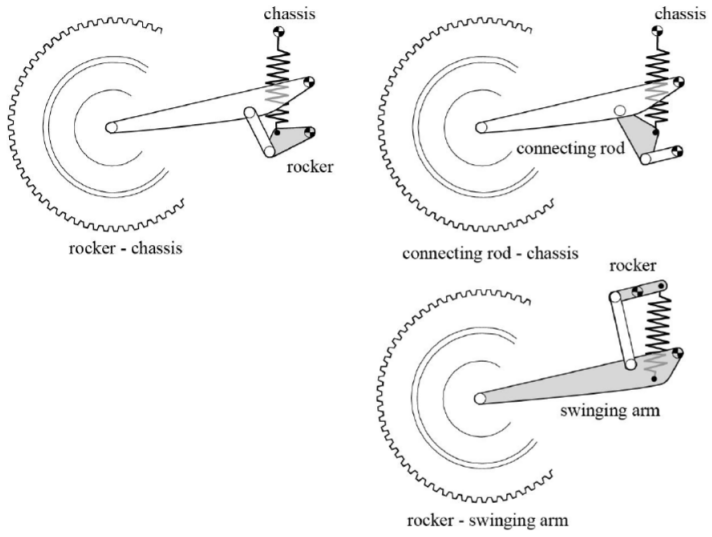

Figure 2.6: Examples of rear suspension links

We focus on first solution. In order to obtain the equivalent torsional stiffness a power balance was used:

$$C_{m_{eq}}\omega_{sa} = F_{shock}\dot{\Delta}s \tag{2.22}$$

where:

- $C_{m_{eq}}$ is the equivalent torque applied at the swingarm pivot
- ω_{sa} is the angular velocity of the swingarm
- F_{shock} is the force of the real shock
- $\dot{\Delta}s$ is the velocity rate of spring contraction

from equation 2.22 we obtain the equivalent torsional stiffness:

$$K_\theta = \frac{K_{shock}\Delta s\dot{\Delta}s}{\theta\dot{\theta}} \tag{2.23}$$

in which the expression of $\frac{\Delta s}{\theta}$ and $\frac{\dot{\Delta}s}{\dot{\theta}}$ can be simply obtained from geometric parameter of the link writing the two different vector closures equation of figure 2.8

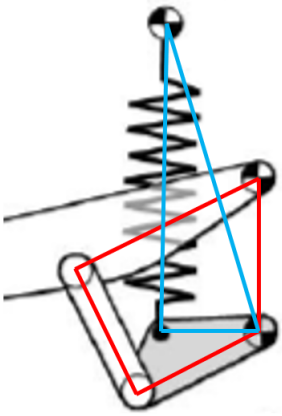

Figure 2.7: Vector closures of the rear link for the determination of equivalent torsional stiffnes

In this way we can obtain a look-up table to use in our script during the calculation of limit accelerations. We now have to introduce our suspension model into motorbike model. As said before we modeled suspension just as shocks, neglecting dumping.
We can consider the y-momentum equilibrium equation around the swingarm pivot in order to calculate θ.

$$K_\theta \theta = F_{zR} l \cos(\theta) - S(R + l \sin(\theta)) \tag{2.24}$$

where:

- R is the wheel radius
- l is the swingarm length

We can also consider the equilibrium equation on the forks.

$$F_{zA} \cos \varepsilon + F_{xA} \cos \varepsilon = 2K_{fork} \Delta l_{fork} \tag{2.25}$$

from which wan can simply obtain the shortening of the forks. Finally, from the vector closures of next figure we can obtain horizontal and vertical displacement as function of fork shortening and swingarm rotation, so as function of vertical rear and front wheel load.

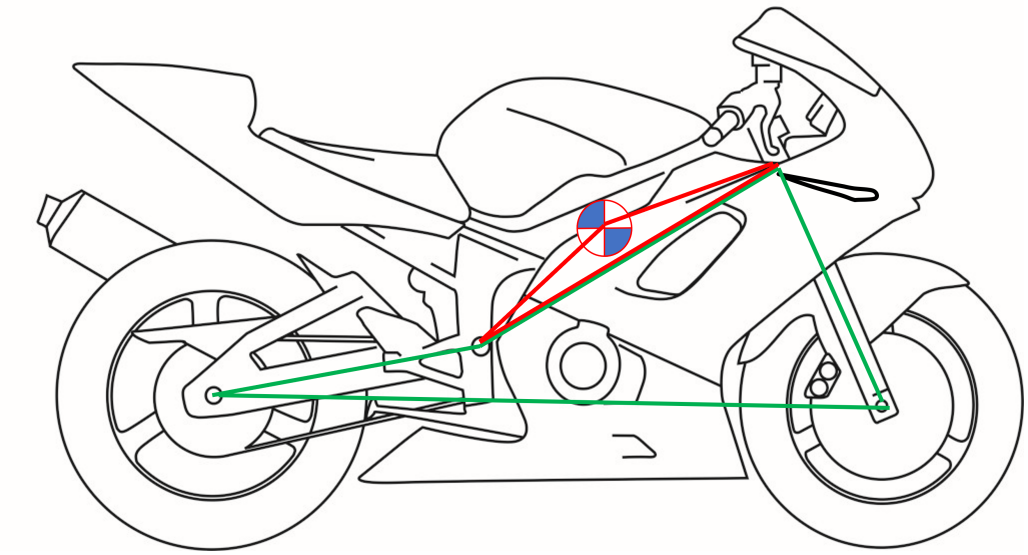

Figure 2.8: Vector closures of complete motorbike for the determination of center of gravity displacements

We would like to point out that the point at the end of the fork is at an arbitrary distance from the front wheel axle. In fact we are interested in its more than in its absolute value. Now, we move on the description of the algorithm for maximum acceleration and deceleration which make use of the equation till now explained.

Algorithm 2.1 quasi-steady model for rectilinear motion

Declaration of geometric data
Declaration of aerodynamic data
Declaration of initial condition
Declaration of the phase (acceleration or deceleration)
Initialization of initial trim as static trim
for $i = 1 : \frac{timetosimulate}{dt}$ **do**
    Calculation of aerodynamic forces
    Calculation actual engine power
    Calculation of equivalent torsional stiffness
    Calculation of motorcycle trim and center of gravity position
    if $phase = accelerationphase$ **then**
        Calculation of limit accelerations and storing in different vectors
        Storing of minimum of the three in a vector a_{eff}
        Re-calculation of F_{zR} and F_{zA}
        Calculation of the i-velocity with trapezoidal rules integration of acceleration
        Calculation of the i-motorbike-displacement with trapezoidal rules integration of velocity
    end if
    if $phase = decelerationphase$ **then**
        Calculation of limit deceleration and storing in different vectors
        Storing of minimum of the two in a vector dec_{eff}
        Re-calculation of F_{zR} and F_{zA}
        Calculation of the i-velocity with trapezoidal rules integration of deceleration
        Calculation of the i-motorbike-displacement with trapezoidal rules integration of the velocity
    end if
end for
Plot data

We can notice that in this simple algorithm we use the motorcycle trim obtained at the iteration $i-1$ to calculate acceleration, and so velocity and position, at the iteration i. Keeping a small dt however this approximation becomes really negligible. In order to verify this hypothesis a convergence study was done progressively decreasing this time interval. Moreover algorithm and equations simplicity allows to keep a very little interval without obtaining large computational time. Selected dt is equal to 0.01s Regarding the engine power a separate function was implemented. It needs as input a vector containing

the ratio between engine and rear wheel speed, from first gear to sixth gear. Maximum engine rpm are also requested. This algorithm first step is to look for best gear, that is the one that guarantee maximum engine speed, without exceed maximum threshold required before. Once gear is selected it calculates the engine speed from motorbike speed and uses a look-up table to determine torque and power. At very low speed we imposed a minimum power because during starting the clutch is released slowly while keeping the motorbike at high revs. It is very difficult to have an accurate model of the starting power that could change from time to time depending also on the sensitivity and skill of the pilot.

2.3.2. Cornering motion

Regarding cornering motion we focus on the center of the curve that is most critical point. In this phase we can consider longitudinal acceleration to be zero because all tyre capabilities are used to maximized lateral forces. It is clear if we consider friction ellipse.

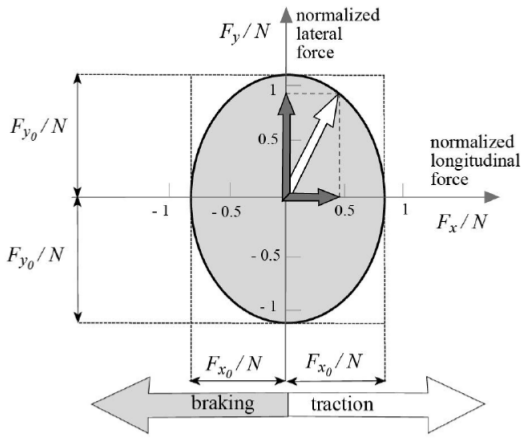

Figure 2.9: Friction ellipse example. Image from [8]

We know that presence of longitudinal forces reduces capability of producing lateral forces. We are considering the time at which rider released the brakes and has not yet started to accelerate.

In this case we considered, as in rectilinear motion, simplified tyre model in which maximum friction was considered linear with vertical tyre load. However we introduced concept of toroidal tyre instead of lenticular one. With this model we take into account the fact that the point of contact will move to the edge of the wheel and no longer lie on the plane of symmetry.

A rider displacement was also considered. In fact during a corner professional riders tends

to move inwards curve, as in figure 2.10 so that, as we will see in following equation, at equal motorbike lean angle can produce more lateral forces.

Figure 2.10: MotoGp rider in cornering motion [15]

We now start, referring to figure 2.11, to point out equilibrium equations.

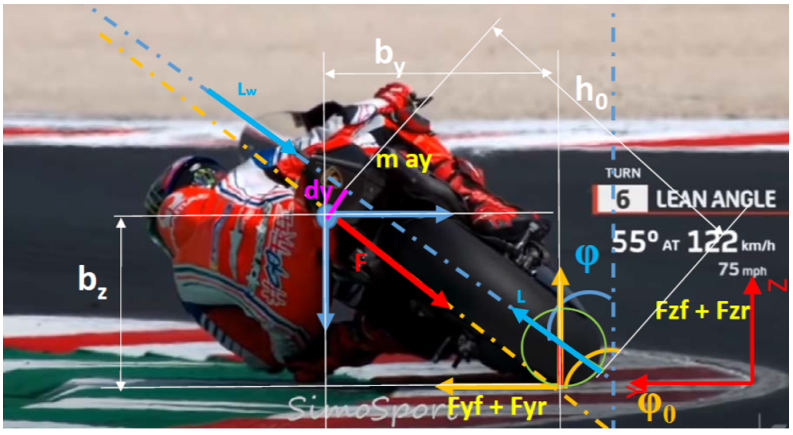

Figure 2.11: Forces acting on motorbike during corner

- Equilibrium equation along z

$$F_{zR} + F_{zF} + L\cos\varphi - L_w\cos\varphi = mg \tag{2.26}$$

in which φ is the lean angle

- Equilibrium equation along y

$$F_{yR} + F_{yF} + L\sin\varphi - L_w \sin\varphi = ma_y \tag{2.27}$$

- Momentum equilibrium equation along x

$$ma_y b_z = mgb_y \tag{2.28}$$

in which

$$b_y = (h_0 - t)\sin\varphi + dy\cos\varphi \tag{2.29}$$

end

$$b_z = t + (h_0 - t)\cos\varphi - dy\sin\varphi \tag{2.30}$$

dy is center o gravity displacement of the whole system, due to the movement of the rider and t is the toroid radius.
In equation 2.30 we neglected contribute from L and Lw because their momentum arm is negligible. From equation 2.30 we can obtain φ and introducing the equations

$$F_{yR} = \mu_R F_{zR} \tag{2.31}$$

end

$$F_{yF} = \mu_R F_{zF} \tag{2.32}$$

in equation 2.27 we can obtain also the maximum lateral acceleration that is the only limit that was considered in this model. From lateral acceleration we can obtain also maximum cornering speed as follow

$$v = \sqrt{aR} \tag{2.33}$$

Also in this case, next step was to model suspensions. The concept is basically the same of the rectilinear motion but equation 2.24 and 2.35 had to be corrected considering the lean angle and introducing the component parallel to the symmetry plane of F_{yR} and F_{yF}.

$$K_\theta\theta = (F_{zR}\cos\varphi + F_{zF}\sin\varphi)\, l\cos(\theta) \tag{2.34}$$

$$(F_{zA}\cos\varphi + F_{yA}\sin\varphi)\cos\varepsilon = 2K_{fork}\Delta l_{fork} \tag{2.35}$$

Also in this case an iterative procedure was implemented. Maximum velocity at the center

of the curve was searched for curve with different radius, from 10 meters to 250. For each radius we started from a velocity equal to $1\frac{m}{s}$ and, thanks to a while cycle, we increased it of a value of 0.1 till it reached the maximum value calculated within this cycle. Next algorithm scheme shows the procedure

Algorithm 2.2 quasi-steady model for cornering motion

```
Declaration of geometric data
Declaration of aerodynamic data
for R_curve = 10 : 1 : 250 do
    v=1
    while v<vLim do
        calulate lateral acceleration
        calculate φ using lenticular approximation
        Calulate aerodynamic forces
        Initialize vertical wheel load using φ calculated before
        while abs(vLim(i+1)-vLim(i))>tolerance do
            Calculate motorcycle trim and center of gravity position
            Recalculate vertical wheels loads
            Recalculate phi
            Calculate vLim
        end while
        v=v+0.1
    end while
    store vLim in a vector
end for
plot R_curve against Vlim
```

We can notice the use of a double while cycle. The first one is needed to slightly increase the velocity, the second one to obtain a convergence for the maximum velocity. In fact, for each internal while iteration the algorithm completely recalculate motorbike trim and use that to recalculate the limit velocity till it remain almost constant between one iteration and the previous one. Tolerance between two iteration is user-definable.

2.3.3. Lap time simulator

Results of the first part of the algorithm can be used to have a, albeit not very accurate, prevision of the lap time. Once selected a circuit, it is necessary to construct the trajectories so that they are composed by straight part and constant radius curves, as in next figure.

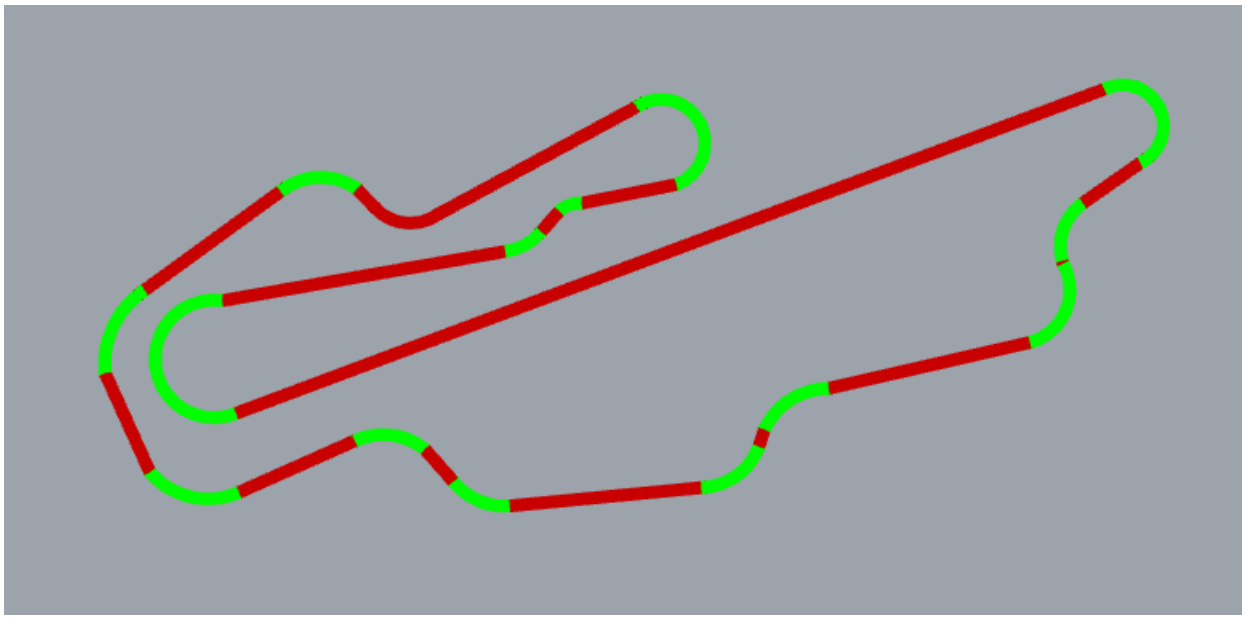

Figure 2.12: Race track used in lap time simulator

The inputs of the lap time simulator will be the limit acceleration and deceleration, the maximum cornering velocity and other three vectors:

- the first one collects the length, in order, of all straight
- the second one collects the length, in order, of all the curves
- the last one collects the radius, in order, of each curve

First task is to calculate, using velocity limit in cornering motion as look-up table, the maximum speed.
Second task is to calculate where the pilot had to switch from acceleration phase to deceleration phase. This is done using a while cycle in which motorbike try to start the braking phase 1 meter before the end of the straight and evaluate the speed at the end. If this speed is higher than the one prescribed, the algorithm anticipate the braking of 0.1m, till the right braking position is found. Once braking position was found for each curve it start integrating the acceleration and deceleration to find time needed for straight

motion of all the circuit. Finally, maximum cornering speed and curves length are used to calculate how many time motorbike needs to ride the curves.
We will use this algorithm at the end of the work to evaluate the effectiveness of the winglets.
Circuit chosen is the circuit of Mugello, in Italy, that is one of the track in which average velocity is highest. In this way, as we will see in the following, we will got a conservative prevision about winglets effectiveness.

2.3.4. Motorbike data and quasi-steady model results

Once the algorithm was done, we decided to test three motorbike cases:

- a low displacement bike with little power
- a large displacement bike with medium power, comparable to the one used in Moto2 championship
- a large displacement bike with high power, comparable to the one used in Superbike championship

It would also have been interesting to test a case similar to the top of the range like MotoGp championship motorbike but insufficient data forced us to give up. Little power motorbike taken as reference is the Cagiva Mito 125, medium power one is the Ducati 959 Panigale and the high power one is the Ducati 1199 Panigale.
This choice is driven by the fact that, for medium and low power bikes, it was possible to take some measurements and some data directly on the bikes. The high power one instead has the really same frame of the medium one and the same weight. It is reasonable to approximate the most powerfull having the same main data of the medium one, except the torque curve. To recap we need:

- motorbike mass and center of gravity position
- pure geometrical data as length and angle
- torque curve
- aerodynamic coefficient and frontal area
- friction coefficient for tyres
- suspension shock stiffness or equivalent torsional stiffness

Regarding motorbike mass, it is available on most motorbike newspapers, instead, center

of gravity position, especially of the whole system, motorbike with pilot, is not available for the specific cases treated in this thesis. An estimation is available in literature, in particular in the work of Victore Cossalter et al. [28]. Once center of gravity was fixed, geometrical data were found with a reverse engineering work using photographs for publicity purposes in which motorbike was photographed from the side. Picture was inserted as background bitmap in Rhinoceros^{TM} and rescaled so that wheelbase would coincide with the one declared from manufacturer. Power and torque curves were available from online resources thanks to some published report of braked dynamometer tests. This kind of tests give as results power at the wheel so transmission efficiency is not necessary. On motorbike manual service, instead, it is possible to find all transmission ratios.
Aerodynamic coefficient, for now, are take from the book of Victore Cossalter. They will be replaced with our simulations results in the last chapter. Also friction coefficient for tyres were taken from that book. Shock stiffness instead is reported with a little incision directly on the shock of motorbike. However it is possible to have an experimental estimation: lifting the motorbike onto special stands and unloading the wheels it is possible to measure fork extension and swingarm rotation using a calibre and an inclinometer.
We now presents some useful results, starting from the description of each phase output. In figure 2.13 we present the output of the algorithm for rectilinear acceleration for the basic case of the high-power motorbike. Here are plotted, as function of v, all three tipes of limits described before and, with dotted line, the final results of the combination of the three.

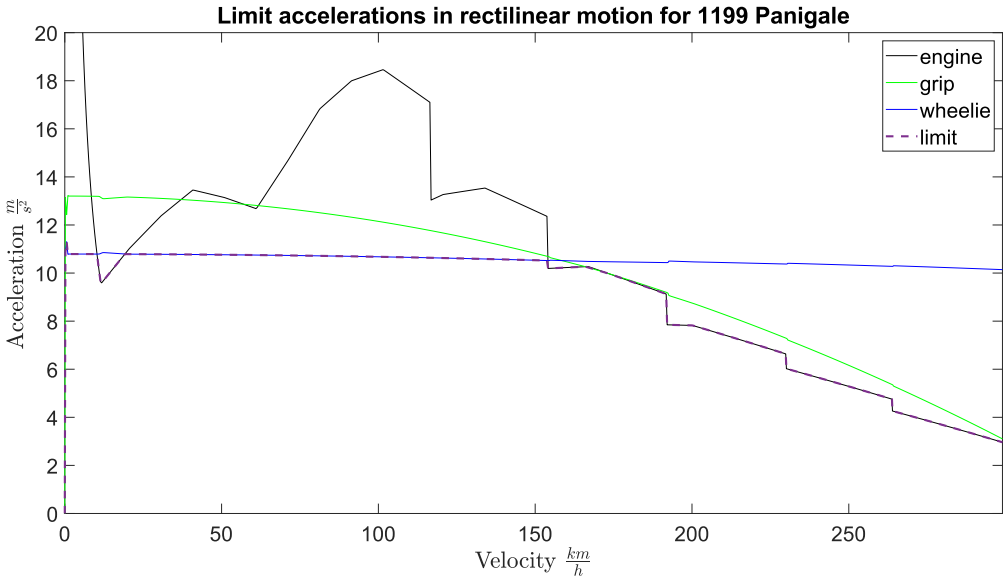

Figure 2.13: Limit accelerations during rectilinear motion of 1199 Panigale

We can see, after a first phase in which pilot is releasing the clutch, a large range of velocity in which acceleration is limited by wheelie phenomena, after which the limit is due to maximum engine power. We can highlight some typical trends: increasing velocity we can see a reduction of both grip and wheelie limit. Regarding wheelie limit is mainly due to lift force and aerodynamic moment, instead if we look at the grip limit we can say, supported by the plot of figure 2.14, that its reduction is mainly due to reduction of load transfer. In fact, increasing velocity, acceleration, so load transfer, becomes less influential, as we can see in next figure in which are reported front, rear and total vertical loads as function of v. .

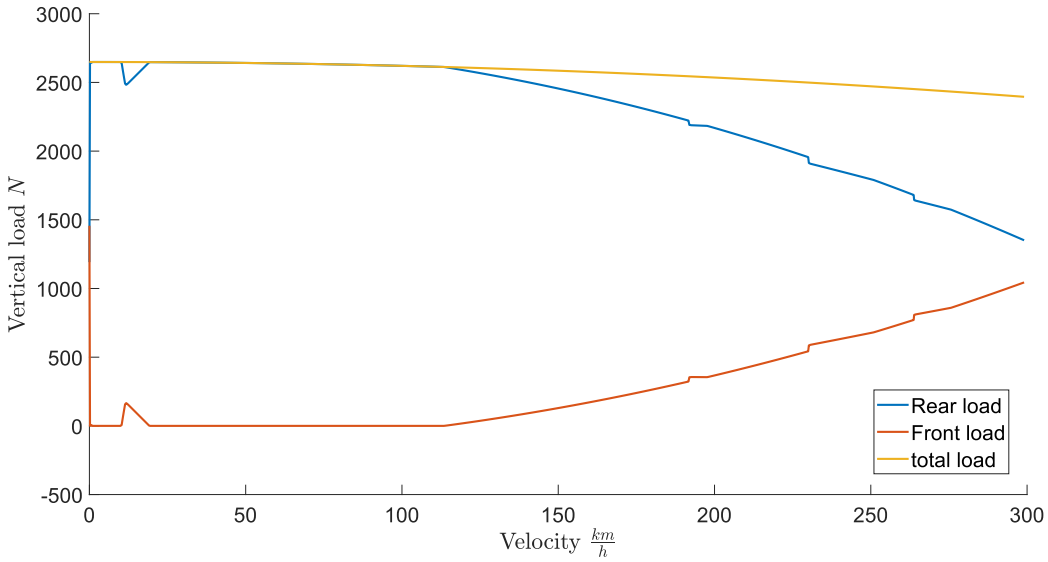

Figure 2.14: Wheel load during acceleration phase

Similar output is observable for braking phase. In figure 2.15 we can see the same motorbike considered before the output of the two braking limit described before.

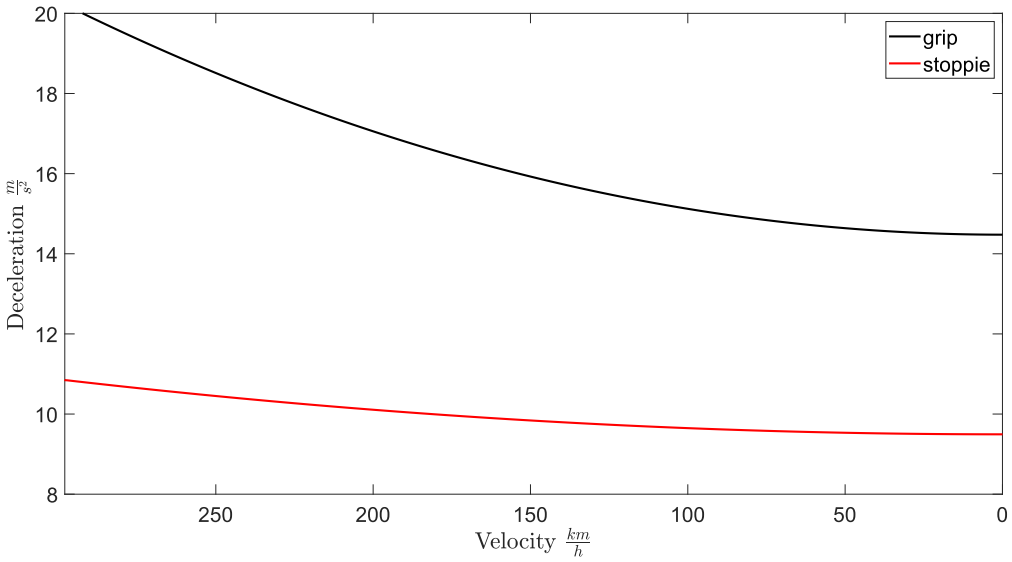

Figure 2.15: Limit decelerations during rectilinear motion of 1199 Panigale

We can clearly see that, for racing motorbike, where short tyre life is allowed and for tyre a very soft compound is used, the only limit acting during deceleration phase is the one due to tipping forward. A more sophisticated tyre model could reduce this gap between the two limit, however, the tendency to overturn is a phenomenon actually found in racing motorbikes. An example of this phenomena is reported in next figure, that depicts a motorbike under braking.

Figure 2.16: Example of real motorbike during braking phase

Last output is the one for describing mid-curve performance. In this case we preferred to plot maximum velocity instead of maximum lateral acceleration, just because it is more indicative. To have a complete overview of cornering behaviour, as said before, we calculate the maximum velocity for a wide range of curvature radii. An example is

reported below.

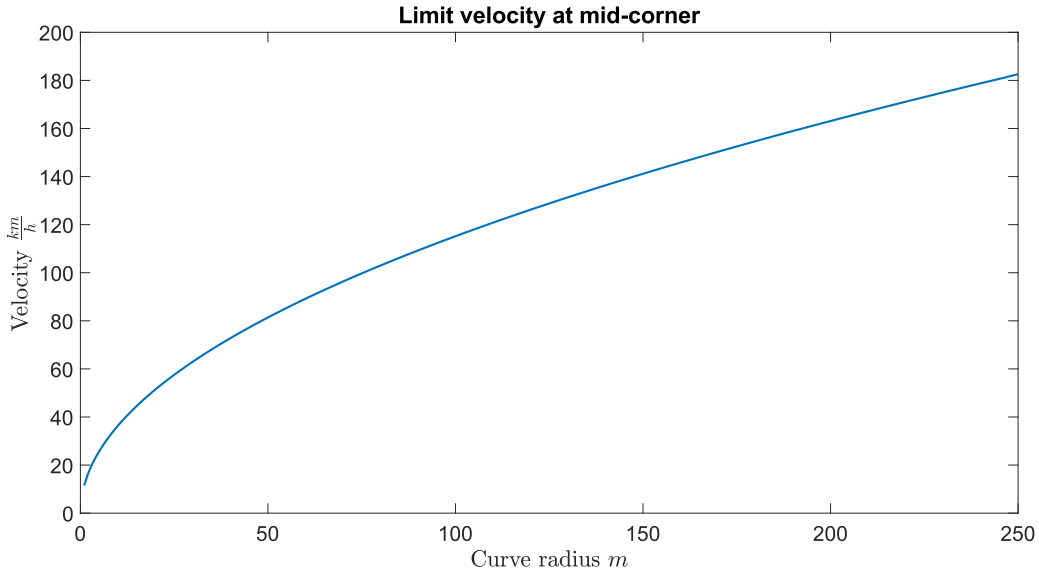

Figure 2.17: Limit velocity at mid corner for 1199 Panigale

First test done concern a comparison between basic cases of the motorbikes described before and a case in which were introduce winglets effects. We have assumed to place it at at a height of 0.7 meters and at 1.3 meters from the rear wheel contact point. We assumed:

- a lift coefficient of 1.5
- a drag coefficient of 0.3
- a moment coefficient, referred to chord length of 0.2.
- a chord and a span of $0.15m$ for each winglet

We report below the comparison. For clarity reasons in following graph is reported only the resulting value of limit accelerations, without reporting both wheelie, grip and engine limitations.
We start from the less powerfull motorbike.

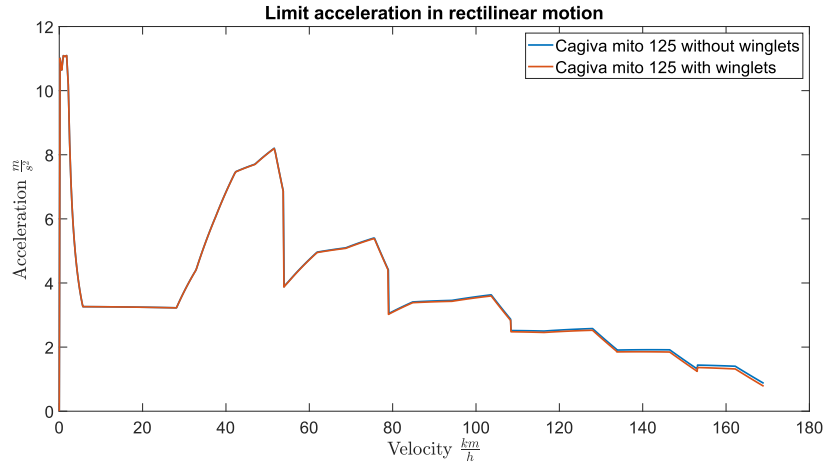

Figure 2.18: Limit acceleration comparison for a low power motorbike, with and without winglets

We can notice that in this case the winglets do not bring any advantages, on the contrary, they reduce acceleration capabilities at high speed. This is due to the fact that, with the exception of the starting phase, limit acceleration is due to engine power. Motorbike with winglets takes about 5 tenths of seconds more to get maximum speed.

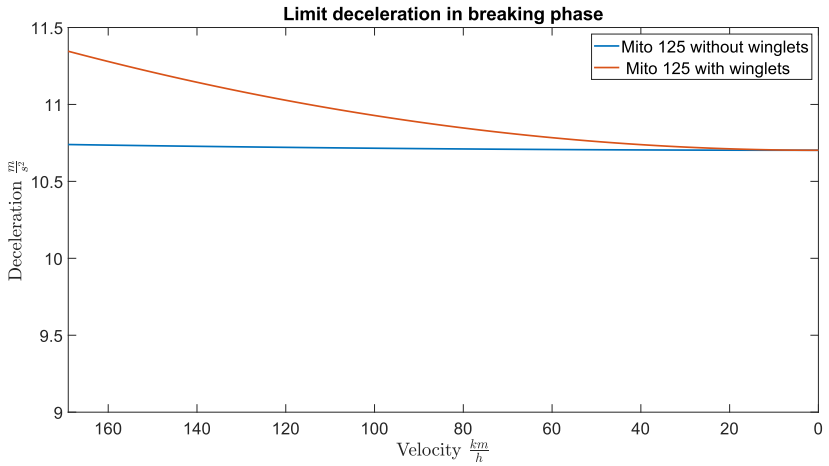

Figure 2.19: Limit deceleration comparison for a motorbike with little power, with and without winglets

During braking phase some advantages are visible at high velocity, decreasing with speed, where, obviously, aerodynamic effects become less relevant. In therms of times, however there is not a significant difference. Results indicate a difference of $0.03s$, too small value to be considered reliable using our model. These advantages are due to the fact

that winglets are mounted behind front wheel contact point, so they generate a favorable pitching moment that reduce the tendency to stoppie.

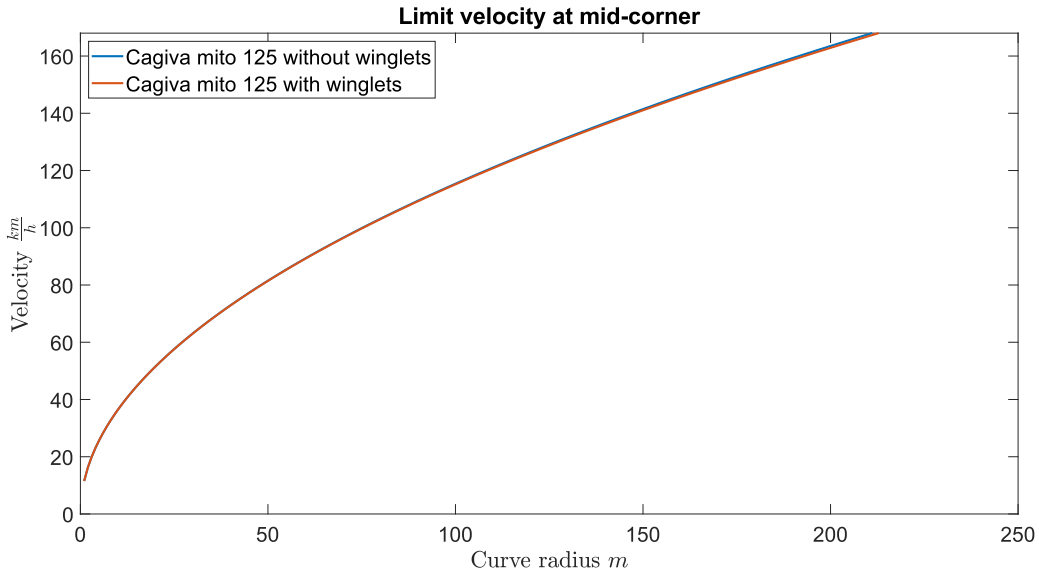

Figure 2.20: Limit mid-corner velocity comparison for a motorbike with little power, with and without winglets

Finally, regarding mid-corner speed, we can see that winglets do not contribute to an improvement in performance and results remain more or less unchanged.
Summarising we understood that for a low-power motorbike:

- during acceleration phase winglets are always counterproductive because the motorbike does not have a tendency to wheelie, furthermore the increase of drag makes aerodynamics less efficient high velocity
- during braking phase winglets can take some advantages, especially increasing the distance of the winglets from rear wheel. About that, we tried to move back the winglets $300mm$ with positive results shown in next figure.

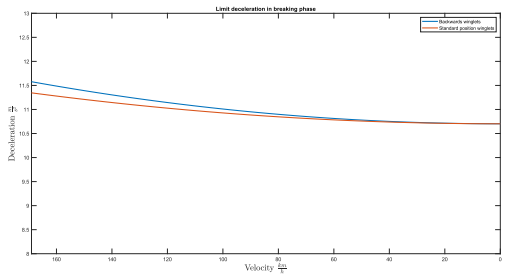

Figure 2.21: Limit acceleration comparison for a motorbike with low power, with winglets in different positions

Turning instead to the medium-power motorbike we can notice, in figure 2.22 a region, from about $70\frac{km}{h}$ to about $70\frac{km}{h}$ in which winglets are able to raising the wheelie limit, while still maintaining the negative effect at high speeds.

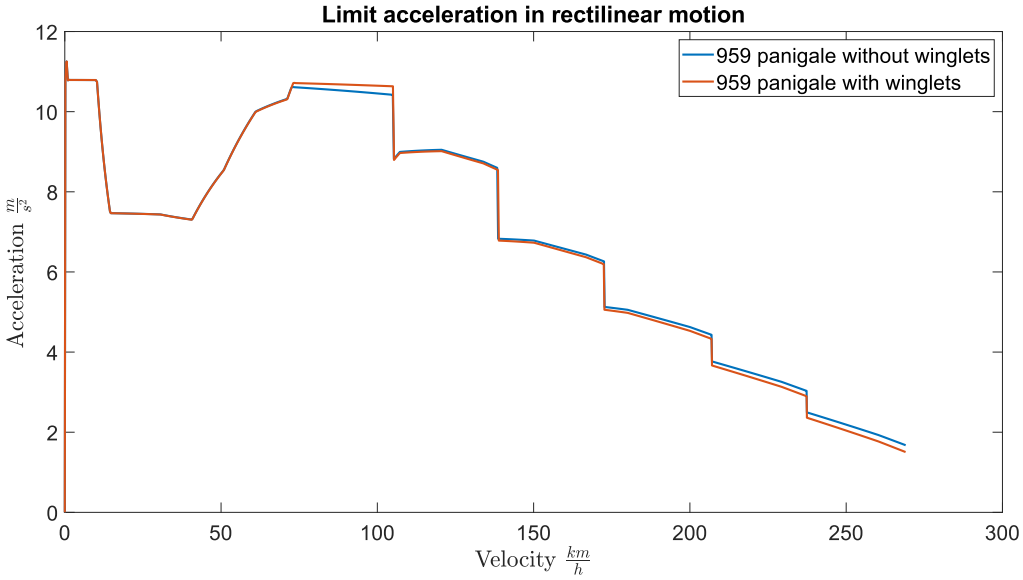

Figure 2.22: Limit acceleration comparison for a motorbike with medium power, with and without winglets

Overall, the time required to reach maximum speed is less in the case without winglets but we should consider two different aspect:

- advantages during braking phase becomes more relevant due to higher maximum speed, with compared to low power motorbike, as visible in figure 2.23
- average speed in most of the circuit is around $159\frac{km}{h}$ and typically there is only one long straight in which motorbike reach maximum speed

Having said that, and considering that the speed in the middle of the curve, as in figure 2.24, still remain unchanged , we can state that for an evaluation of the performance variations, for this case, we would need to use the lap time simulator, analyzing different circuit.

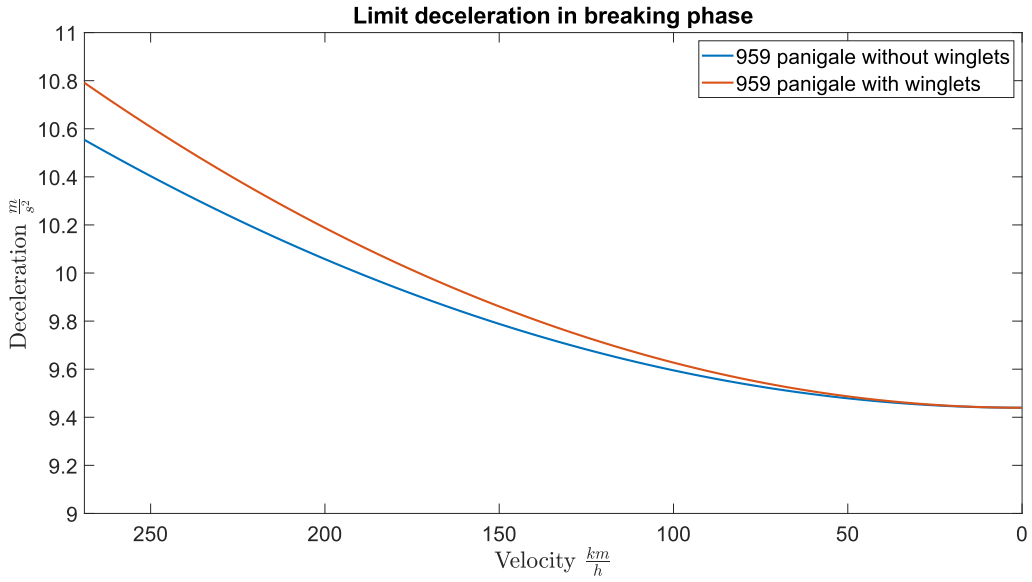

Figure 2.23: Limit deceleration comparison for a motorbike with medium power, with and without winglets

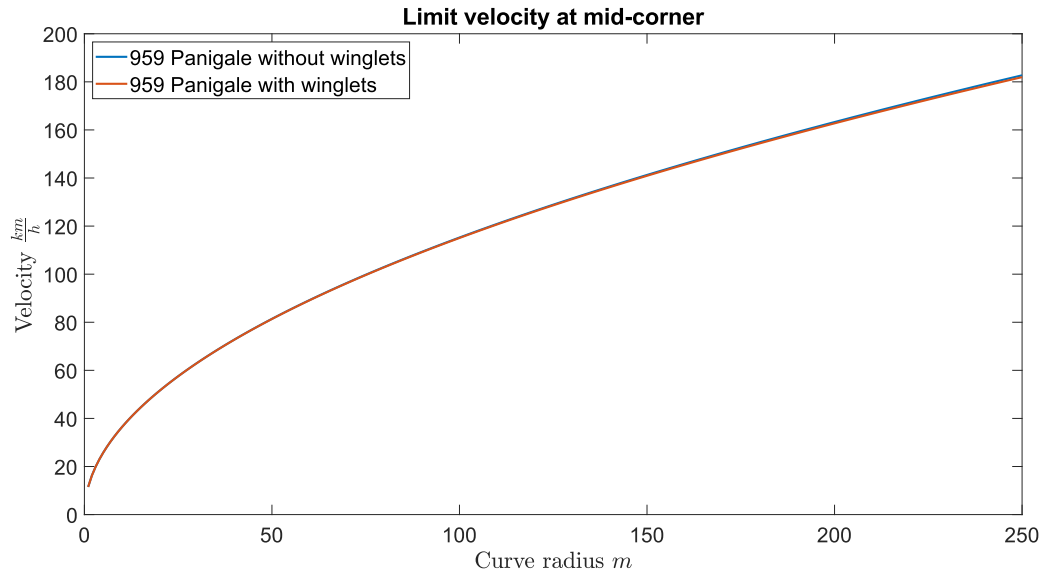

Figure 2.24: Limit mid-corner velocity comparison for a motorbike with medium power, with and without winglets

For high power motorbike we report only the results for acceleration phase since braking phase and mid corner speed are the same of medium one.

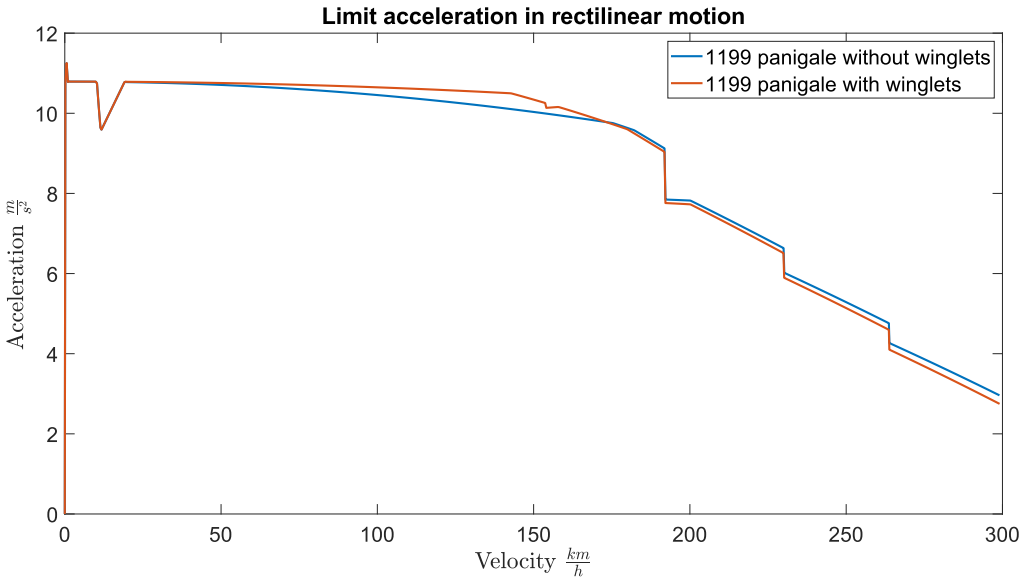

Figure 2.25: Limit acceleration comparison for a motorbike with high power, with and without winglets

In this case a very considerable range of velocity is affected by wheelie limit and winglets can best exploit their advantages. In this case, for the first time, time to get maximum speed decrease if winglets are used. If we consider a straight in which pilot accelerate up to maximum speed and than brakes up to stop, winglets can reduce time needed for this manoeuvre at almost $0.7s$ that is a great result.
Before concluding, we would like better analyze and explain the trends obtained for mid-corner speed. If we have a look at figure 2.11 and at equation 2.27 we can see that winglets lift has two different effects:

- increases the vertical load, positive effect
- increases the lateral forces needed to make the turn, negative effect

The two effects just described change their contribution with the lean angle. First one is higher when lean angle is small instead, when lean angle overtakes 45◦, the second one becomes greater. However is not so simple as that because vertical forces are weighted by friction coefficient and in addition winglets lift cause a, albeit small, center of gravity lowering. Considering a pilot center of gravity displacement of $80mm$ towards the center of the curve, the one used to obtain all previous graph, we obtain a lean angle range between 50 and 55 degrees, angle for which positive and negative effects eliminate each

other.
Vojtěch Sedl in his master thesis [25] proposed a solution to eliminate this lateral component, obtaining so advantages also at mid-corner. We will treat this topic in subsection 6.2.3

3 | Approaches to aerodynamics

In the study of aerodynamics, there are several methods by which problems can be approached. It is possible to perform full-size real tests, under real flow conditions. This method is definitely the easiest and the most straightforward in obtaining surely correct results, however it is to expensive for design phase of the project. This is why wind tunnels are used, which by exploiting the theory of aerodynamic similarity, allow us to carry out tests in a smaller range of motion both with scaled-down both with real size models, all to cut down costs. This is definitely a more indirect study that brings with it some complications in reconstructing the real conditions of the problem among which one of the main is to reproduce the realistic Reynolds number. An alternative method that, with the recent fast evolution of computers has certainly become more competitive is Computational Fluid Dynamics (CFD). In this way we can create a virtual model that simulates the real one, while keeping costs low. This method also has its limitations that the user must be aware of: firstly from the moment we build a totally virtual model we must keep in mind that the computer has incomplete knowledge of the physical phenomenon being studied, furthermore the main limitation is the computational cost that fluid dynamic simulations require, this obviously depends on the computational power that we have available. In this thesis we have chosen to use CFD for several reasons, chief among them cost and the consequent freedom to perform as many tests as possible. We will see in the following chapters that the studies and simulations we performed would have been too numerous if we had thought of doing real or wind tunnel tests (think also only of the need to build several real fin models and the related construction issues). We chose as our CFD software OpenFOAM^{TM} which is an open-source software developed by OpenCFD Ltd since 2004. OpenFOAM^{TM} is a software without a graphical user interface that therefore needs terminal commands, however, for the finite-simulation visualizations we used Paraview. As far as computational power is concerned, we relied mainly on a multiprocessor desktop computer with a fair amount of RAM, however, to carry out the longer and heavier simulations we had to rely on the cluster at the Politecnico di Milano since the computational costs would have been too high even for our desktop computer. For the validation of the results, as we will see in the next chapters, in addition to compar-

ing the results with reference gallery data (2d) or with other software based on different theories, such as non linear lifting-line theory (LLT) we wanted to make sure of the independence of the computational grid by trying to thicken the grid and comparing the results.

3.1. Simulation Approaches

There are three different methods to simulate the motion of the fluid 3.1:

- Direct Numerical Simulation (DNS);
- Large Eddy Simulation (LES);
- Reynolds Averaged Navier-stokes (RANS);

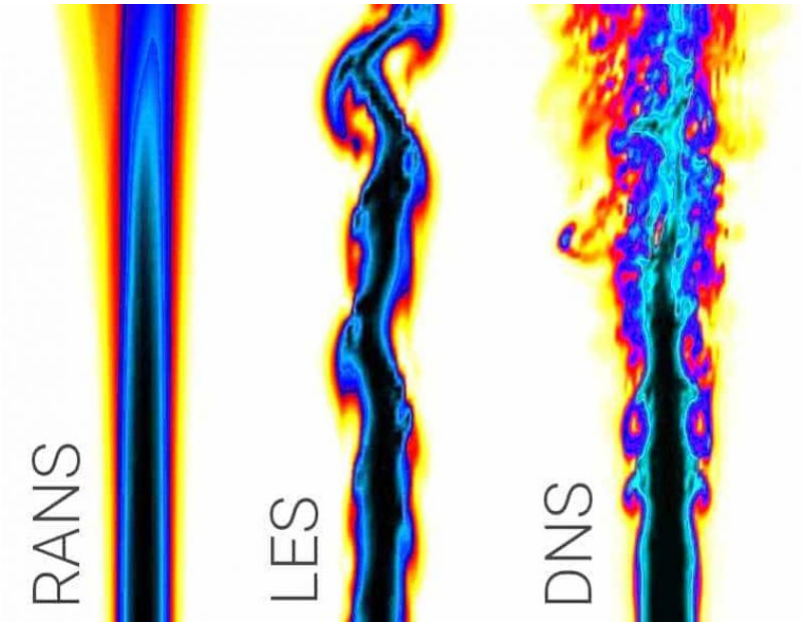

Figure 3.1: Simulation approaches results visualization for RANS, DNS and LES

Generally, LES and DNS allow for higher accuracy in simulations than models based on RANS equations. In particular, DNS turns out to be the most refined simulation method in the field of fluid dynamics. This method consists of solving the Navier-Stokes equations (see appendix B) without the need for a turbulence model and is able to capture vortices of all dimensions. However, the amount of computational power required, even

for simple flows, is very high. This method is not suitable for industrial applications, since there are currently not enough CPU resources, and is therefore used only as a research. As for large-scale vortex simulations (LES), which are discussed extensively in the text by Baurle [4], the method is capable of overcoming the many disadvantages associated to RANS simulations; particularly when it comes to accuracy or when one wants to perform a non stationary simulation. LES is part of SRS (Scale Resolving Simulations); in essence, this model solves large-scale vortices and models small-scale vortices instead. What defines the size of the vortices depends on the physical size of the flow geometry and the number Reynolds number. Smaller vortices can be explained by referring to the scale of Kolmogorov. The main reason for using LES-type models lies in the fact that, large vortices size are responsible for 90 percent of the mass transport, momentum, and energy and thus directly affect the mean flow. Smaller vortices on the other hand go only to dissipate the fluctuations. The biggest disadvantage lies in the fact that LES require large amounts of computational power (less than DNS but nevertheless not negligible) due to the need for of a high-resolution grid and very small time steps for non stationary. The RANS model is then applied to problems for which a solution is required to be stationary. Moreover, if the grid resolution is good enough, then the accuracy is also sufficiently high. However, these considerations are no longer valid in the case where more complex flows are involved.

3.2. Theoretical background on RANS model

To solve the governing equations in order to represent a fluid statistically, the traditional approach in CFD is to resort to simplified Reynolds-Avereged-Navier-Stokes (RANS) equations. The RANS equations represent the mediated form of the standard Navier Stokes equations, where the quantities are no longer instantaneous but are averaged over a certain period of time, which is sufficiently small with respect to the phenomena involved and sufficiently large with respect to the turbulence disturbances. Turbulent motion can be considered as the superposition of an averaged motion and a fluctuating motion over time:

$$\phi(x_i, t) = \Phi(x_i, t) + \phi'(x_i, t) \tag{3.1}$$

where $\Phi(x_i, t)$ is the average term and $\phi'(x_i, t)$ is the fluctuating term, which is usually lower by many orders of magnitude than the average term. The RANS equations, are obtained by going to apply the Reynolds decomposition, that is, by decomposing the

time-dependent quantities into averaged terms and terms fluctuating terms:

$$\Phi_T(x_i) = \lim_{T\to\infty} \frac{1}{T} \int_t^{t+T} \phi(x_i, t)dt \tag{3.2}$$

Going then to rewrite the Navier-Stokes equations for a compressible flow and substituting the term $\sigma_{ij} = -p\delta_{ij} + \tau_{ij}$, we obtain that:

$$\frac{\partial \rho}{\partial t} + \frac{\partial}{\partial x_i}(\rho u_i) = 0 \tag{3.3}$$

$$\frac{\partial \rho u_i}{\partial t} + \frac{\partial}{\partial x_j}(\rho u_i u_j) = \frac{\partial \sigma_{ij}}{\partial x_i} \tag{3.4}$$

As for the energy equation, it is solved decoupled from the conservation equations of mass and momentum. At this point, each variable is replaced with its mean and fluctuating parts. If the flow is assumed stationary on a macro scale, the mean quantities of the variables are just functions of space:

$$\rho(x_i, t) = \overline{\rho}(x_i) + \rho'(x_i, t) \tag{3.5}$$

$$p(x_i, t) = P(x_i) + p'(x_i, t) \tag{3.6}$$

$$\overline{\rho} u_i(x_i, t) = \overline{\rho} U_i(x_i) + \overline{\rho} u_i'(x_i, t) \tag{3.7}$$

After that, equations 3.5 and 3.7 are substituted in the N-S equations:

$$\frac{\partial}{\partial t}(\overline{\rho} + \rho') + \frac{\partial}{\partial x_i}(\overline{\rho} U_i + \overline{\rho} u_i') = 0 \tag{3.8}$$

$$\frac{\partial}{\partial t}(\overline{\rho} U_i + \overline{\rho} u_i') + \frac{\partial}{\partial x_j}(\overline{\rho} U_i U_j + \overline{\rho} u_i' U_j + \overline{\rho} U_i u_j' + \overline{\rho} u_i' u_j') = -\frac{\partial}{\partial x_i}(P + p') + \frac{\partial}{\partial x_j}(\overline{\tau}_{ij} + \tau_{ij}') \tag{3.9}$$

To finally complete, each term is averaged with respect to time, obtaining:

$$\frac{\partial}{\partial t}(\overline{\overline{\rho}} + \overline{\rho'}) + \frac{\partial}{\partial x_i}(\overline{\overline{\rho} U_i} + \overline{\overline{\rho} u_i'}) = 0 \tag{3.10}$$

$$\frac{\partial}{\partial t}(\overline{\overline{\rho}\overline{U_i}} + \overline{\overline{\rho}\overline{u_i'}}) + \frac{\partial}{\partial x_j}(\overline{\overline{\rho}\overline{U_i}\overline{U_j}} + \overline{\overline{\rho}\overline{u_i'}\overline{U_j}} + \overline{\overline{\rho}\overline{U_i}\overline{u_j'}} + \overline{\overline{\rho}\overline{u_i'}\overline{u_j'}}) = -\frac{\partial}{\partial x_i}(\overline{P} + \overline{p'}) + \frac{\partial}{\partial x_j}(\overline{\overline{\tau}_{ij}} + \overline{\tau_{ij}'}) \tag{3.11}$$

The average of the terms composed of the fluctuating component alone is zero and they are therefore simplified. The RANS equations defined as:

$$\frac{\partial}{\partial x_i}(\overline{\rho}\overline{U_i}) = 0 \tag{3.12}$$

$$\frac{\partial}{\partial x_j}(\overline{\rho}\overline{U_i}\overline{U_j} + \overline{\rho u_i' u_j'}) = -\frac{\partial P}{\partial x_i} + \frac{\partial \overline{\tau_{ij}}}{\partial x_j} \tag{3.13}$$

In equation 3.13 the new term $\overline{\rho u_i' u_j'}$ is commonly brought to the right side of the equation by introducing the negative sign:

$$\frac{\partial}{\partial x_j}(\overline{\rho U_i U_j}) = -\frac{\partial P}{\partial x_i} + \frac{\partial}{\partial x_j}(\overline{\tau_{ij}} - \overline{\rho u_i' u_j'}) \tag{3.14}$$

From a physical point of view, this term represents the time-averaged turbulent momentum transfer rate. It takes the name of Reynolds stress tensor:

$$\tau_{ij} = -\overline{\rho u_i' u_j'} = -\overline{\rho} \begin{bmatrix} \overline{u'^2} & \overline{u'v'} & \overline{u'w'} \\ ... & \overline{v'^2} & \overline{v'w'} \\ ... & ... & \overline{w'^2} \end{bmatrix} \tag{3.15}$$

where $u_i' = [u'v'w']$. this procedure of weighting introduces six new unknowns into the governing equations. Since there are more unknowns than equations, it is necessary to apply an appropriate model of turbulence in order to solve the RANS equations.

3.3. Turbulence model

As mentioned earlier, in order to close the system of RANS equations, it is necessary to choose a turbulence model capable of modeling the stress term of Reynolds. Below we find some of the main turbulence models that are used.

- **Spalart-Allmaras**
- $k - \omega$ **(Wilcox)**

- $k-\omega$ **SST (Menter)**
- $k-kl-\omega$

3.3.1. Spalart-Allmaras

It is a zero-equation model, and one phenomenon that is not suitable for this type of model is that of the highly separated flows. Furthermore, because zero-equation models are not local, i.e. the equation at one point depends on the solution at other points, they cannot be used for unstructured grids. In essence, these types of models, while easy to implement and at low computational cost, they are only suitable for problems of a simple nature. Thus, the Spalart-Allmaras turbulence model is a one-equation model, which calculates the turbulent kinematic viscosity by solving a transport equation. Taking the text of Spalart-Allmaras [31] as a reference, the equation of transport is defined as:

$$\frac{\partial \tilde{\nu}}{\partial t}+u_j\frac{\partial \tilde{\nu}}{\partial x_j}=C_{b1}[1-f_{t2}]\tilde{S}\tilde{\nu}+\frac{1}{\sigma}\nabla[(\nu+\tilde{\nu})\nabla\tilde{\nu}]+C_{b2}|\nabla\tilde{\nu}|^2-[C_{w1}f_w-\frac{C_{b1}}{\kappa^2}f_{t2}](\frac{\tilde{\nu}}{d})^2+f_{t1}\Delta U^2 \tag{3.16}$$

The turbulence viscosity is given by:

$$\nu_t=\tilde{\nu}f_{v1} \tag{3.17}$$

with:

$$\begin{aligned} f_{v1}&=\frac{\chi^3}{\chi^3+C_{v1}^3}\\ \chi&=\frac{\tilde{\nu}}{\nu}\end{aligned} \tag{3.18}$$

The fundamental relations of the model are expressed as follows:

$$\begin{aligned} \tilde{S}&=S+\frac{\tilde{\nu}}{\kappa^2d^2}f_{v2}\\ f_{v2}&=1-\frac{\chi}{1+_{v1}}\\ f_w&=g[\frac{1+c_{w3}^3}{g^6+c_{w3}^3}](1/6)\\ g&=r+c_{w2}(r^6-r)\\ r&=\frac{\tilde{\nu}}{\tilde{S}\kappa^2d^2}\\ f_{t1}&=C_{t3}exp(-Ct4\chi^2)\\ S&=\sqrt{2\Omega_{ij}\Omega_{ij}}\end{aligned} \tag{3.19}$$

The tensor of rotation is:

$$\Omega_{ij} = \frac{1}{2}(\frac{\partial u_i}{\partial u_j} - \frac{\partial u_j}{\partial x_i}) \tag{3.20}$$

$$\begin{gathered}
\sigma = 0.667 \\
\kappa = 0.41 \\
C_{b1} = 0.1355 \\
C_{b2} = 0.622 \\
C_{w1} = 0.56203 \\
C_{w2} = 0.3 \\
C_{w3} = 2 \\
C_{v1} = 0.7.1 \\
C_{t1} = 1 \\
C_{t2} = 2 \\
C_{t3} = 1.1 \\
C_{t4} = 2
\end{gathered} \tag{3.21}$$

This model was created for aerodynamic wall flows, for which low computational cost and good accuracy can be achieved, and for flows with moderate separation/recirculation. The disadvantage is that one cannot handle strong separations, flows without shear and decaying turbulence.

3.3.2. $\kappa - \omega$

The $\kappa - \omega$ turbulence model is a two-equation model, the objective of which is to predict turbulence using two partial differential equations. The first concerns the turbulent kinetic energy k and the second concerns the specific dissipation rate ω. Over the years, several updates to the original model have been made; in the following the latest one will be described, which refers to the Wilcox text [39]. The turbulence viscosity is defined as follows:

$$\nu_t = \frac{\kappa}{\omega} \tag{3.22}$$

and the relations between κ and ω are defined by the two equations:

$$\frac{\partial(\rho\kappa)}{\partial t} + \frac{\partial(\rho u_j \kappa)}{\partial x_j} = \rho - \beta^* \rho\omega\kappa + \frac{\partial}{\partial x_j}\left[\left(\mu + \sigma_k \frac{\rho\kappa}{\omega}\right)\frac{\partial \kappa}{\partial x_j}\right] \tag{3.23}$$

$$\frac{\partial \rho\omega}{\partial t} + \frac{\partial (\rho u_j \omega)}{\partial x_j} = \frac{\alpha\omega}{\kappa} P - \beta\rho\omega^2 + \frac{\partial}{\partial x_j}\left[\left(\mu + \sigma_\omega \frac{\rho\kappa}{\omega}\right)\frac{\partial \omega}{\partial x_j}\right] + \frac{\rho\sigma_d}{\omega}\frac{\partial \kappa}{\partial x_j}\frac{\partial \omega}{\partial x_j} \tag{3.24}$$

following by the coefficients:

$$\sigma_\kappa = 0.6$$
$$\sigma_\omega = 0.5$$
$$\mathrm{C}_\mu = 0.09$$
$$\kappa = 0.4$$

The $\kappa - \omega$ turbulence model is good for predicting the flow behavior on the boundary layer, but it performs worse than the $\kappa - \epsilon$ model when it comes to the free flow. This is due to the strong dependence of the initial values of ω in the free flow.

3.3.3. $\kappa - \omega$ SST

the turbulence model proposed by Menter consists of combining the $\kappa - \omega$ model with $\kappa - \epsilon$. The advantage is that, in the inner region of the boundary layer the robustness of the $\kappa - \omega$ model, while exploiting the independence of the $\kappa - \omega$ model from free flow in the outer regions [20]. First, the $\kappa - \epsilon$ model is transformed into the $\kappa - \omega$ formulation. The differences between this model and the original one consist in the addition of the diffusive term, which appears in the equation of ω, and in the modeling constants. The original model is then multiplied by the fusion function F1, while the modified model is multiplied by the function (1 - F1), after which the two are added together through a combined linear given by the relation:

$$\phi = F_1\phi_1 + (1 - F_1)\phi_2 \tag{3.25}$$

where F_1 and F_2 are defined as:

$$F_1 = tanh(arg_1^4)$$
$$arg_1 = min\left[max\left(\frac{\sqrt{\kappa}}{\beta^*\omega d}, \frac{500\nu}{d^2\omega}\right), \frac{4\rho\sigma_{\omega 2}\kappa}{CD_{\kappa\omega}d^2}\right]$$
$$F_2 = tanh\left(arg_2^2\right)$$
$$arg_2 = max\left(\frac{\sqrt{\kappa}}{\beta^*\omega d}, \frac{500\nu}{d^2\omega}\right)$$

The fusion function will be equal to 1 for $\kappa - \omega$ near the wall (in the original model) and moving away from it, the function will be equal to 0. The parameter ϕ_1 represents any constant of the original model, ϕ_2 any constant of the transformed model, and finally ϕ is

the corresponding constant of the new model. The two partial differential equations that are obtained (for turbulent kinetic energy and for the specific rate of dissipation) are:

$$\frac{\partial(\rho\kappa)}{\partial t} + \frac{\partial(\rho u_j \kappa)}{\partial x_j} = P - \beta * \omega\kappa + \frac{\partial}{\partial x_j}\left[\left(\mu + \sigma_{\kappa t})\bar{t}o\Theta\partial\kappa\partial x_j\right]\right. \tag{3.26}$$

$$\frac{\partial(\rho\omega)}{\partial t} + \frac{\partial(\rho u_j \omega)}{\partial x_j} = \frac{\gamma}{\nu_t}P - \beta\rho\omega^2 + \frac{\partial}{\partial x_j}\left[\left(\mu + \sigma_\omega \mu_t\right)\frac{\partial\omega}{\partial x_j}\right] + 2(1 - F_1)\frac{\rho\sigma_{\omega 2}}{\omega}\frac{\partial\kappa}{\partial x_j}\frac{\partial\omega}{\partial x_j} \tag{3.27}$$

The variables are defined as:

$$P = \tau_{ij}\frac{\partial u_i}{\partial x_j}$$

$$\tau_{ij} = \mu_t\left(2S_{ij} - \tfrac{2}{3}\frac{\partial u_\kappa}{\partial x_\kappa}\delta_{ij}\right) - \tfrac{2}{3}\rho\kappa\delta_{ij}$$

$$S_{ij} = \tfrac{1}{2}\left(\frac{\partial u_i}{\partial x_j} + \frac{\partial u_j}{\partial x_i}\right)$$

$$\mu_t = \frac{\rho a_1 \kappa}{max(a_1\omega, \Omega F_2)}$$

$$CD_{\kappa\omega} = max\left(2\rho\sigma_{\omega 2}\tfrac{1}{\omega}\frac{\partial\kappa}{\partial x_j}\frac{\partial\omega}{\partial x_j}, 10^{-20}\right)$$

$$\gamma_1 = \frac{\beta_1}{\beta*} - \frac{\sigma_{\omega 1}\kappa^2}{\sqrt{\beta^*}}$$

$$\gamma_2 = \frac{\beta_2}{\beta*} - \frac{\sigma_{\omega 2}\kappa^2}{\sqrt{\beta^*}}$$

The constants are:

$$\sigma_{\kappa 1} = 0.85$$
$$\sigma_{\kappa 2} = 1.0$$
$$\sigma_{\omega 1} = 0.65$$
$$\sigma_{\omega 2} = 0.856$$
$$\beta_1 = 0.075$$
$$\beta_2 = 0.0828$$
$$\beta^* = 0.09$$
$$a_1 = 0.31$$

3.3.4. $\kappa - \kappa l - \omega$

The k-kl-omega model is a two-equation model based on turbulent kinetic energy k and turbulent dissipation rate omega. It is a model that arose to overcome the shortcomings of the standard k-omega model with respect to the values of k and omega in the freestream. It is also more accurate in capturing flow separations. The variant implemented on OpenFOAM^{TM} is based on the model written by Langtry-Menter in report [21].

The equation of the model are given by:

$$\frac{D(\rho\omega)}{Dt} = \nabla(\rho D_\omega \nabla\omega) + \frac{\rho\gamma G}{\nu} - \frac{2}{3}\rho\gamma\omega(\nabla u) - \rho\beta\omega^2 - \rho(F_1 - 1)CD_{\kappa\omega} + S_\omega \tag{3.28}$$

$$\frac{D}{Dt}(\rho\kappa) = \nabla(\rho D_\kappa \nabla\kappa) + \rho G - \frac{2}{3}\rho\kappa(\nabla u) - \rho\beta^*\omega\kappa + S_\kappa \tag{3.29}$$

The turbulence viscosity can be calculated with:

$$\nu_t = a_1 \frac{\kappa}{max(a_1\omega, b_1 F_{23} S)} \tag{3.30}$$

An the default model coefficients are:

$$\alpha_{\kappa 1} = 0.85$$

$$\alpha_{\kappa 2} = 1$$

$$\alpha_{\omega 1} = 0.5$$

$$\alpha_{\omega 2} = 0.856$$

$$\beta_1 = 0.075$$

$$\beta_2 = 0.0828$$

$$\gamma_1 = 0.556$$

$$\gamma_2 = 0.44$$

3.4. Boundary Layer

Every body immersed in a fluid has on its surface a thin layer of fluid called the boundary layer, within which viscous effects cannot be neglected. The boundary layer varies significantly on the surface, of a wing or airfoil, presenting an initial laminar region, a subsequent turbulent region and an eventual separation. This phenomenon results in the need to model turbulence in areas near the body wall and is studied by defining of the local Reynolds number y^+.

y^+

Aerodynamic studies state that, in general, a turbulent boundary layer can be divided into two main regions: an inner region, comprising 10-20 % of the total thickness total of the boundary layer and an outer region. The inner region consists of two zones different: a viscous sublayer, in which the velocity profile is conditioned by shear forces viscous, and a completely turbulent layer, separated by a transition/buffer layer region. Referring to the 'law of the wall', the velocity profile is given by $u^+ = y^+$ in the viscous sublayer, and $u^+ = \frac{1}{\kappa} \ln y^+ + B$ in the turbulent or logarithmic layer, where k and B are constant. The parameter y^+ represents therefore the non-dimensional distance from the wall and allows the characteristic dimensions of the boundary layer to be derived [5]. y^+ is calculated from the equation:

$$y^+ = \frac{u_\tau y}{\nu} \tag{3.31}$$

where ν is the kinematic viscosity, y is the distance from the wall, ρ is the density and u_τ is the friction speed given by the shear stress close to the wall τ_w

$$u_\tau = \sqrt{\tau_w / \rho} \tag{3.32}$$

For $y^+ < 5$ the cell resides in the viscous sublayer, where $u/u_\tau = y^+$, and for $y^+ > 30$ the flow lies in the low-logarithmic region [10], as depicted in Figure 3.2:

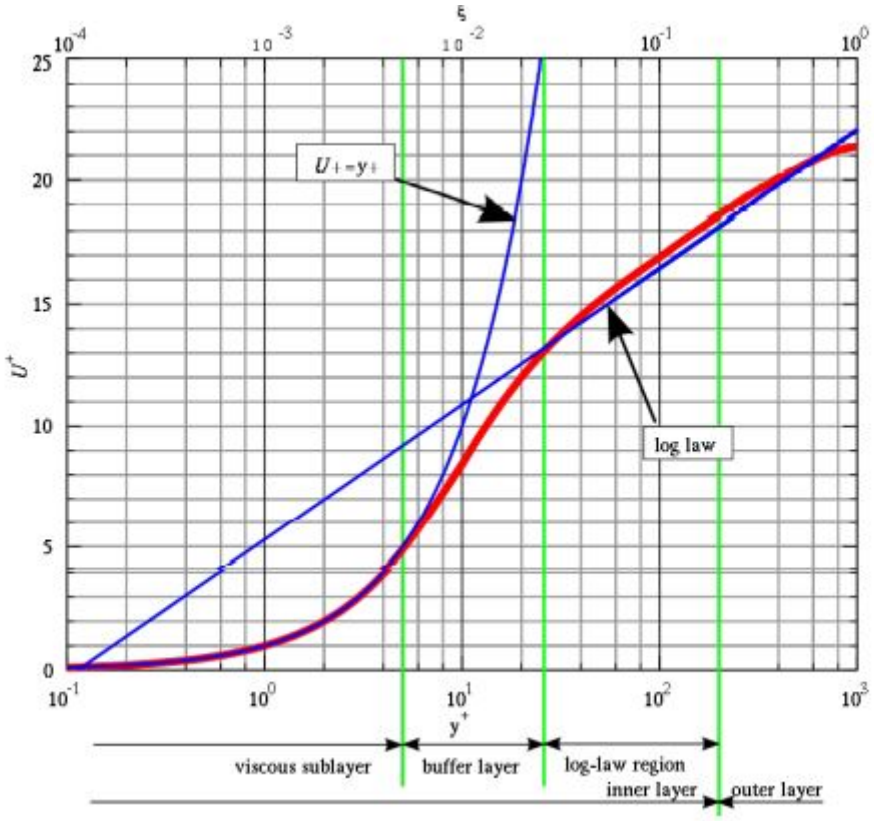

Figure 3.2: Law of the wall

The reference thickness of the first layer is then derived from the coefficient of friction, C_f, defined as:

$$C_f = \frac{0.058}{Re^{0.2}} \tag{3.33}$$

Approximating the flux on the profile to the boundary layer on a plane sheet, and considering the wall shear stress:

$$\tau_w = \frac{1}{2}\rho U_\infty^2 C_f \tag{3.34}$$

wall functions

Wall functions are used to reduce the amount of cells needed to solve a domain, since the viscous sublayer is not completely solved near the of the walls. The first computational node, on the other hand, is located at about $30 < y+ < 100$ in the low-logarithmic region. However, using this approach, some problems in the separation and attachment regions.

4 | Airfoil selection

As explained briefly in the introduction, in this chapter we will deal with a preliminary study in a two-dimensional domain. We will examine three different profiles who's intended use is very different one from the other. Infact:

- NACA0012: is a symmetrical profile of the 4-digit naca series very popular in the aerospace sector for the construction of blades.
- E387: non-symmetrical Eppler profile designed for low Reynolds number conditions.
- MSHD: high-lift profile for low Reynolds numbers obtained through optimization using PROFOIL in the Report[16].

In this chapter we will try to analyze the behavior of these three profiles, comparing their coefficients as the angle of attack varies and looking more generally at the motion and pressure field around them. As mentioned in the introduction, we expect to find differences not only in terms of coefficients but also in behavior near the stall[16]. The objective is therefore a preliminary analysis confined to 2d before starting 3d studies and see how these three very different profiles behave in a three-dimensional current. Flow at low Reynolds numbers is quite difficult to simulate in fact one has to deal with laminar, turbulent flows, transitions, separated flows and large wakes. The laminar boundary layer created on the front is influenced by the adverse pressure gradient downstream of the pressure peak on the profile. Because of this, the flux tends to separate forming a laminar shear layer which is not really a free shear layer because it still remains very close to the surface of the profile which therefore makes it more stable, however it is certainly not as stable as a boundary layer completely attached to the profile. This initial shear layer often gets affected by disturbances present in the flow itself and turns into a turbulent shear layer. The turbulent boundary layer acquires momentum very rapidly from the external flow and thickens rapidly, after which this turbulent shear layer makes contact with the profile and thus a turbulent boundary layer attached to the profile is created, ending the transition. If the shear layer does not reattach to the profile, a subcritical flow characterized by a broad wake is obtained. In a sense, the shear layer encloses a zone of flow adhering to the profile that is called the laminar separation bubble (Figure: 4.1),

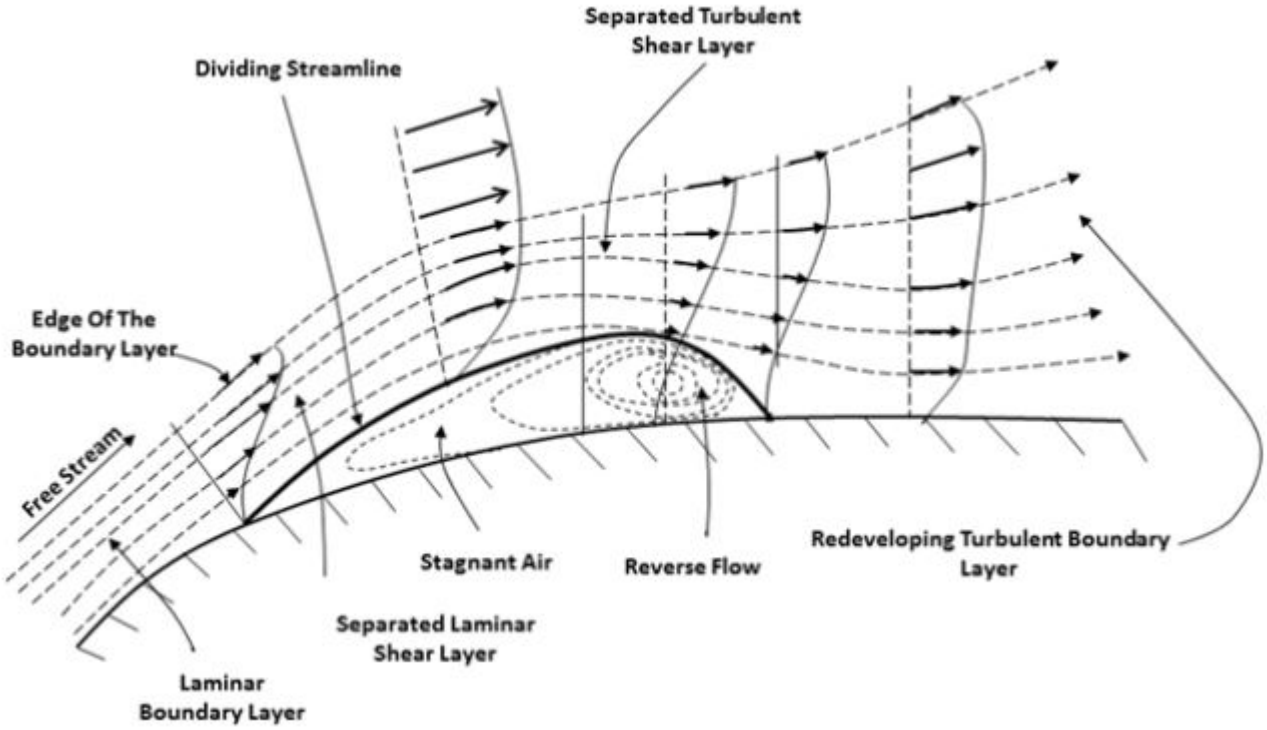

Figure 4.1: Separation bubble phenomenology

within which the flow has recirculation zones. This separation bubble generally translates in terms of performance with reduced lift and increased drag compared to a case where the flow remains totally attached.

Another phenomenon characteristic of aerodynamic. This phenomenon occurs when there is different behavior of the separation bubble depending on whether we are increasing or decreasing the angle of attack, this affects the aerodynamic coefficients and can create stability and control problems on vehicles operating in this Reynolds regime We can recognize two main types of hysteresis: pre-stall hysteresis and stall hysteresis. In the first case we have separation bubbles located in the middle of the chord, if we increase the angle of attack the transition point occurs further upstream and a separation bubble is created closer to the leading edges, at this point we decrease the angle of attack the separation bubble returns to its initial position in the middle of the chord but with a lower angle of attack. On the other hand, the other case is characterized by a separation bubble close to the leading edge, if we increase the angle of attack the bubble bursts and extends along the entire profile without reattaching, completely changing the pressure distribution on the profile and causing the coefficients to collapse. If we decrease the angle of attack, the bubble returns to its initial position but at a lower angle of attack.

4.1. Problem geometry and setup

First of all we start by defining the geometry of the domain. We have chosen a chord equal to c = 0.15m at a velocity of the current 30m/s thus obtaining a Reynolds number equal to 300000. Below we find a Figure 4.2 that represents the domain of interest. The domain is rectangular-shape and the profile is positioned in the middle and we consider the leading edge as the origin of the Cartesian plane. The flow runs from left to right in the X direction, the left wall is 8 times the chord from the leading edge and the right wall is 15 times the chord. In the Y direction the top and bottom walls are distant 6 times the chord form the profile. With these measures we can consider the domain sufficiently large to: eliminate any effect of proximity to the wall, give sufficient space for the flow to develop before investing the profile and leave the wake free to evolve downstream of the profile. In order to analyze the behavior of the profile when the angle of attack varies, we preferred to rotate the profile and maintain horizontal the direction of the flow rather than the opposite, this because, despite having to repeat the mesh for each angle of attack, once automated the process, the work was less sensible to the risk of human errors. This was possible through the 'Rotate' function of the external mesher Gmesh, which allows the imported profile to rotate around the origin of the axes, coincident with the leading edge of the profile. OpenFOAM^{TM} has been programmed to always work with a three-dimensional domain even for 2d studies. For this reason, using Gmesh (software for the generation of two-dimensional meshes) we had to use the OpenFOAM^{TM} function called 'ExtrudeMesh' which allows the 2d mesh created initially to be extruded in the Z direction to work in OpenFOAM^{TM}. In fact, in the Z direction the domain has the thickness of a single cell of the mesh and the 'Empty' conditions are added on the FRONT / BACK faces that impose zero speed in the direction orthogonal to the faces,suche as the Z direction.

Boundary conditions:

Regarding the boundary conditions we find:

- INLET: 'FixedValue' conditions for the speed, set at 30m / s and 'ZeroGradient' for the Pressure.
- OUTLET: 'FixedValue' with null value for the Pressure, and 'ZeroGradient' for the speed.
- UP / DOWN: 'Symmetry' type condition for both pressure and speed.
- FRONT / BACK: 'Empty' conditions for pressure and speed.
- AIRFOIL: 'No-Slip' for speed and 'ZeroGradient' for Pressure.

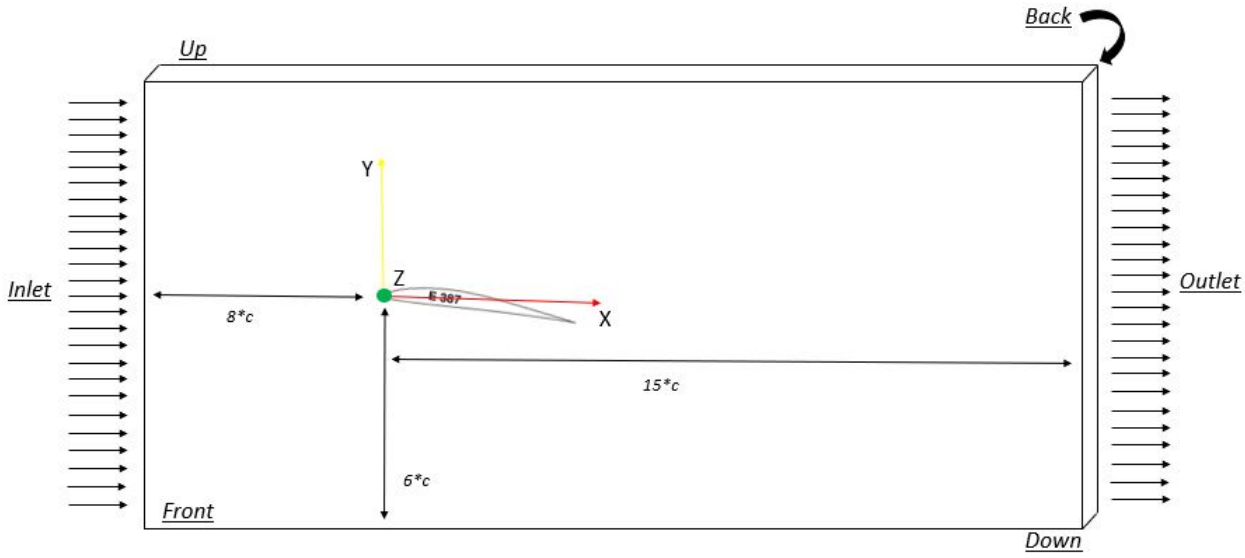

Figure 4.2: Numerical domain for airfoil section studies

Initial conditions

Below are the initial conditions used for the turbulence parameters required by the turbulence models used. Starting from the reference data in the report [7] of a tunnel with a test chamber of area $A = 0.974m^2$ we obtain a hydraulic diameter equal to $D_h = 1.11m$ and an intensity of turbulence I=0.58% we can calculate the following:

- Turbulence length scale: $L_t = 0.038 * D_h = 0.042m$
- Modified Turbulence viscosity: $Nu_{tilda} = \sqrt{1.5} * I * u * L_t$
- Turbulence energy: $k = 1.5 * u^2 * 0.01^2 = 0.09$
- Dissipation rate: $\epsilon = \frac{0.1643 * k^{1}.5}{L_t} = 0.11$
- Specific dissipation rate: $\omega = \frac{\sqrt{k}}{L_t} = 7.23$
- $\omega_{wall} = \frac{60 * 0{,}000015}{0{,}075 * y+^2} = 77169971$

4.2. Mesh generation and description

For this 2d study study we used Gmsh as software to build the mesh. Gmsh is an opensource software for the generation of finite element meshes with integrated post-processing. Gmsh is built around 4 modules: geometry, mesh, solver and post-processing. The setup of the inputs to generate a mesh can be done in the following ways: by using the graphical user interface, by writing a mesh.geo text file in ASCII format that can be done either by hand or by a calculation program or external like C ++, Matlab™ etc ... Actually for this reason in this case we have chosen to use Gmsh and not the internal mesher of OpenFOAM™ (SnappyHexMesh), in fact we have created a small Matlab script with a small user interface for a more user-friendly use (Figure: 4.3) that generates the mesh.geo text file for Gmsh. This work helped us to automate the process of writing the mesh.geo file, which is essential if we want to test some modifications to the geometric parameters. As we can see in Figure 4.3 we can set the desired y+ value in order to capture well also the behavior of the current in the areas near the walls, and then play with the size of the elements close to the profile, the thickness of the boundary layer and the number of elements on the fan on the trailing edge.

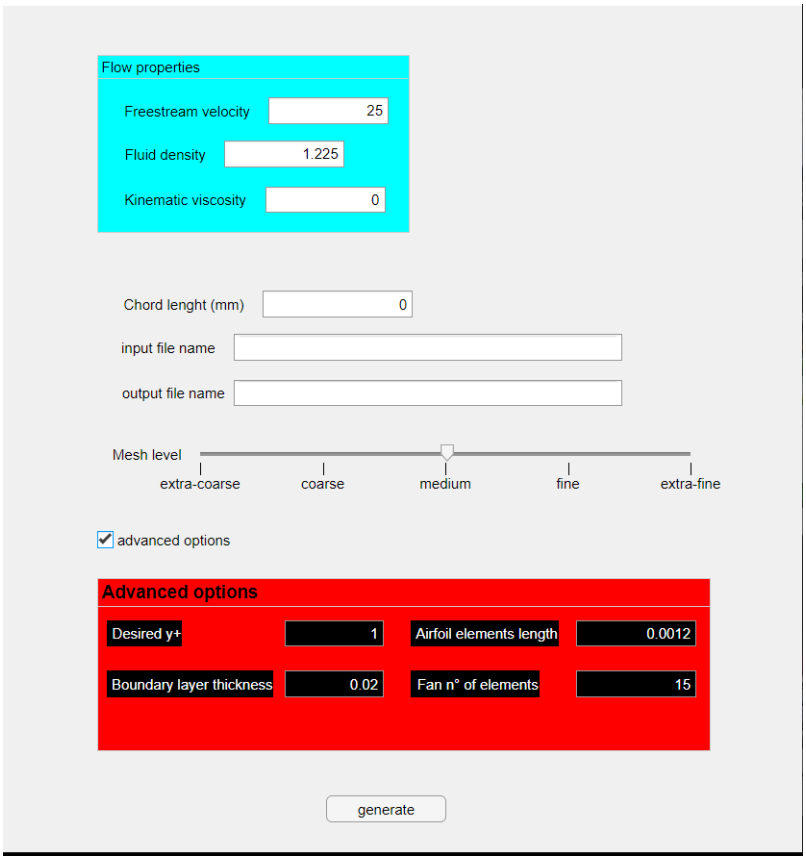

Figure 4.3: Matlab™ program interface for mesh.geo file generation

The mesh is an Unstructured mesh because writing the code for generating the mesh.geo file would have been too complex in the case of a fully structured mesh. In reality, more precisely, the mesh in question is a hybrid mesh (Figure: 4.4) characterized by an unstructured part away from the profile and a structured part around the profile in order to better capture the flow field within the boundary layer. To further improve the quality of the mesh, as we can see in the Figure 4.4 on the right, the presence of a rectangular-shaped refinement box not too far from the profile, this will certainly increase the time for Gmesh to generate the mesh and the time of the actual simulation but guarantees greater consistency of the results. We would like to say that with a hybrid mesh of this type we do not expect a perfect analysis of what happens in the wake, compared to a fully structured mesh, so we expect from the beginning not to be able to obtain the extremely precise results in terms of Drag.

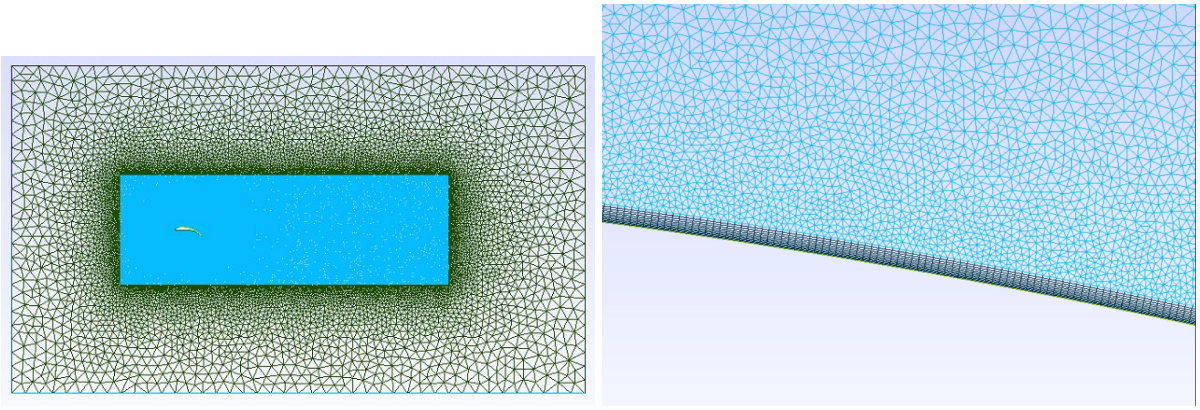

Figure 4.4: Hybrid mesh used for 2d studies

In Figure: 4.5 is shown the structured part of the mesh composed by rectangular elements of small thickness close to the profile gradually increasing with an expansion ratio slightly higher than 1 in order to have a thickness transition of the layers as gradual as possible up to the last layer whose thickness is comparable to the size of the first elements of the unstructured part of the mesh. near the Trailing edge we find a fan where the size of the elements of each layer is clearly distorted, in fact we have tried to choose a number of elements of the fan so that the aspect ratio of the elements inside the fan does not deviate too much from those on the back and of the profile.

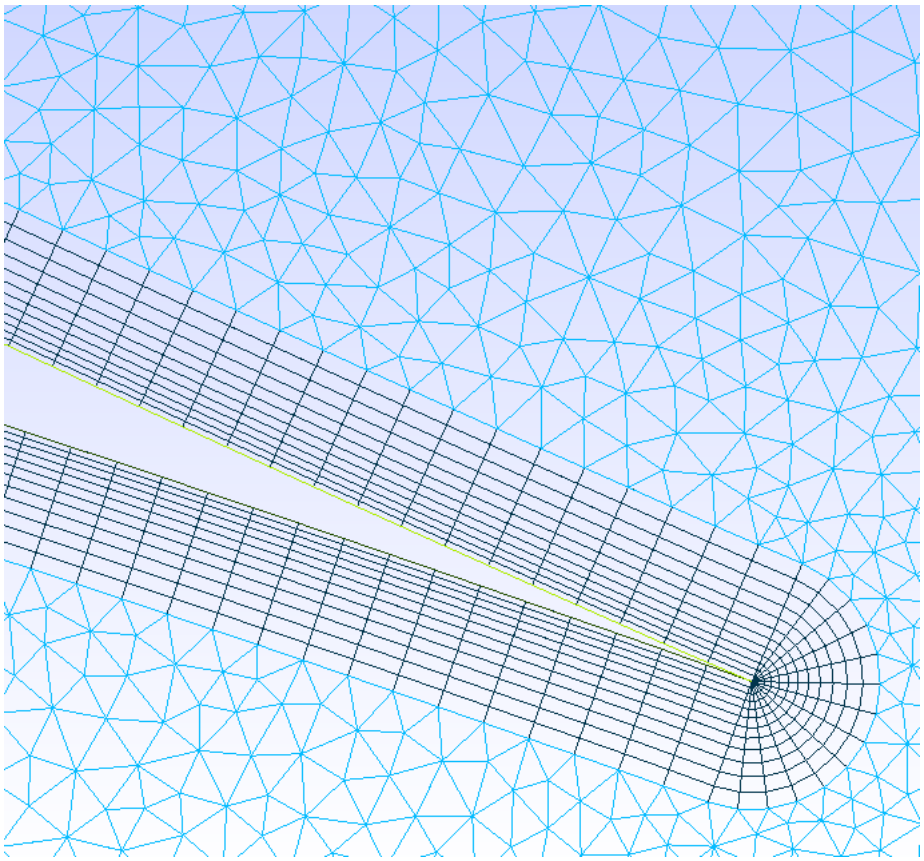

Figure 4.5: trailing edge layers of hybrid mesh for 2d studies

4.3. Grid convergence

Once the computational model was created, we tried to change some mesh settings and see the dependence of the results in terms of Cl and Cd. In particular, we went to thicken the mesh more and more while keeping an eye on the results. In fact, we have created 4 different meshes listed in the table starting from Mesh 1 with 101920 elements and the thickness of the first layer on the profile equal to 8e-5m arriving to Mesh 4 which has 450500 elements and a thickness of the first layer 8 times smaller which guarantees us a Y+ value of 2.8. What we expect is a variation in the results the function of mesh refinement up to a certain value, beyond which the results no longer change substantially if we continue to refine the mesh. In this way we can make sure of the consistency of the results of the simulations as they remain constant as the mesh size changes. This analysis was done at two angles of incidence (0 and 7 degrees) so that we could be more than sure that the model did not have disagreeing behaviors when different initial conditions were examined. As we can see in the table: 4.1 and in the Figure: 5.7 we notice how the coefficients vary initially starting from the most coarse mesh until they stabilize on one value if we compare mesh 3 and mesh 4. This is more noticeable on the Cd values while as for Cl we notice less variation if we compare the most coarse mesh with the finest mesh. At this point to continue our analysis of the profiles we choose mesh 3 as the mesh to be used as it seems to us a good compromise between results obtained (in agreement with mesh 4) but with a lower computational cost.

Grid convergence

	mesh 1	**mesh 2**	**mesh 3**	**mesh 4**
N° elements	101920	155871	248676	450500
1st layer th.	8e-5	4e-5	2e-5	1e-5
Y+	10	7.1	4.4	2.8
Cl 0°	0.371	0.366	0.362	0.36
Cd 0°	0.009	0.011	0.013	0.013
Cl 7°	1.09	1.084	1.077	1.067
Cd 7°	0.018	0.019	0.021	0.021

Table 4.1: Grid convergence

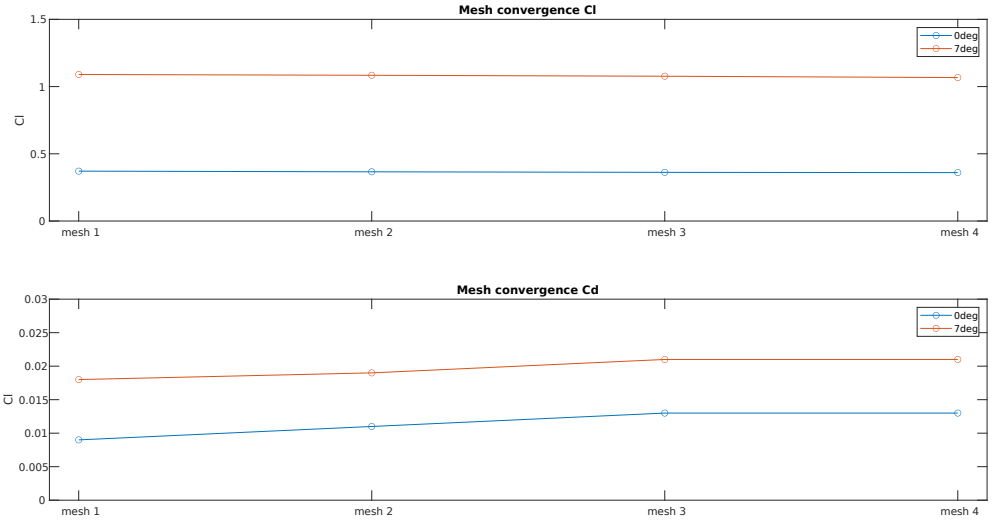

Figure 4.6: Grid convergence for airfoil section studies

4.4. Solver and simulation parameters

Within OpenFOAM^{TM} it is possible to set the equation solver for the simulation, change the settings of convergence or choose the temporal integration scheme for dynamic simulations transient. For this study since we are in the incompressible field we mainly used SimpleFoam as a solver for stationary simulations. Only in a few cases (to better capture vortices near the stall) we decided to use PisoFoam which is instead an instationary solver for the incompressible. Each simulation was initialized with potentiaFoam, so the momentum field is solved by assuming a current at potential for the first iterations in order to best address simpleFoam in the first part of the simulation. Similarly was done with PimpleFoam, in fact all the instationary simulations were initialized with simpleFoam for the first few hundred iterations. Below we find summarized the main settings of the simulations we used.

Solvers

The equation solvers, tolerances and algorithms are controlled from the fvSolution dictionary in the system directory. As for solvers we used GAMG (generalised geometric-algebraic multi-grid) for pressure and ϕ, GaussSeidel as smoother with tolerance 1e-7 and reltol 0.01. While for κ and omega velocity we used PBiCG (preconditioned bi-conjugate gradient) with DILU preconditioner with tolerance 1e-8 and reltol 0.001.

Numerical Schemes

In the fvScheme section, again within the System directory, we find instead the possibility of setting the numerical schemes to be applied to the derivatives of the system. OpenFOAM^{TM} gives us great freedom to choose from a wide selection of numerical schemes for different derivatives or interpolation of values. First, after choosing a standard Gaussian finite-volume integration type (the most common choice), one can decide to individually set the interpolation scheme for each term. Once again to facilitate stability and convergence, many simulations, especially the most unstable ones e.g. at high angles of attack, were run using first-order schemes and then switched to second-order. Below in the tables we find summarized the schemes used in both cases:

Divergence scheme	**1°order**
$\mathbf{div}(\phi, U)$	*Gauss upwind grad(U);*
$\mathbf{div}(\phi, \kappa)$	*Gaussupwind grad(*κ*);*
$\mathbf{div}(\phi, \omega)$	*Gauss upwind grad(*ω*);*
$\mathbf{div}((\nu Eff^{*} dev2(T(grad(U)))))$	*Gauss linear;*

Table 4.2: 1° order schemes

Divergence scheme	**2°order**
$\mathbf{div}(\phi, U)$	*Gauss linearUpwind grad(U);*
$\mathbf{div}(\phi, \kappa)$	*Gauss limitedLinear 1;*
$\mathbf{div}(\phi, \omega)$	*Gauss limitedLinear 1;*
$\mathbf{div}((\nu Eff^{*} dev2(T(grad(U)))))$	*Gauss linear;*

Table 4.3: 2° order schemes

CFL number

Many simulations, especially near the stall are unsteady simulations, and because of this we had to appropriately set the duration of individual time steps to be in agreement with the CFL condition. The Courant-Friedrich-Lewy condition is a numerical constraint that determines the time step allowed for a specific grid size. This constraint dictates that the information can propagate no more than one cell away from the previous cell. When explicit patterns are used, for example, this constraint is necessary for convergence. If the information propagates with the rate, then the CFL number is given by the following equation, which is valid for the one-dimensional case.

$$\tilde{u} = \frac{\Delta t}{\Delta x} < C \tag{4.1}$$

Where C is the number that determines the CFL condition. For explicit patterns (like pisoFoam) it is necessary have C < 1, while the value may be greater for implicit patterns. Since we used pimpleFoam, we were able to set an adaptive timestep based on the size of the elements so that the maximum number of CFL is always kept below 10.

Residuals control

The residual is one of the most important measures of the convergence of an iterative solution, since it directly quantifies the error in the solution of the system of equations. In a CFD analysis, this parameter measures the local imbalance of a conserved variable in each control volume. The residual also will never be exactly zero, however, the smaller its value, the more accurate the solution is numerically. We imposed the following convergence criteria on the residuals for our simulations:

residual tolerace

Parameter	value
U	*1e-6*
p	*1e-5*
κ	*1e-5*
ϵ	*1e-5*
ω	*1e-5*

Table 4.4: residual tolerance

In addition, to make sure that the simulations were yielding sensible results, we looked at the trend of the coefficients over time and made sure that they stabilized on a value while the residuals fell to imposed tolerance. To help us that this was happening we had to manipulate the Relaxation Factors. These are specific to each magnitude and can take a value between 0 and 1. the higher this number is the faster the convergence will be but the less stable the results will be, with the risk that it will blow up; the closer the number is to 0 the slower but more stable the simulation will be. We manipulated these values several times to finally arrive at this compromise, which was maintained later:

relaxation Factors

Parameter	value
U	*0.6*
p	*0.3*
κ	*0.4*
ϵ	*0.4*
ω	*0.4*

Table 4.5: relaxation factors

4.4.1. Model validation

the validation of our 2d model has been conducted comparing the CFD results of E387 airfoil with the experimental test at low Reynolds numbers by Nasa [7].

Wind Tunnel

The wind tunnel used is the low speed low turbulence wind tunnel designed by F.N.M. Brown for low speed flow visualization(Figure 4.7). The tunnel is an open-circuit tunnel with a squared cross section through the inlet and the test section with a transition to circular section by a diffuser. the contraction ratio at the inlet is 21:1 in fact it starts from a square section of 2.95m to a square section of 0.61x0.61m in 1.48m. Upstream of the inlet are 12 anti-turbulence screens, and the test chamber is constructed of 3 glass panels and one (on the back) of plexiglass with the profile support; the dimensions of the test chamber are 0.61x0.61x1.83m. Downstream of the test chamber we find a diffuser with an angle of 4.2° and then a motor section with a 1.2m diameter 8-blade propeller

powered by a variable speed AC motor with maximum power of 18.6kW.

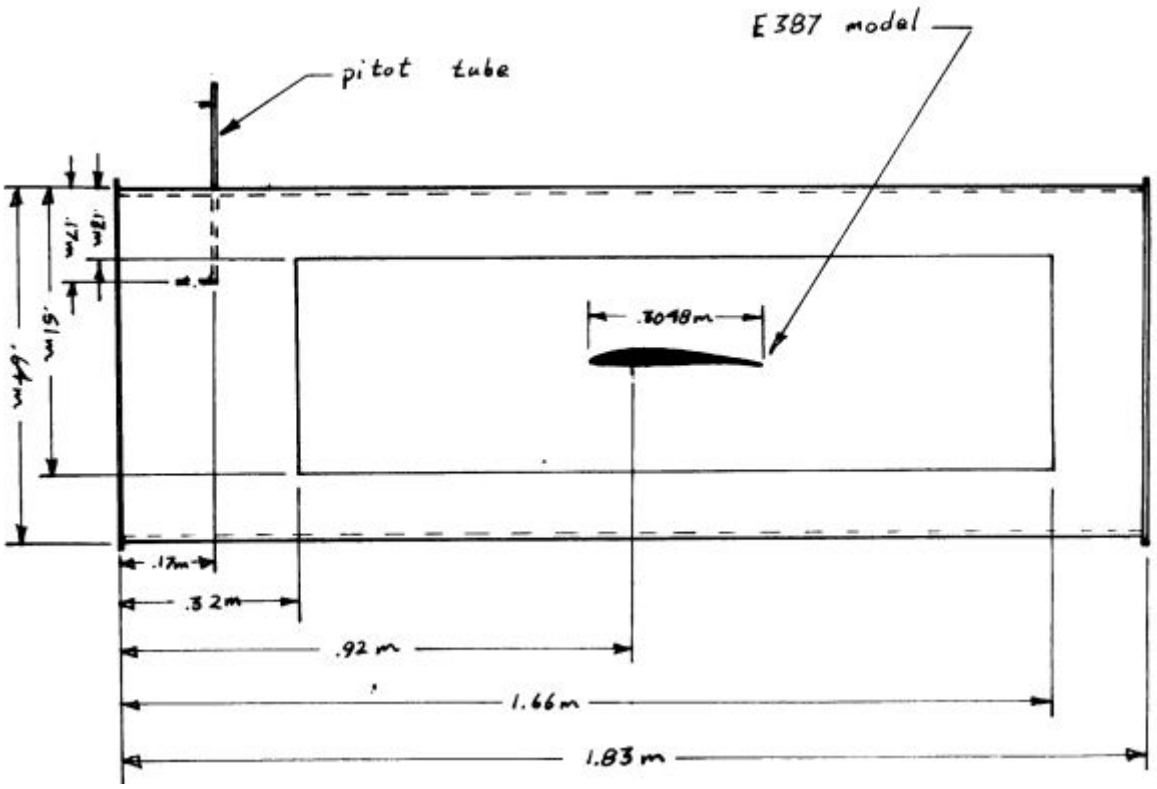

Figure 4.7: F.N.M. Brown Wind tunnel

Airfoil model

Models of the Eppler E387 profile were built in the laboratory by carving a mold from a solid aluminum block into which to pour epoxy resin that took the shape of the profile. The coordinates of the E387 profile were taken from NASA Langley. The model has an aperture of 0.406m and is mounted in the center of the test chamber between two 0.61x0.61m plexiglass endplates, these endplates have a beveled leading edge and are positioned so that the leading edge is 0.267m away from the position of the quarter chord of the profile. There are 66 static pressure sockets in the model with size of 0.79mm in diameter and normal to the surface of the profile, they are connected by teflon tubes with inner diameter of 1.27mm and outer diameter of 1.78mm.

Pressure distribution

Regarding the comparison of our results on the E387 profile with the data obtained from the wind tunnel, we focused on the pressure distribution along the chord of the profile in addition to the aerodynamic coefficients plotted later with the Cl-alpha curve and polar. Let us first analyze the pressure coefficient distribution along the profile: this analysis was done for different angles of attack (0deg 7deg and 10deg) so as to be sure that the model and results were independent of the angle of incidence. In the following figures: 4.8, 4.9, 4.10 we note how there is satisfactory agreement of the results obtained with OpenFOAM^{TM} and the tunnel values, for much of the graph the two Cp curves overlap. On the other hand, there is discordance especially near the leading edge and in the second half of the chord moving toward the trailing edge where the tunnel data present a step that is not present in our model. This step is due to the presence of the separation bubble that the pressure sockets in the tunnel model are able to capture while our model does not notice it. This separation bubble is seen by the pressure sockets with a collapse of Cp followed by a pressure plateau. the position of the pressure plateau coincides with the position of the laminar part of the separation bubble. We can further differentiate based on the size of the separation bubble, short separation bubbles perturb the pressure distribution little while larger separation bubbles change the pressure distribution more significantly and thicken a turbulent boundary layer that is more prone to separation causing drag increase and lift collapse. As we can see from the graphs 4.8, 4.9, 4.10 we can see different flow behaviors as the angle of attack changes. In particular looking at the pressure distribution at 0 deg AoA it is very evident the separation bubble captured by the tunnel at 70-80 percent of the chord while at larger angles of attack we do not find the step caused by the separation bubble.

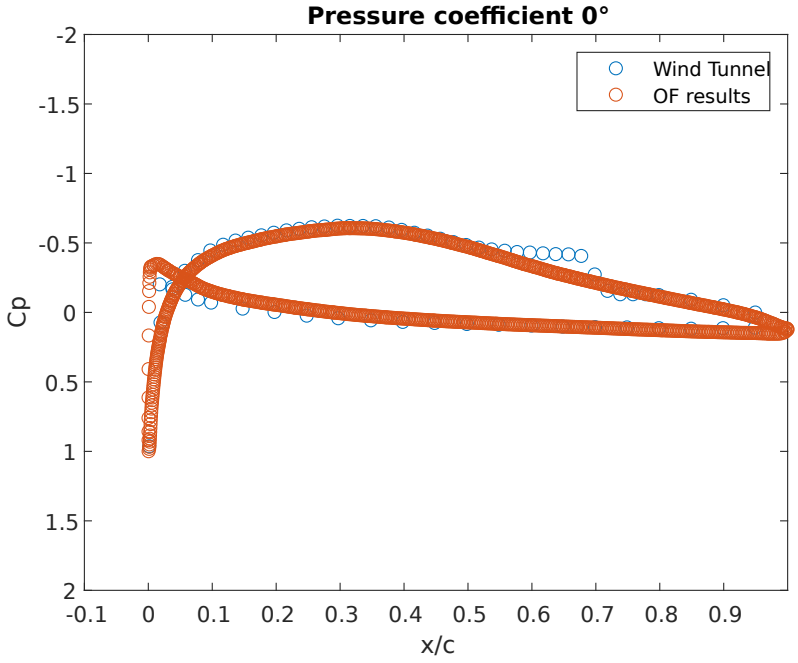

Figure 4.8: Comparison between validation data and OpenFOAM™ results of pressure coefficient distribution for E387 airfoil at 0° AoA

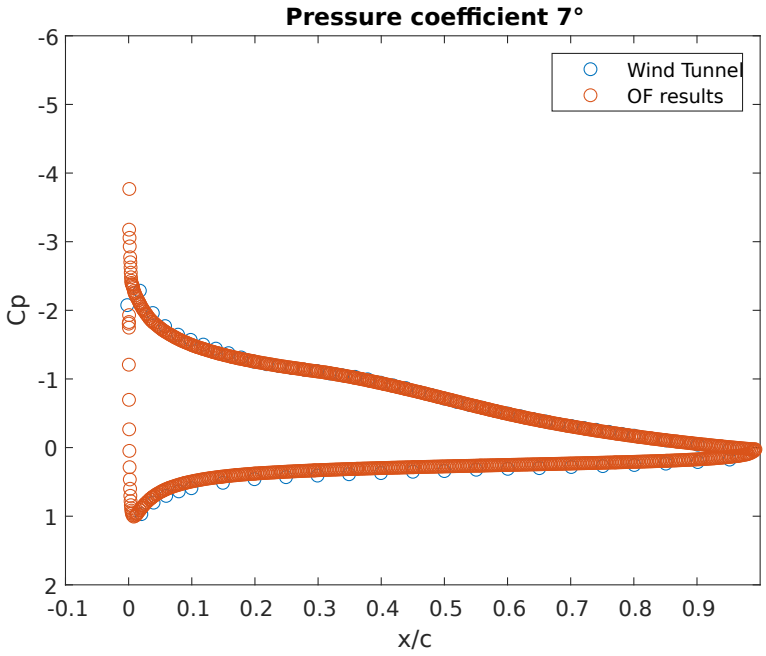

Figure 4.9: Comparison between validation data and OpenFOAM™ results of pressure coefficient distribution for E387 airfoil at 7° AoA

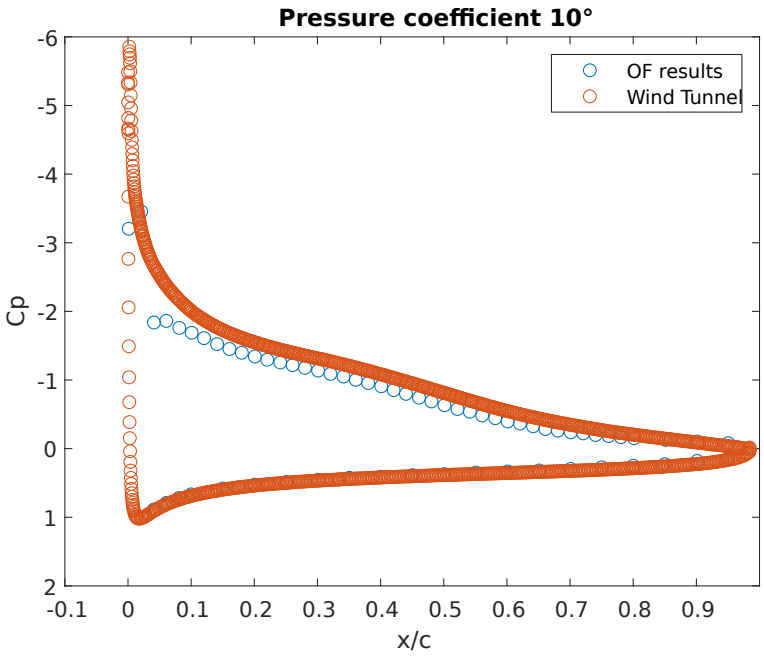

Figure 4.10: Comparison between validation data and OpenFOAM™ results of pressure coefficient distribution for E387 airfoil at 10° AoA

Since at high angles of attack the simpleFoam steady-state current solver struggled to achieve convergence of the residuals we opted for an unsteady solver such as pimpleFoam. To be sure of the results obtained from the latter, we decided to compare some data obtained with simpleFoam and pimpleFoam. The following image plots the pressure distribution at an angle of attack of 4 deg obtained by simpleFoam and pimpleFoam; we can be fully satisfied with both setups as the two curves practically overlap.

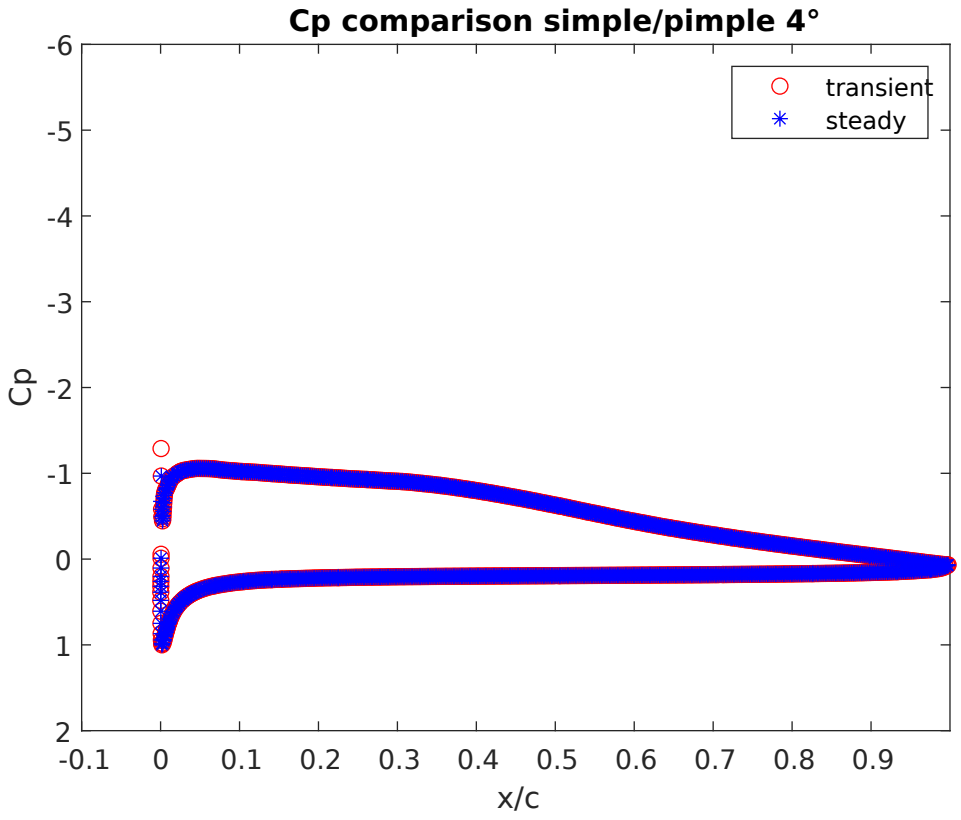

Figure 4.11: simpleFoam and pimpleFoam comparison on pressure coefficient distribution

In the graph below, on the other hand, we finally find the Cl- curve. As we can see the results obtained through OpenFOAM^{TM} turn out to be totally in agreement with the tunnel data, even in the most difficult zone i.e. near the stall. Once again we would like to mention that for low angles of attack the stationary simulations were solved by simpleFoam while near the stall where more instability is present it was necessary to use pimpleFoam. As mentioned before to be sure that pimpleFoam was set correctly it was also tested at 4 deg AoA and again it is consistent with the results of simpleFoam.

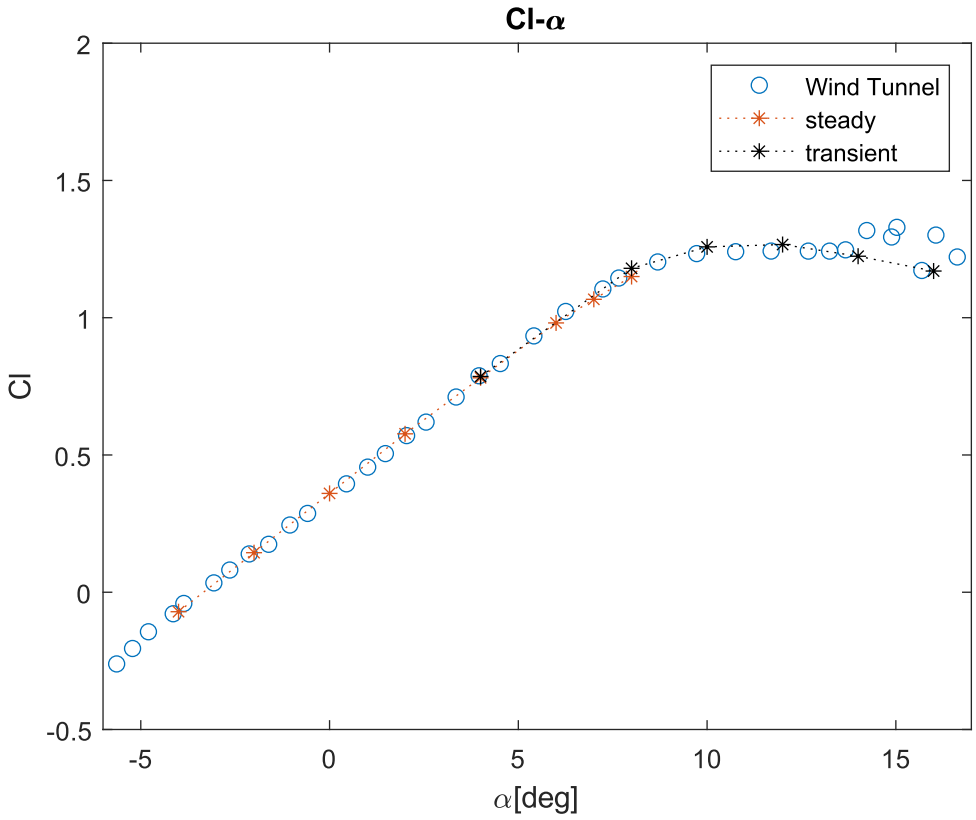

Figure 4.12: E387 Cl-α comparison between OpenFOAM^{TM} and wind tunnel results

Instead, in figure 4.13 we find the polar curve plotted. It can be seen that the two curves deviate mainly due to an overestimation of the drag coefficient of our model compared to the tunnel data.

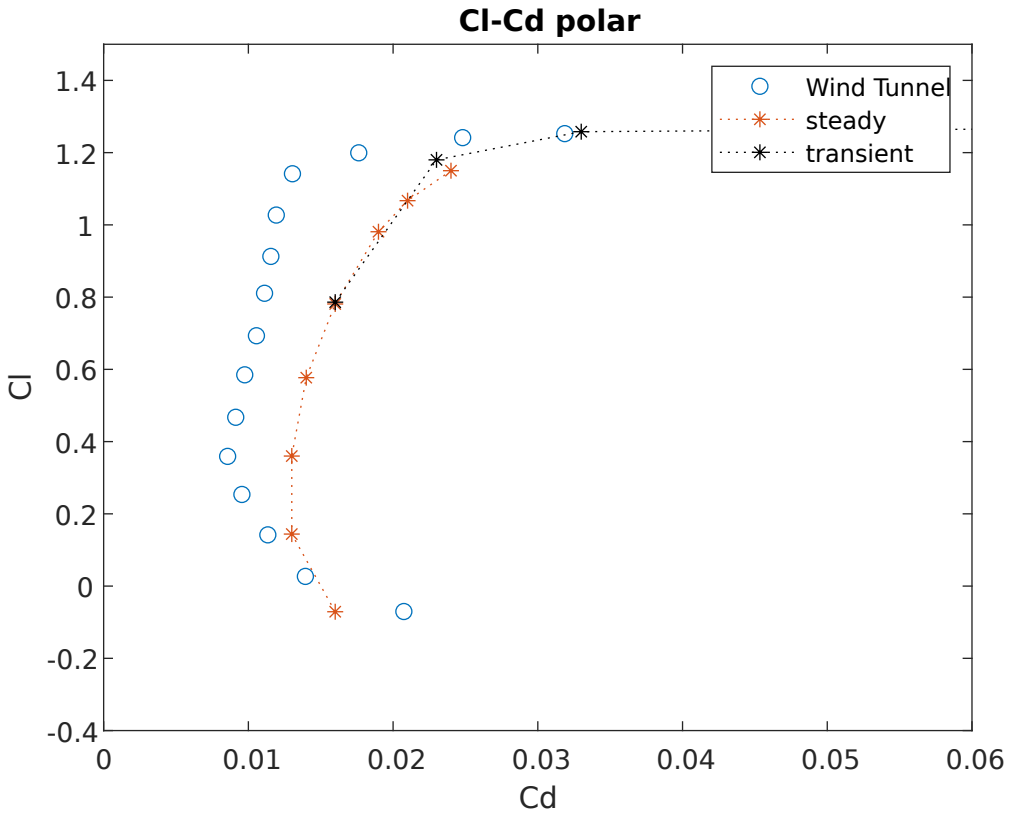

Figure 4.13: E387 Cl-Cd comparison between OpenFOAM^{TM} and wind tunnel results

4.4.2. Results

In the picture 4.14 the geometries of the three different profiles are compared, we can see that the thickness of the mshd profile is higher than the others and the point of maximum thickness is reached earlier, already at 0.163 x/c. and the maximum camber is much higher than the other two (the naca0012 is even symmetrical)

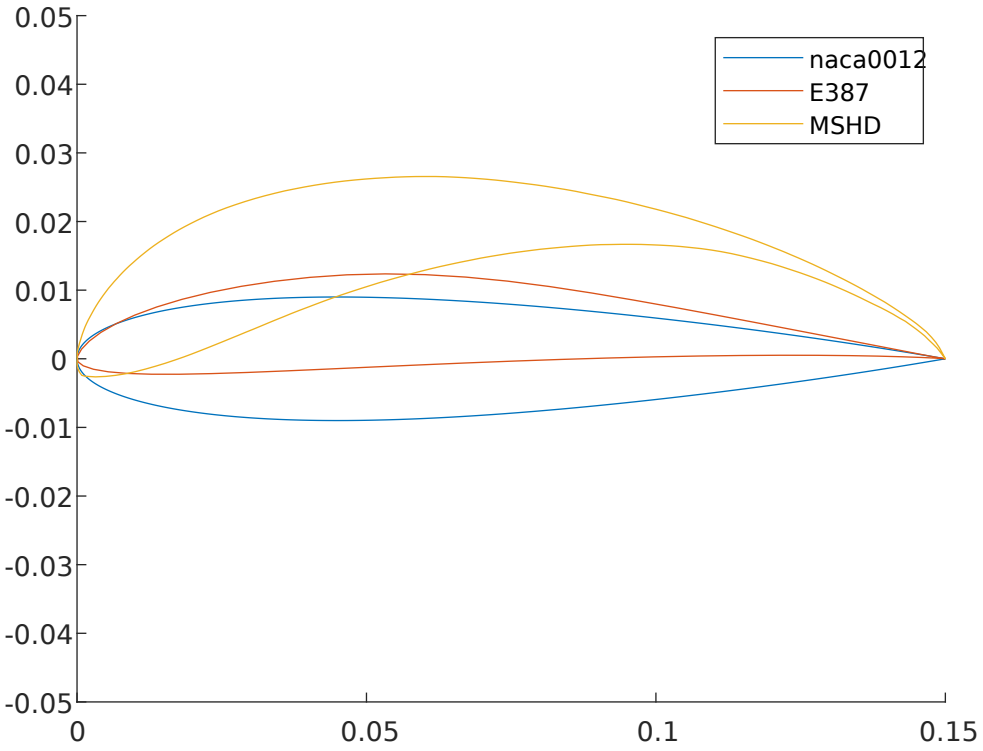

Figure 4.14: Tested airfoils geometry

In addition, the high camber of the mshd profile is designed to provide more aft loading considering what was mentioned in the report [33], that is, using aft loading as the main direction for the design d high lift profiles for motorsport applications. In addition, the mshd has a fairly high leading edge radius compared to the other two profiles, this is to release the performance of the profile from the peak pressure going to the back. The thickness of the profile is concetrated mainly anteriorly when compared with the others and this affects the behavior of the profile to have a 'soft stall' behaviour [33] by moving the position of the boundary layer transition forward, in this way the position of the minimum Cp is shifted further forward so as to anticipate the adverse pressure gradient.

Cl-α

In the following graph, the Cl-α curves of the three profiles are plotted so that all three can be compared together. The first thing that stands out is the overall performance of the mshd compared to the other profiles both in terms of lift and in terms of the range of possible angles of attack. The maximum Cl is considerably higher and at a significantly higher angle of attack, this gives us the possibility of greater 'adjustability' when mounting the wing. High downforce is possible even beyond Cl max, this is due to the 'soft stall' behavior when compared to the other two, in fact it reaches a maximum lift value and then decreases quite smoothly, moreover we can see that the growth as the angle of attack changes is very smooth, in fact already at low angles we have high lift values.

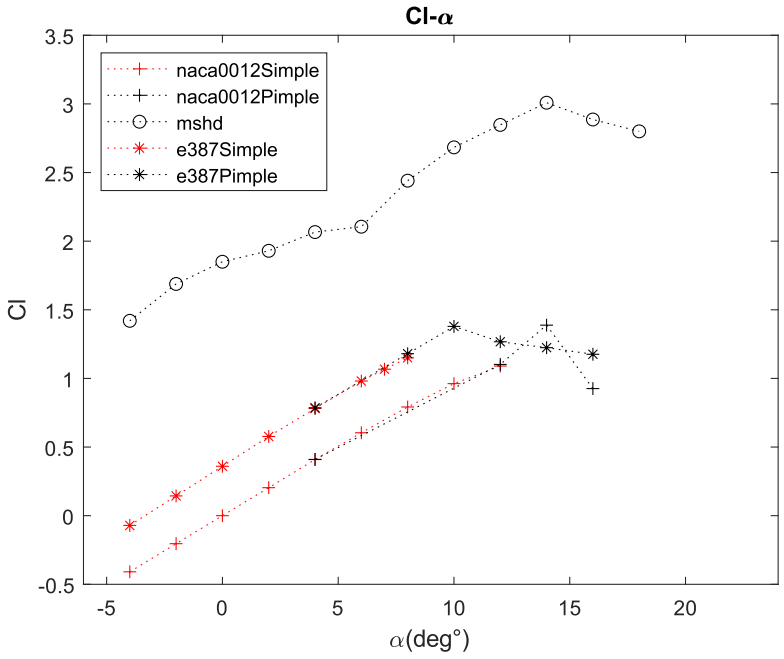

Figure 4.15: airfoils performance comparison

Pressure distribution

Another remarkable result is the following. In the figure we find plotted the pressure distributions of the three different profiles always at Reynolds 300000 at an angle of attack of 7 degrees. The Naca 0012 presents a distribution where the peak of depression is concentrated at the leading edge while later collapses rapidly. The E387 seems to have a less sharp pressure distribution in fact we also find in the rear portion of the profile a portion where depression contributes in the generation of lift. However, the mshd profile presents a pressure distribution quite different from the other two favoring 'aft loading', in fact we notice how the peak of depression at the leading edge is given up in order to obtain a flatter Cp curve that guarantees depression even closer to the tail of the profile.

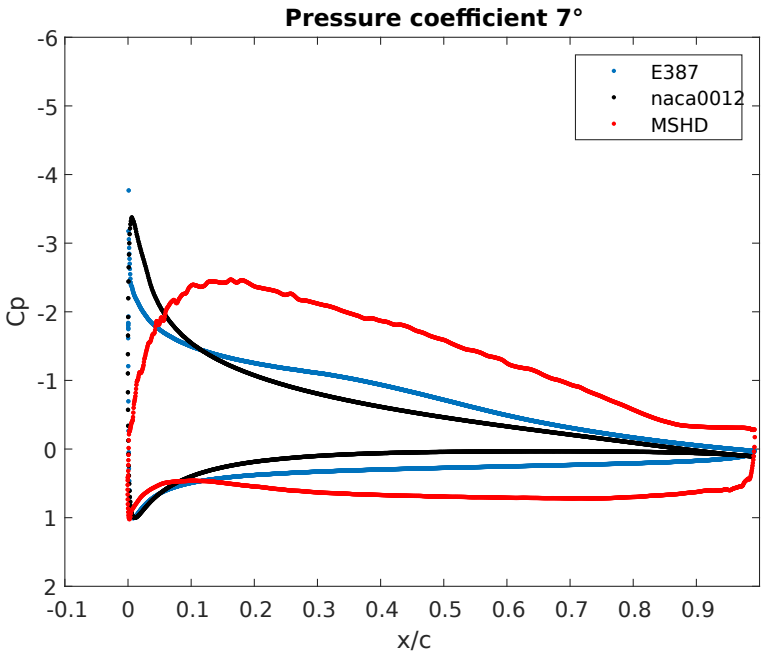

Figure 4.16: Pressure coefficient comparison between tested airfoils

Reynolds dependence

Another target we discussed in the introductory section concerns the relative insensitivity of the profile to changing its performance as speed and Reynolds number change. This almost constant behavior in different situations of the motion field would bring great benefits in terms of vehicle stability and dynamics. In fact as we will see in the next chapter by moving to a three-dimensional momentum field we already imagine that lift and drag will change dramatically with the square of the velocity, so in this scenario it would be a great benefit if these changes did not also depend on the shape of the profile. From the following image we can see that by doubling the velocity at the same AoA=7deg, and consequently the Reynolds number by going to a value of 600000, the Cp distribution of the MSHD is practically coincident with the case at Re=300000 while for the other two profiles a small variation can be found. Usually, the sensitivity from the Reynolds number can be mitigated by extending the range of the turbulent boundary layer [12]. In fact, this ensures an increase in the adverse pressure gradient that causes an instability in the motion of the separation point that causes a change in the initial conditions of the pressure recovery and results in turbulent instational separation.

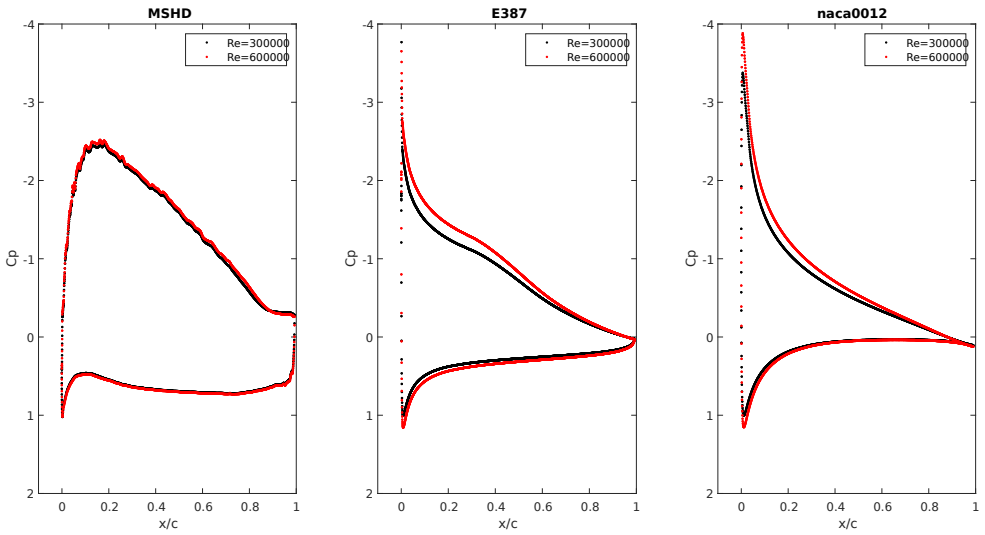

Figure 4.17: Reynolds dependence on pressure distribution on tested airfoils

5 | Winglet design

The purpose of this chapter is to analyze, from an aerodynamic point of view, analogies and differences between the 2d case and a finite wing clamped to a wall that would approximate motorcycle fairings, proceeding than with a sensitivity study and with a design proposal. In particular we focused on a wing in which the semi-span length is equal to the chord.
In order to keep the same nomenclature used in aeronautical field we defined this geometry of wing having an aspect-ratio equal to 2. Referring to figure 5.1 we defined

$$AR = \frac{2s}{c} = \frac{b}{c} \tag{5.1}$$

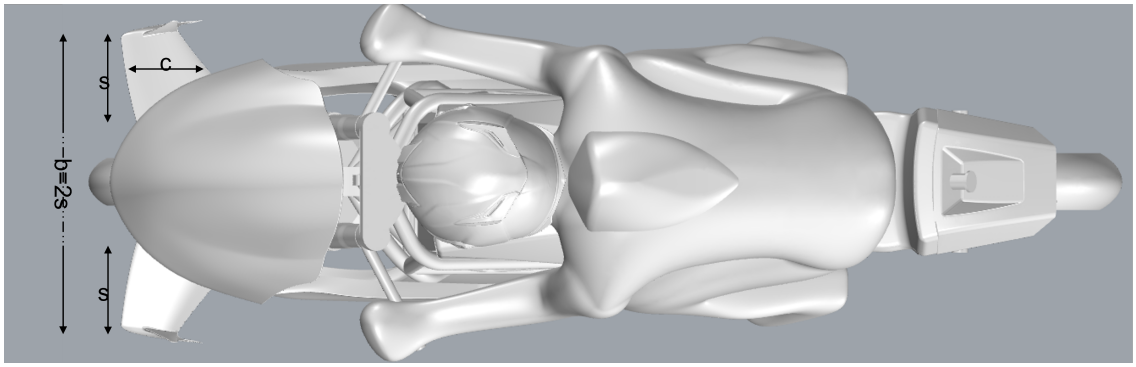

Figure 5.1: Motorcycle upper view

5.1. Problem geometry and setup

In this chapter we adopted an aeronautical approach in which we consider winglet oriented such that vertical force ar directed upward and so we will talk about lift more that downforce.
In this case we used two different, but very similar, setup: the first one to validate the model, the second one to analyze the effects of main wing geometry parameter. Both setups use a box domain in which the wing is attached to the back wall as in figure 5.2a

and 5.2b

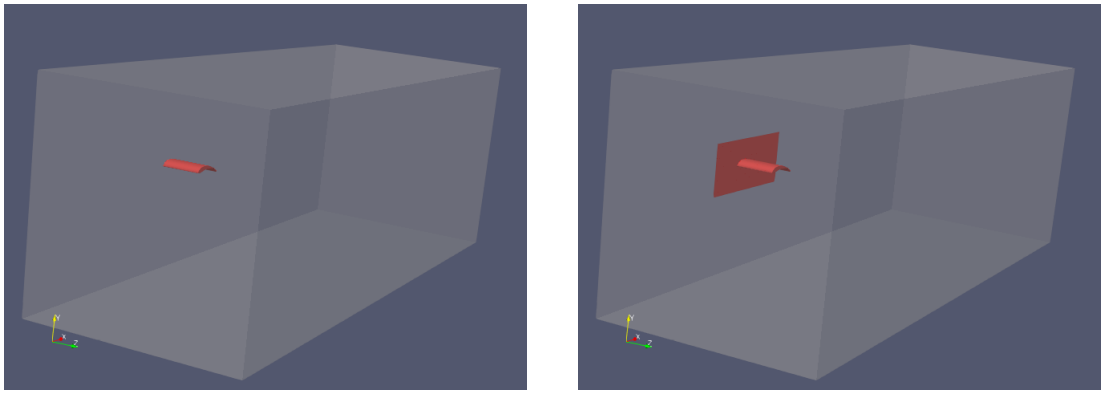

(a) Validation Geometry (b) Analysis geometry

Figure 5.2: Geometry of the numerical simulations for finite wings

We can notice in figure 5.2b that a physical wall has been added at the root of the wing in order to approximate the lateral fairing of the motorbike. Dimensions of the wall are reported in next figure: (5.3)

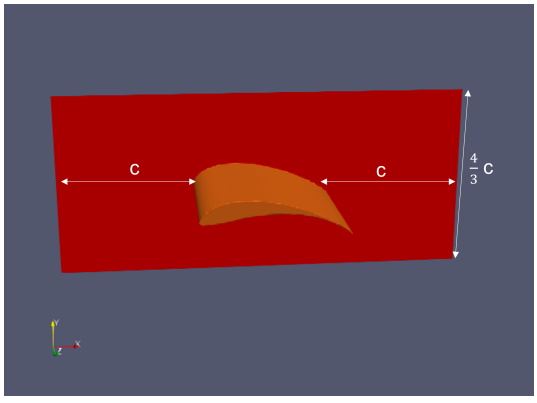

Figure 5.3: Detail of geometry for finite wings

About the same setup of the 2d case in section 4.1 have been applied here bor both validation and analysis case in order to obtain a comparative as reliable as possible. Chord and velocity remains respectively 0.15m and 30m/s, so the Reynolds number remains unchanged. Same consideration about the domain of interest of the 2d case was done for this case, extending the domain enough in the third direction, in order to leave the tip vortex freely develops. In order to contains the computational costs domain has been shrunk a bit, while ensuring there is no interference with the boundary condition imposed. Regarding the boundary conditions we find:

- INLET: 'FixedValue' conditions for the speed, set at 30m / s and 'ZeroGradient' for the Pressure.
- OUTLET: 'FixedValue' with null value for the Pressure, and 'ZeroGradient' for the speed.
- UP / DOWN: 'Symmetry' type condition for both pressure and speed.
- FRONT: 'Symmetry' type condition for both pressure and speed.
- BACK: 'Symmetry' type condition for both pressure and speed in the validation case, so that it is possible to run just half of the geometry. In the other case, in which we add the wall we set 'Slip' type condition for the velocity and 'ZeroGradient' for the pressure. Then, to add the boundary layer in the region of the root 'NoSlip' condition was added to the physical wall of figure 5.2b
- AIRFOIL: 'NoSlip' for speed and 'ZeroGradient' for Pressure.

5.2. Mesh description and grid convergence

For this 3d study we used SnappyHexMesh as software to build the mesh. SnappyHexMesh is the mesher implemented in OpenFOAM^{TM}.
The meshes created presents a quite coarse background mesh with surfaces refinements on the airfoil and on the wall, if present. Furthermore a refinement box has been imposed all around the airfoil, especially in the backward in order to better capture the wake. It extends in the span direction for two times the span length and in the flow direction about seven times the chord length. About five layers was added in order to better capture the boundary layer as in figure 5.4b

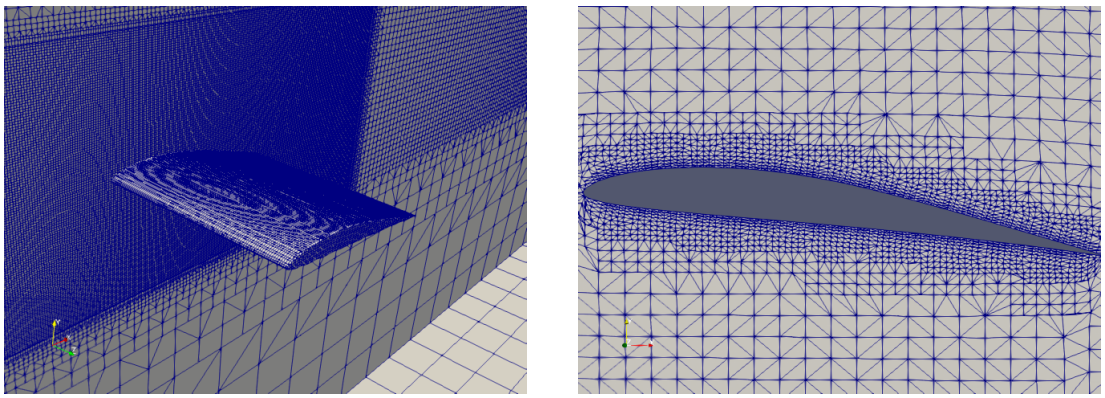

(a) 3d wing mesh (b) 3d wing layers mesh

Figure 5.4: Mesh for 3d wing attached to the wall

A grid convergence study, as in section 4.3 was done also for this case.

	N° Of Elements	Y+ Min	Y+ Max	Y+ Avg	Cl	Cd
Mesh1	330659	3.6	118.9	32.4	0.328	0.041
Mesh2	478178	3.1	88.4	27.8	0.307	0.04
Mesh3	647898	3.4	94.7	25.7	0.323	0.036
Mesh4	1113394	2.1	78.1	20.2	0.327	0.036
Mesh5	3471836	0.21	51	13.8	0.329	0.034

5.3. Turbulence model and numerical schemes

SIMPLE algorithm was used to solve pre-stall AoA analysis and PISO algorithm to solve for unsteady flow.

SIMPLE setup is similar to the 2d case with an important difference in the boundary layer treatment. As opposed to the 2d case in which we solved for the boundary layer thanks to a very fine mesh that take y^+ to be about 1, in this case, computational costs led us to use wall function treatment, in order to could get a restrained number of mesh elements.

Regarding the setup for PISO solver, first of all we set the time-step duration such that Courant Friedrichs Lewy was respected, obtaining a CFL number slightly less to one. For more accurate indication on numerical schemes we remind to section 4.4

5.4. Model validation

In order to validate the model we proceed with two steps:

- a comparison between our results and the ones from non-linear lifting line theory
- a comparison between the 2d pressure coefficient and the pressure coefficient of a section in the middle of a AR 20 wing, in which we can neglect the tip effects

Lifting-line theory comparison

Non linear lifting line theory (LLT) prediction was obtained through XFLR5, a open-source software for 3D wing analysis, that make use of Xfoil to obtain a 2d prediction of the section that, in a second step, is used in LLT calculation. For the LLT case, the viscous analysis is fully coupled, and it iterates both 2D viscous and 3D solutions until convergence is met. We take as reference the E387 airfoil and we simulate, both with XFLR5 both with OpenFOAM^{TM} wings with different aspect ratio, keeping the chord constant and increasing the span. All simulation was done at an angle of attack equal to 7° using a simple rectangular planform as shown in next figure.

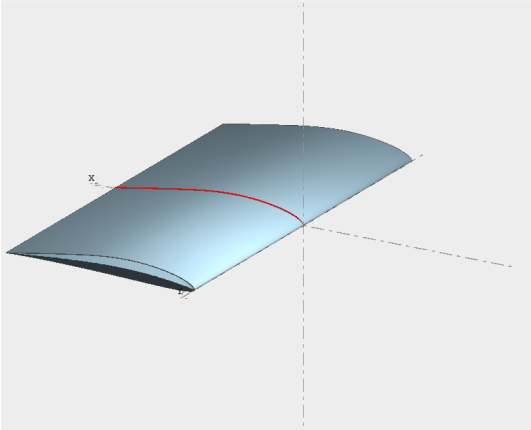

Figure 5.5: Wing planform for validation

A comparison for lift and drag was done varying the aspect ratio. In the following graphs are reported, respectively, the lift and drag comparison between the LLT prediction and the cfd simulation results both for the wing clamped to the wall, both for the wing flying suspended without the wall. For completeness also 2d results are shown.

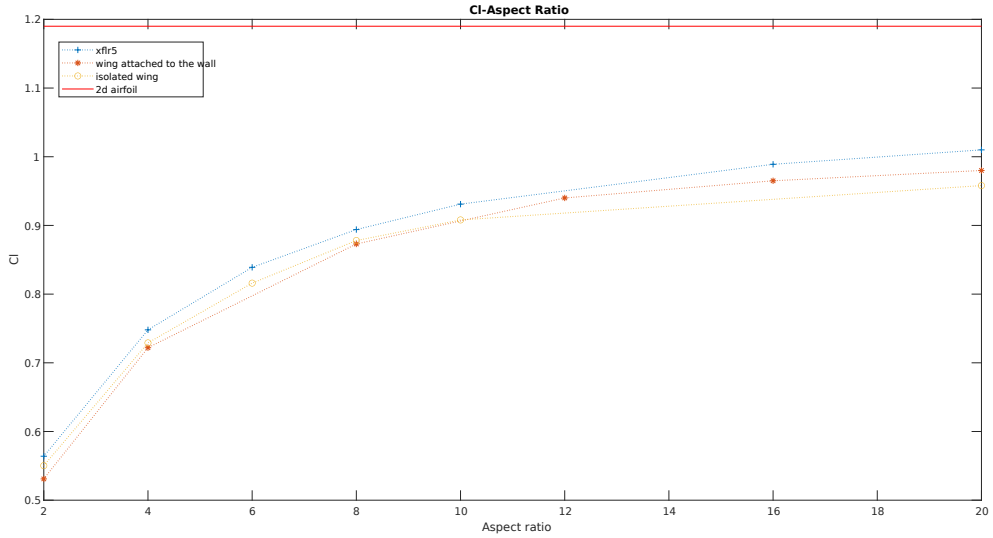

Figure 5.6: LLT-cfd comparison, Cl as function of AR

We can notice a good agreement of the results, except for very low aspect ratio, where limitation of LLT becomes important and XFLR5 simulation can't met convergence. Moreover, is clear that increasing the aspect ratio, the lift coefficient tends to the 2d one. Regarding the drag coefficient, as expected, a quite large discrepancy of the results is observed. However, although the numerical value is not captured correctly, the trends of reducing the drag increasing the aspect ratio is correctly captured.

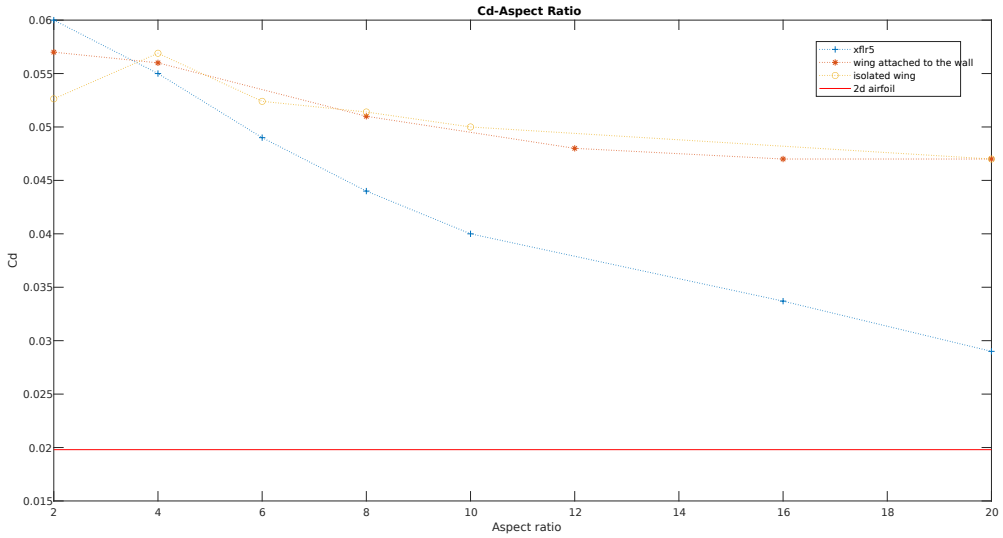

Figure 5.7: LLT-cfd comparison, Cd as function of AR

2d comparison

Another approach for the validation was followed in order to obtain a comparison not only on the integral quantities, such as total lift and drag coefficient, but a local analysis through the comparison of the Cp. In particular we compared the Cp of the 2d airfoil, previously checked with the experimental data, with the Cp of the central section of an AR 20 wing, in which tip effects could be considered negligible. In figure 5.8 is shown this comparison:

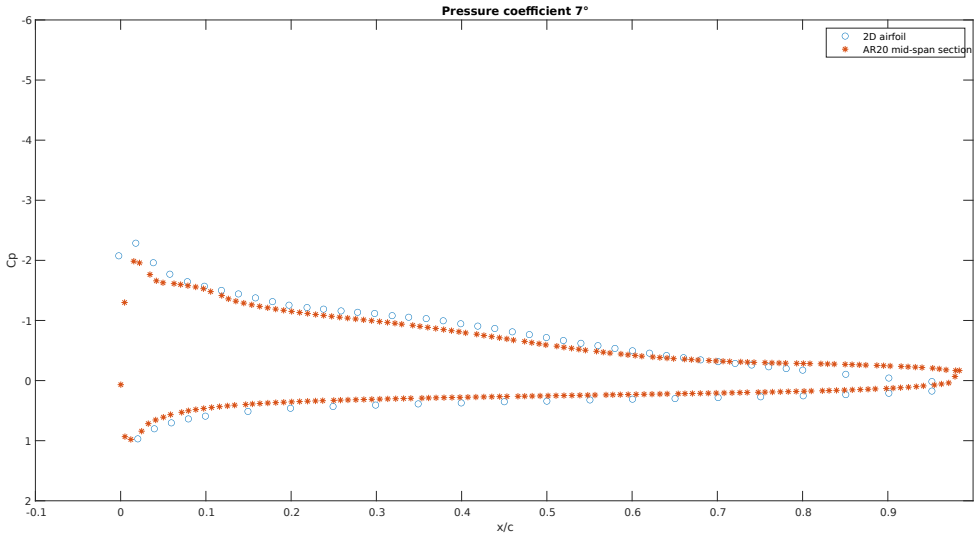

Figure 5.8: Cp comparison between 2d case and middle section of AR20 wing

Also in this case the results are satisfactory and we can conclude saying that we can correctly capture the pressure distribution, instead for the drag we can just use our simulation as comparison between two different geometry, if the really same simulation setup is used, but we can not predict the correct value of the drag. However we do not retain that discrepancy as a serious sources of errors because if we compare the total drag force of the wings, that have a small Cd and quite small area, with the total drag of the motorbike that presents a larger area and an higher drag coefficient, typical of bluff body, the error committed would not be so relevant.

5.5. Results

In this chapter we will describe the results obtained analyzing the wing changing some main geometry parameters. A work of search for an improvement was done on the wing attached to the wall.

Main parameter analyzed are: the airfoil, the taper ratio, the sweep angle and different tip device solutions.

5.5.1. Airfoil influence and main wing characteristics

First parameter analyzed is the 2d airfoil. The purpose of this part of the work is to understand the influence on a AR 2 wing of the chosen airfoils, with particular attention to maximum lift coefficient. The first question we asked ourselves was if a 2d airfoil with a higher lift coefficient leads to a three dimensional wing with higher lift coefficient also with a low aspect ratio wing. For this purpose we design three basic wings with the following characteristics:

- chord = 15cm (as in the 2d case)
- rectangular planform
- Aspect Ratio 2
- the airfoils used was that described in chapter 4

A comparison between the 2d and 3d Cl-α curve for the three selected airfoil is reported in next figure.

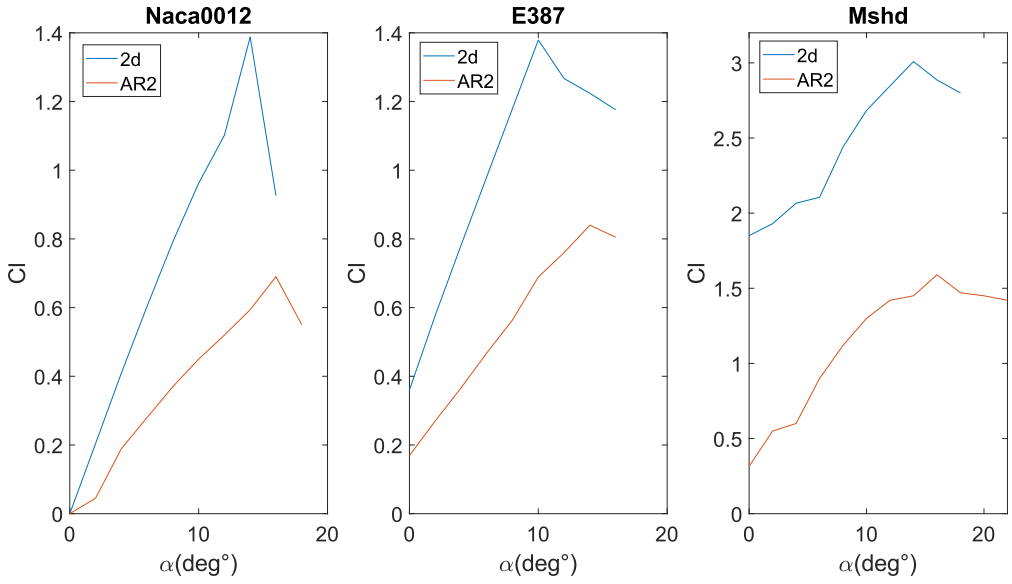

Figure 5.9: Cl-α comparison between AR2 wings and 2d case for different airfoil section

We can notice, for all three airfoils, a maximum lift reduction with an increase of maximum

angle of attack and a reduction in the slope of the curve both in the increasing region, both in decreasing region, after the maximum lift angle of attack. However it is clear that 3d wings keep about the same gap of performance, in terms of maximum lift, of the 2d case. It is reported for clearance, in next figure, a comparison between the three Cl$-\alpha$ of the 3d wings.

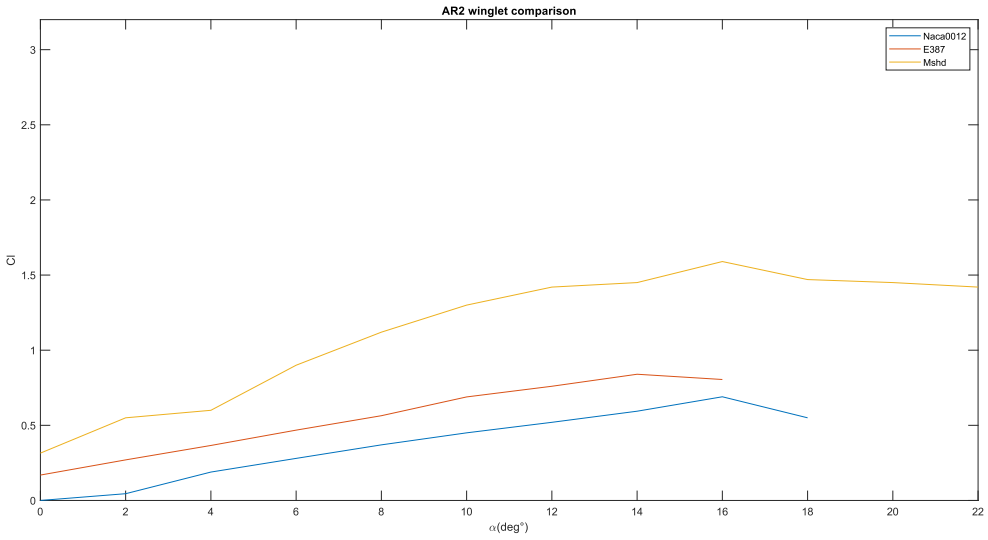

Figure 5.10: Cl-α comparison for different AR2, rectangular wings with different airfoil section

The mshd wing still have the maximum lift coefficient compared with the other two wings. Despite the flow is highly three dimensional and the presence of the tip vortex strongly modify, as we will see later, flow characteristics around the wing and in the wake, 2d section has a great influence on the wing performance.
Moreover, we compared the slope of the E387 wing with the theoretical prediction proposed by Lowry and Polhamus and by Hoerner and Borst [18]. Results of this comparison are reported in figure 5.11.

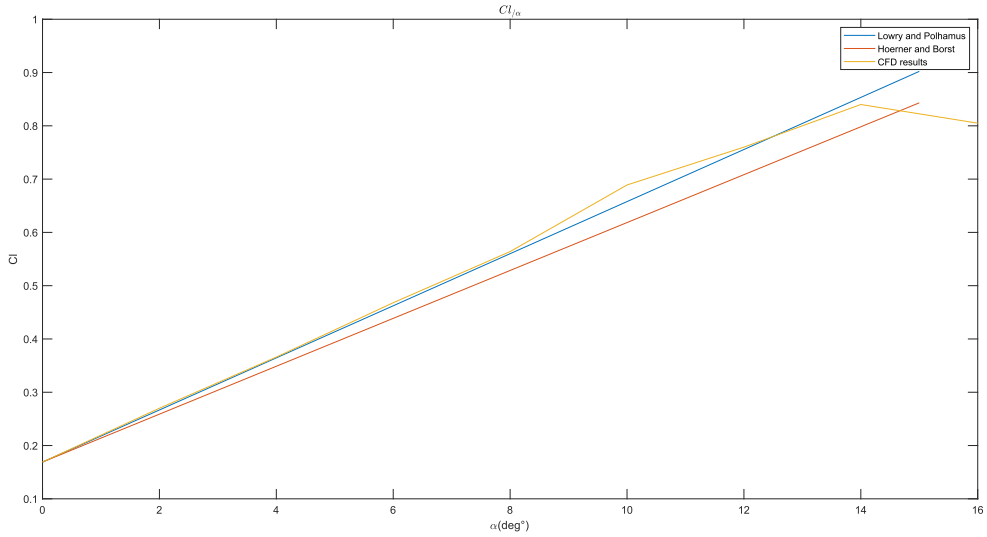

Figure 5.11: Cfd and theoretical Cl/α comparison for AR2 wing with E387 airfoil section

We can notice a very good match of our results with the Lowry and Polhamus prediction a part for a little non linearity present at high angle of attack, accordingly with Torres and Mueller [34], probably due to the tip vortex. A more detailed analysis on pressure distribution and lift distribution is now presented. We focused only on high angles of attack, that are of major interest for our case, in order to obtain the maximum lift. Particular attention was given to the maximum lift angle of attack and the the one immediately subsequent, assuming that a possible solution is to install the wing on motorbike so that, during a braking, thanks to the pitch angle of the motorbike, the wings take the angle of attack immediately subsequent to the maximum lift one. In this way, although a little reduction of downforce would be experienced, the near stall condition would increase significantly the drag force, increasing braking capability. We will talk about it more in detail in next chapter. Lift distribution was calculated at different angle of attack for all three wings.

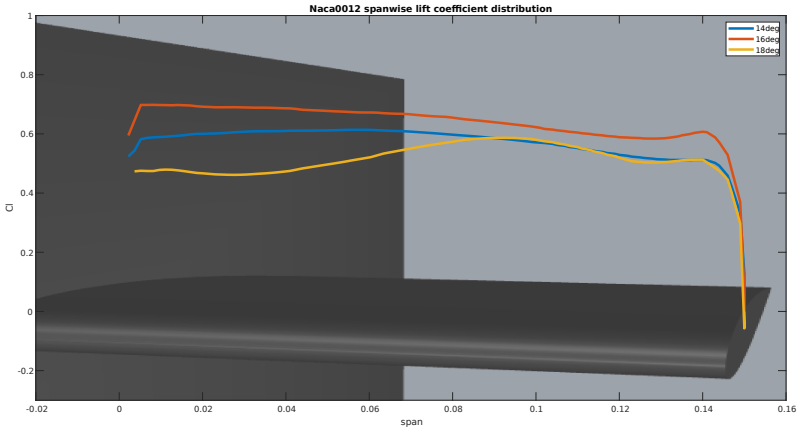

Figure 5.12: Naca0012 AR2 wing Cl distribution

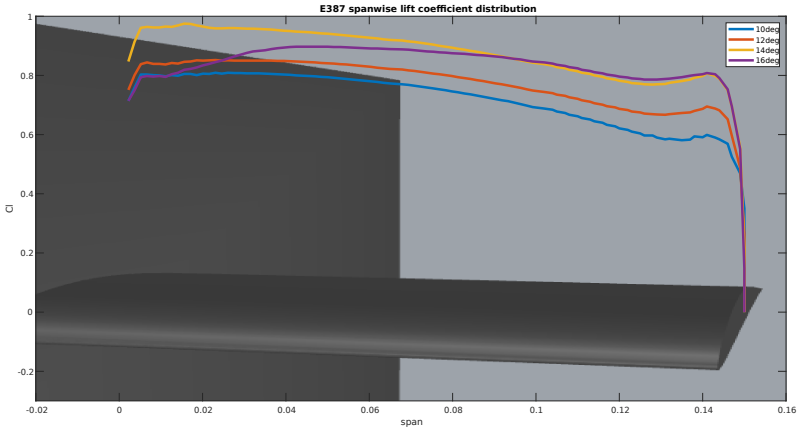

Figure 5.13: E387 AR2 wing Cl distribution

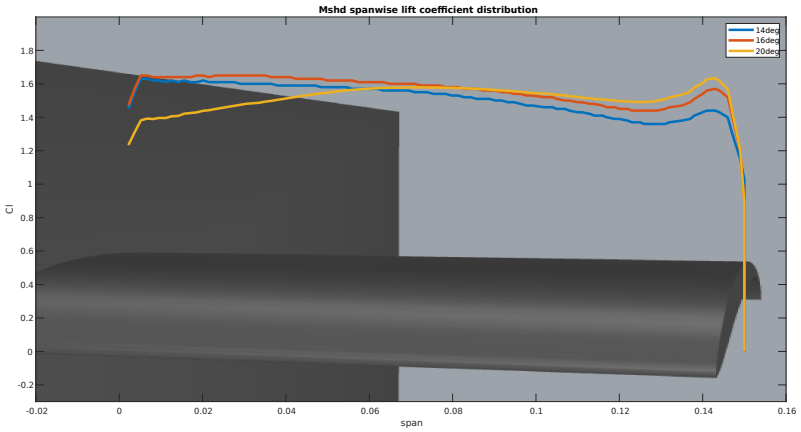

Figure 5.14: Mshd AR2 wing Cl distribution

Regarding the lift distribution we can notice a trend similar to the one obtained by Sathaye et al. [24] with a lift peak at the tip of the wing. It is possible to see that the peak at the tip is more evident increasing the angle of attack and it grows passing from the less performing airfoil to the more performing one, where the maximum lift is higher. We can conclude saying that the lift increase on the tip of the wing, due to the tip vortex, is more relevant when an higher Cl condition is lead. In fact, increasing the Cl, increases the pressure difference between the suction side and the pressure side, making the vortex stronger.
It is also interesting to have a look at post stall angle Cl distribution. It is clear that the stall starts at the root of the wing and affect about the first half of the wing, whereas the tip region presents a further increase of the lift coefficient. This is somehow in agreement with the results of Torres and Mueller of figure 1.22 in which we can see that the wing with an $AR \leq 1$ is capable to reach higher angle of attack and higher lift coefficient. Confirming this, we report in next figure the pressure contours on the E387 wing at 14° and 16° and on the MSHD wing at 16° and 18°.

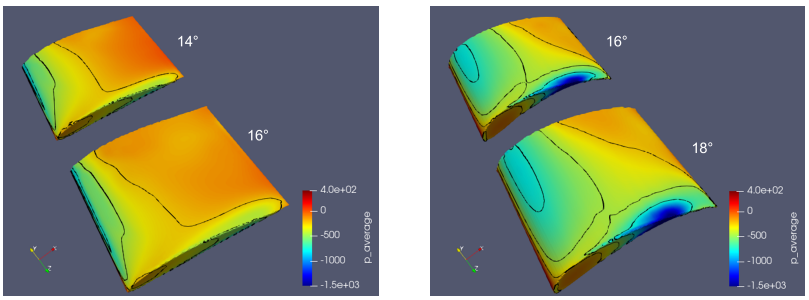

(a) E387 pressure contours (b) MSHD pressure contours

Figure 5.15: Pressure contours on different AR2 wings at different AoA

Pressure contours confirm the presence of a suction peak on the tip. Moreover it is possible to see that, specially in the MSHD wing, the tip vortex affect the pressure distribution of all the wing but with major influence in the tip region. For better understanding in next figure is reported for the MSHD at 14° AoA a pressure contours of the wake and the streamlines near the wing.

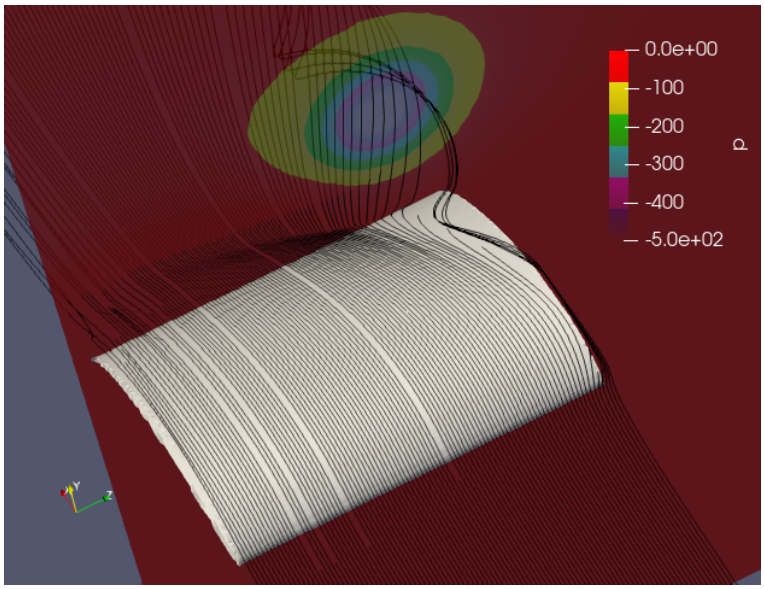

Figure 5.16: MSHD wing wake pressure contours and streamlines

We can say that the vortex core is a very low pressure region capable of drawing in the airflow, as we can notice looking at the streamlines. This low pressure region generated by the vortex reduces the adverse pressure gradient on the rear part of the wing avoiding the circulation zone which is generated on stalled airfoil. In next figure we report the planar velocity vector for both a section at 0.1b and 0.9b. In particular in the two following slice vectors are oriented as follows

$$\vec{v} = v_x \cdot i + v_y \cdot j \tag{5.2}$$

and colored by the module of $\vec{v}$

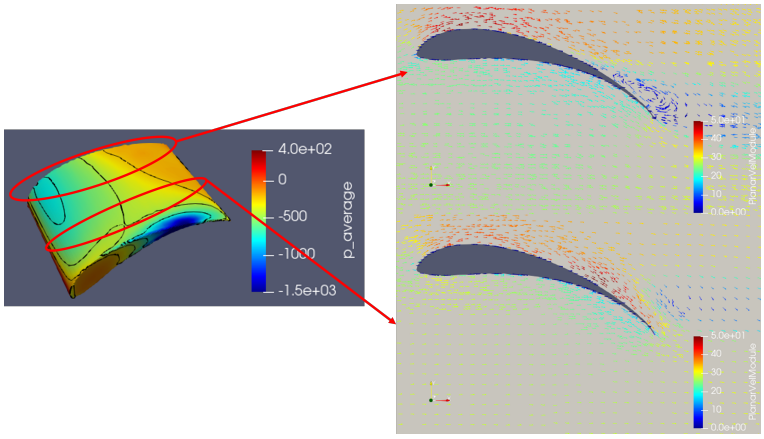

Figure 5.17: Planar velocity vector on a plane near the root and near the tip for MSHD AR2 wing

The root region of the wing already presents a separation zone at the maximum lift AoA, while the flow on the tip region is still attached. This suggests the presence of an induced AoA. Some consideration about that will be done later in this section but it is possible to anticipate that the absence of a rear recirculation zone is due primarily to the low pressure region of the vortex rather than the induced AoA
The flow is strongly three-dimensional as shown in figure 5.18 in which streamlines on the MSHD wing at 14° AoA are reported. We can appreciate that the vortex does not develop immediately on the leading edge but after a fraction of the chord, in fact, we can see that all the streamlines that arrives more or less only in x direction, are than affected by the tip vortex that induce a z-direction component of the velocity.

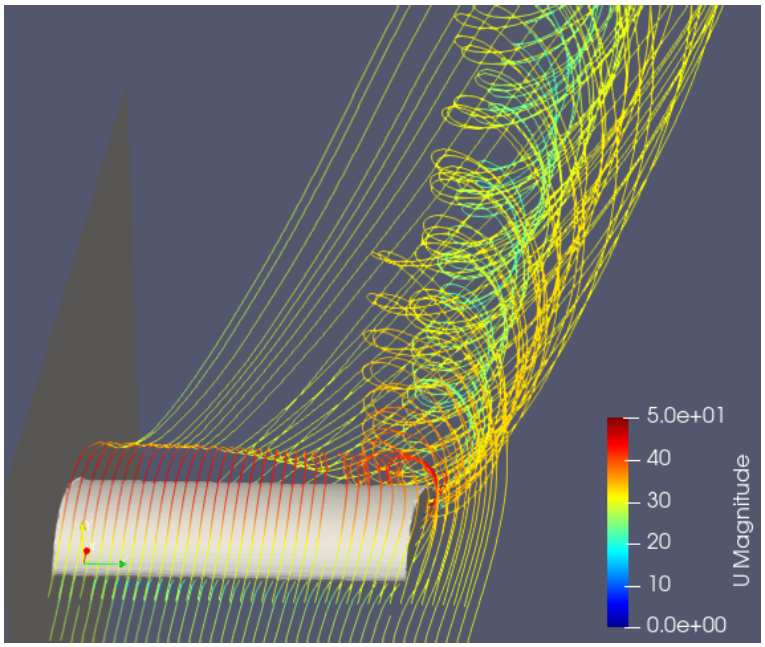

Figure 5.18: Streamlines on MSHD wing at 14° AoA

More accurate considerations on the induced velocity can be done referring to figure 5.19 in which planar velocity vectors are reported. Vectors are oriented as follows

$$\vec{v} = v_x \cdot i + v_z \cdot j \tag{5.3}$$

and coloured respectively by:

- the module of $\vec{v}$
- v_y
- v_z

and the plane section is located at $0.9c$ from leading edge.

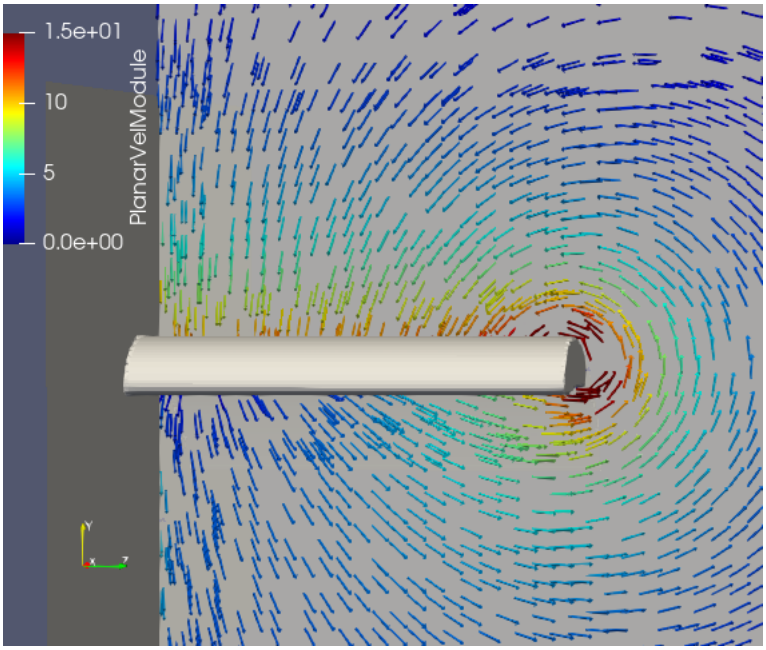

(a) $|v_y \cdot i + v_z \cdot j|$

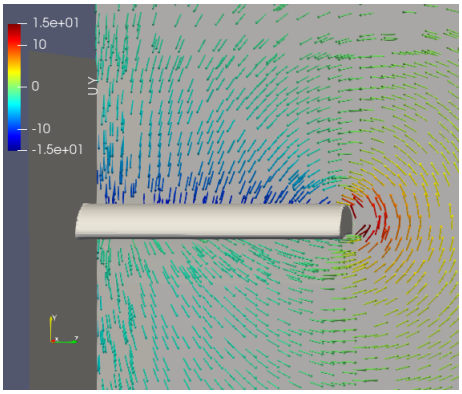

(b) v_y

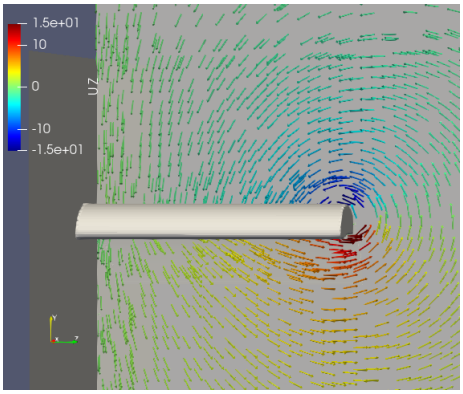

(c) v_z

Figure 5.19: Velocity vectors on x-normal plane for MSHD wing

From figure 5.20a it is possible to see the flow going from the pressure side towards the suction side of the wing. From figure 5.20b we can clearly see a non-negligible component of the vertical velocity going upward in the region just after the tip, instead in the region above the wing the y-velocity seems to be quite constant, making us think that the induced AoA would not be so relevant. Further consideration will be done later. From figure 5.19c we can see an opposite trend between the region above and under the wing with a positive z-components of the velocity under the wing and a negative z-components of the velocity above. Regarding the induced AoA, it is difficult to estimate its magnitude because:

- vortex starts to develop at about 1/3 of the chord and becomes stronger moving to the trailing edge. Its influence on the y-components of the velocity therefore is not constant moving from the leading edge to the trailing edge.
- downwash due to the vortex is overlapping to the downwas of the profile that, also in 2d case is present.
- vortex influence is present, although to a lesser extent, also at the root of the wing so we don't have a reference against which we can base our calculation of the induced AoA

In order to get an idea of the magnitude of the induced AoA we can however have a look for the MSHD wing at 14° AoA to the z-distribution of the downwash angle defined as

$$\arctan \frac{v_y}{v_x} \tag{5.4}$$

Below are reported downwash distribution at $0.5c$ and $0.9c$

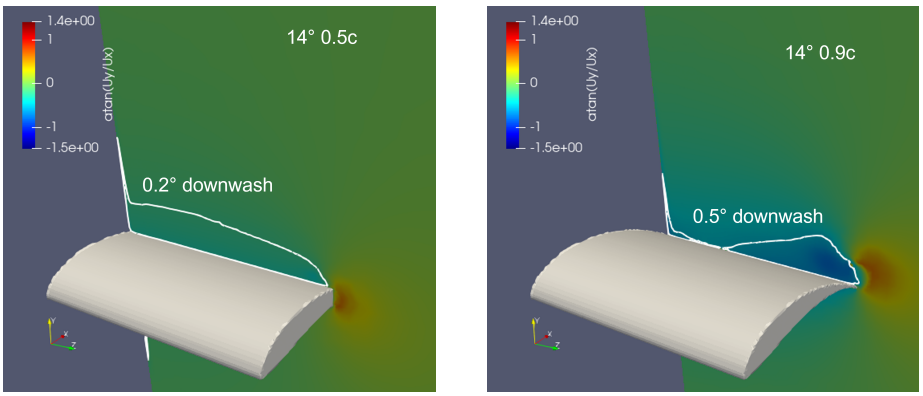

(a) $0.5c$ (b) $0.9c$

Figure 5.20: Downwash distribution on MSHD wing at 14° AoA

In order to have a more quantitative representation, we added on the plane an two isolines that separate the zone in which the downwash angle is greater (near the wing) or smaller (far from the wing) of a target value. This target value changes between the two section plane because, obviously, the downwash angle increases moving to the trailing edge so we have choosen a higher value for the $0.9c$ section plane. We can see that at midchord downwash angle is about constant along the span and the value is still small. Moving to the other section analyzed we can see just a little higher value that disappear at about mid-span. We can conclude saying that the induced angle is not so relevant and the stall trend of figure 5.17 is due in a small way by this induced angle present in the

region closest to the trailing edge and for the most part by the votex low pressure. One last interesting result is about pressure on the lower surface of the wing. Also in this case we focused on the MSHD wing at 14° AoA.

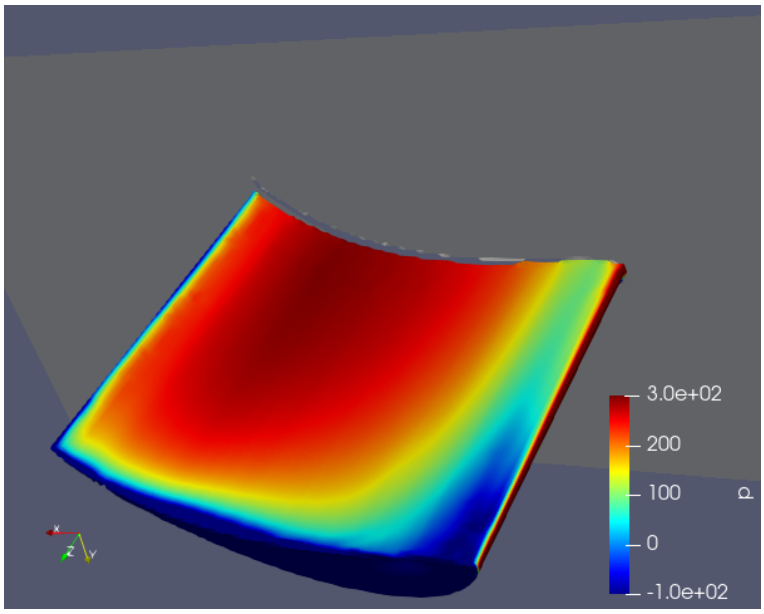

Figure 5.21: Lower side pressure on MSHD wing at 14° AoA

We can see a decrease of pressure moving from the root to tip with a considerable loss of lift in the very last part of the span. This low-pressure region is due to the airflow moving from the pressure region to the suction region. Although this lift loss is fully compensated by the low pressure region that the vortex generates on the upper surface, as in figures **??**, **??** and **??**, we found it interesting to analyse whether a simple endplate could reduce this air displacement and so this lift loss without losing the benefits on the upper surface. Furthermore some benefits in therms of induced drag reduction could be obtained. This study will be covered in the next section 5.5.2.

5.5.2. Simple endplates influence

At the end of previous section we explained, also thanks to the work by Viieru, Albertani et alter [37], reason why a simple endplates may be of interest, remembering, however that at high AoA the endplates could become uneffective or even counterproductive.
First enplate design derive from a "competitor analysis" in particular we referred to the 2016 Ducati Desmosedici, a race motorcycle for MotoGp competition.

Figure 5.22: 2016 Ducati Desmosedici

Solution developed by Ducati provides for the use of planar endplates that are simply an offset of the wing profile with a large round on trailing edge. In our case we tried to replicate this design focusing on the influence of those kind of endplates varying their dimensions. In particular we design 4 geometry with different offset dimension:

- 5mm offset that we will call EP5
- 10mm offset that we will call EP10
- 15mm offset that we will call EP15
- 20mm offset that we will call EP20

that are reported in order from the left to the right in next figure.

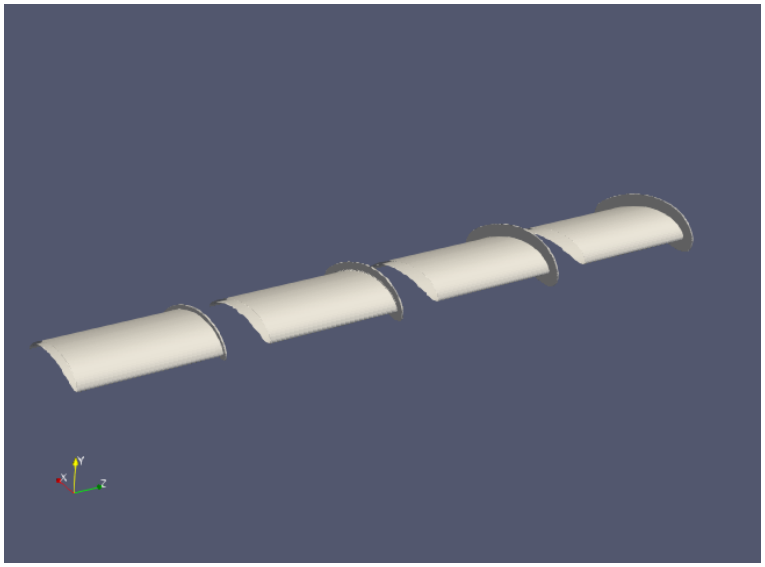

Figure 5.23: CAD design of simple different endplates

Airfoil chosen for this analysis is the MSHD because from previous studies seems to be most interesting between the three analyzed. We start to presents the results from the $Cl - \alpha$ and $Cl - Cd$ curve.

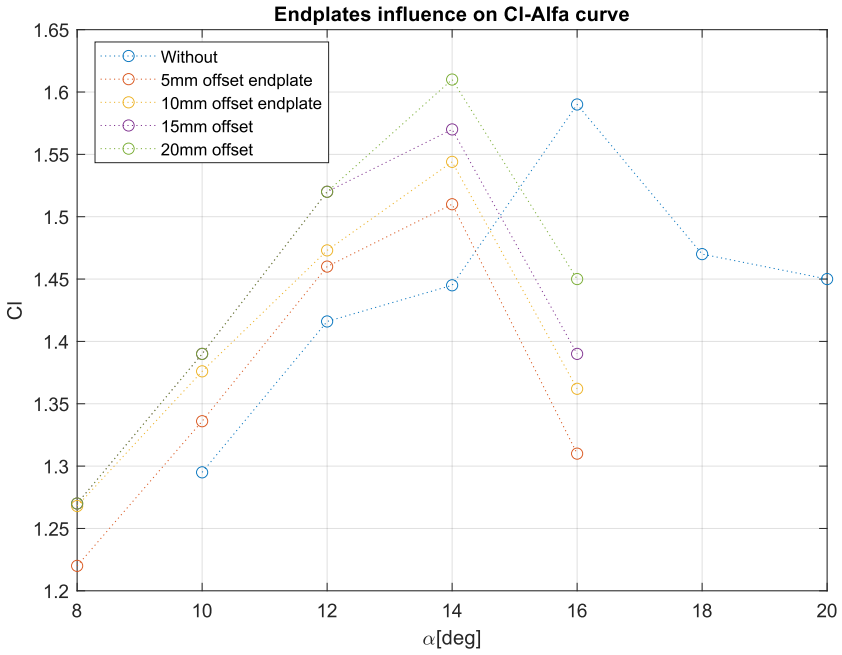

Figure 5.24: $Cl - \alpha$ for different endplates dimensions

It is clear that increasing endplate dimensions the $Cl - \alpha$ curve moves upward. However we can notice that the maximum lift AoA moves too, towards smaller angle. As a results maximum Cl obtained could be smaller or just a little higher than the one without endplate. In order to understand this lift increase, at equal AoA, we report the pressure distribution on the pressure side of the wings with:

- no endplates
- EP05
- EP10
- EP20

all at 14° AoA

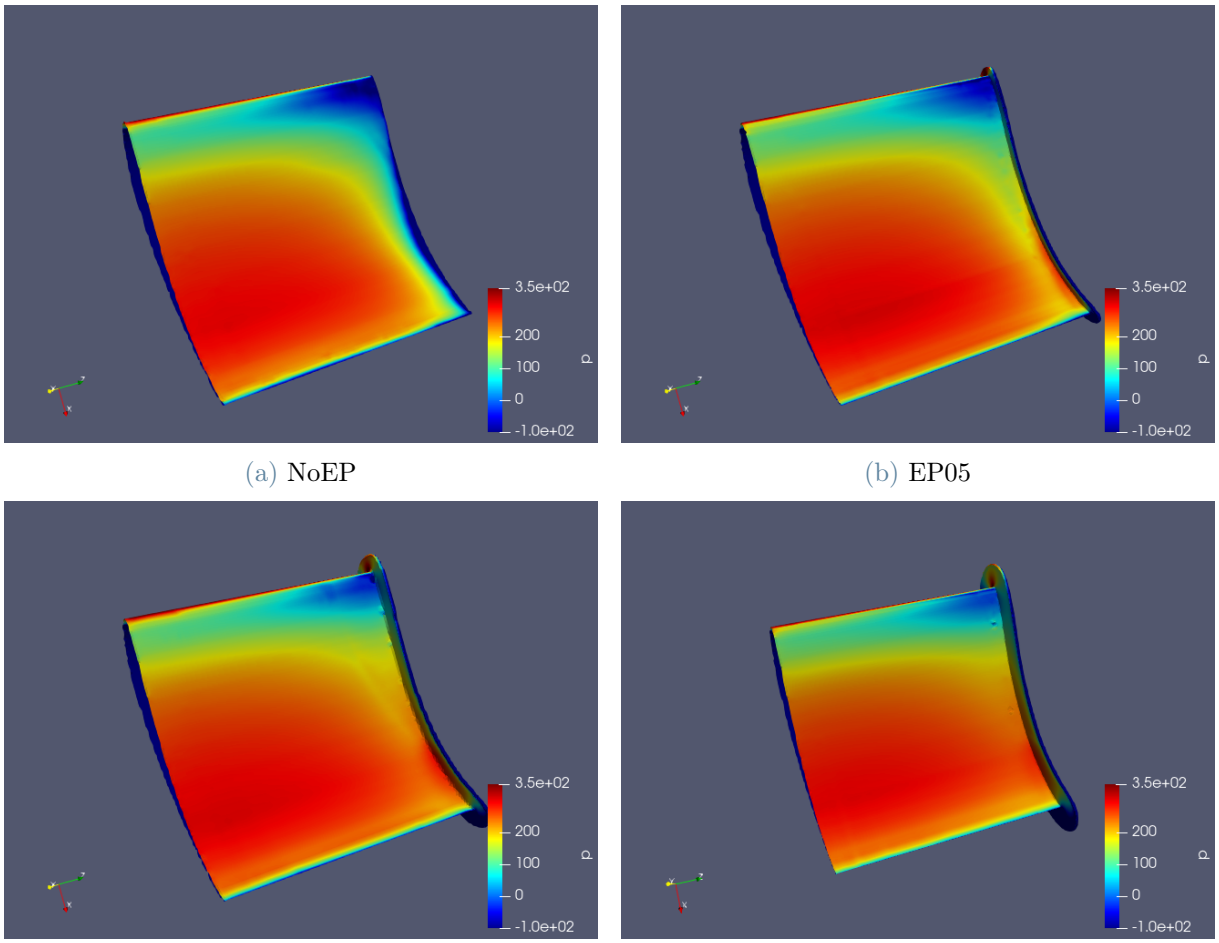

(a) NoEP (b) EP05

(c) EP10 (d) EP20

Figure 5.25: Lower side pressure distribution for various EP at 14° AoA

We can see that increasing the endplate dimension an higher pressure is reached on the lower side of the tip region. This effect is already visible for the 5mm endplate but becomes stronger when dimension is increased to 20mm.
Other considerations can be done looking instead at the pressure distribution on the upper side of the wing. We report in next figure the pressure distribution on suction side for the same case of figure 5.25.

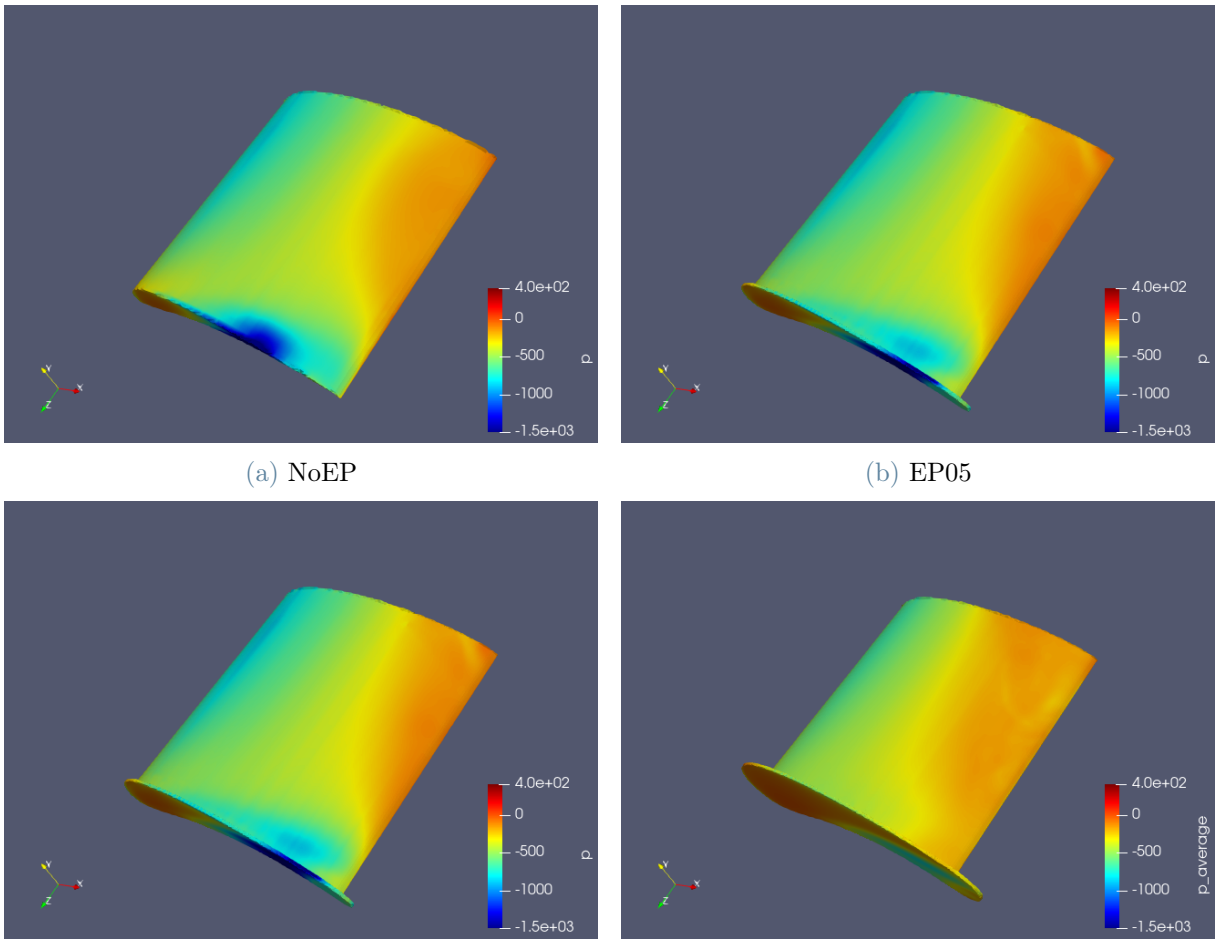

(a) NoEP (b) EP05

(c) EP10 (d) EP20

Figure 5.26: Suction side pressure distribution for various EP at 14° AoA

We can see a strong reduction of the low pressure region generated by the tip vortex. This reduction implies the anticipation of the stall because reducing low pressure region an higher adverse pressure gradient is reached with consequent flow separation.
In order to better understand flow structures and their variation with enplates dimensions we report also a streamlines comparison between the cases analyzed before in figure 5.25 and 5.27.

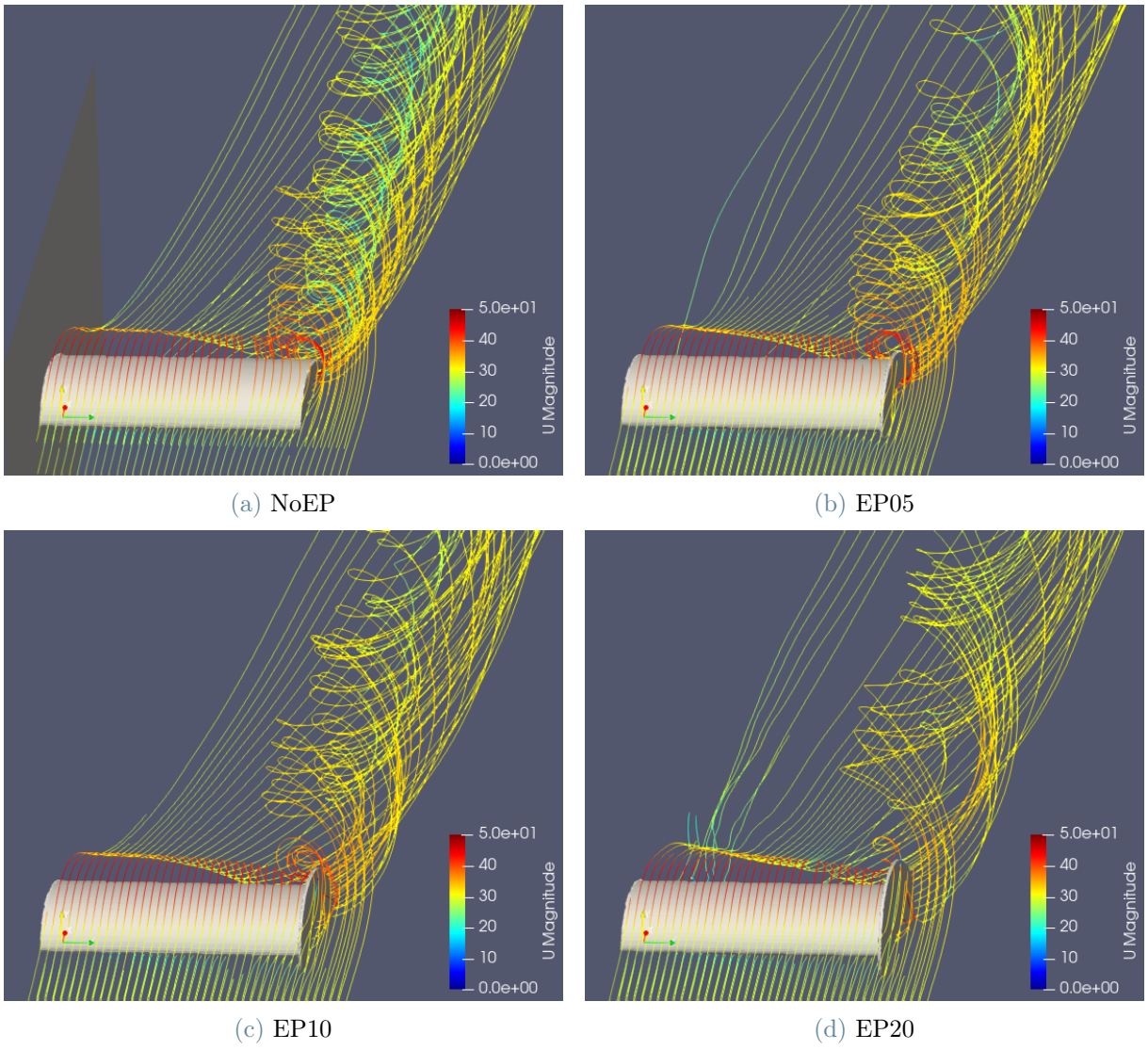

(a) NoEP (b) EP05

(c) EP10 (d) EP20

Figure 5.27: Streamlines for various EP at 14° AoA

We can see that increasing the endplate dimension vortex seems to be less structured but three-dimensional structure is still present and a substantial influence of this vortex is still present in the most part of the wing.
More quantitative visualization can be obtained representing planar velocity on the x-normal plane. In figure 5.28 and 5.29 vectors are oriented as follows:

$$\vec{v} = v_x \cdot i + v_z \cdot j \tag{5.5}$$

and coloured, in figure 5.28 by v_y, instead in figure 5.29 orientation remains the same but vectors are coloured by v_z.

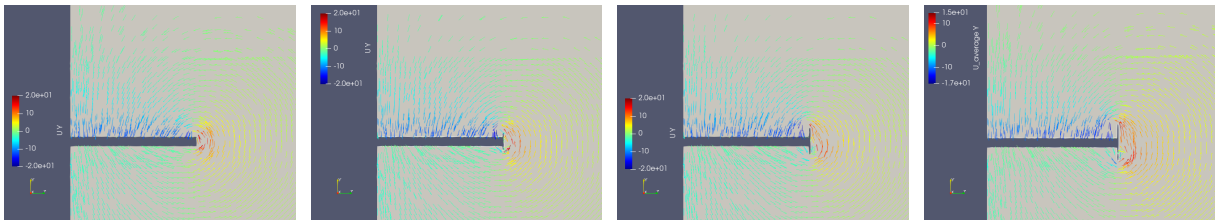

(a) NoEP (b) EP05 (c) EP10 (d) EP20

Figure 5.28: Planar velocity for various EP at 14° AoA coloured by y velocity

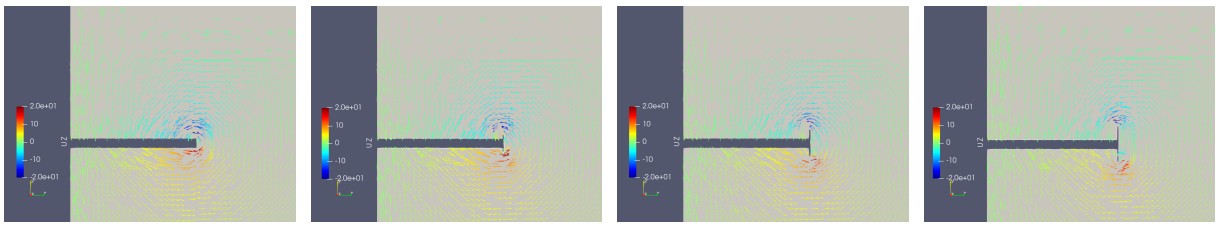

(a) NoEP (b) EP05 (c) EP10 (d) EP20

Figure 5.29: Planar velocity for various EP at 14° AoA coloured by z velocity

We can see that these simple endplates do not reduce vertical velocity at the tip but rather they increase it. Just a little reduction in z velocity is experienced. However they significantly change vortex shape making that elliptic. In order to better understand vortex shape modification, we present a comparison between the EP20 and NoEP wing x-vorticity at the trailing edge and along the wake. In next figure we report isolines of x-vorticity plotted on x-normal planes at various distance from the trailing edge.
In particular, distance from the leading edge is:

- 1c for the nearest plane
- 2c for the secon plane
- 4c for the third plane
- 6c for the last plane

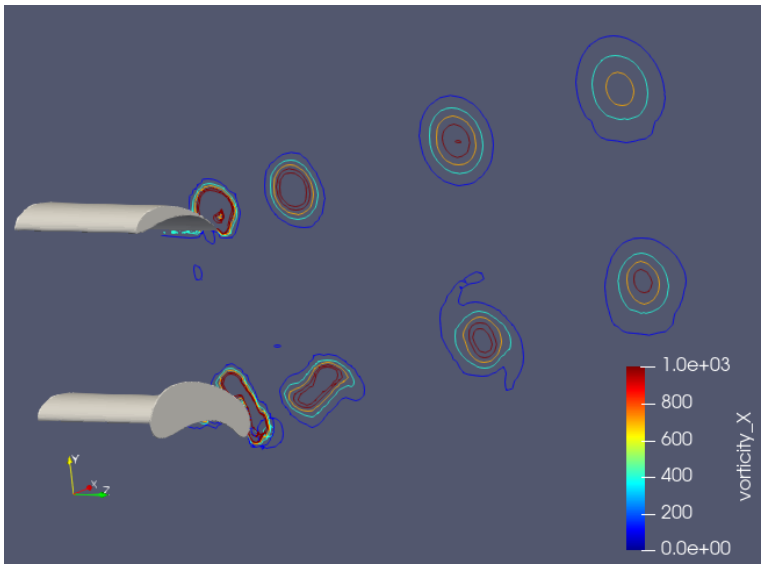

Figure 5.30: Vorticty isolines for NoEP and EP20 wing

We can see, as said before, an elliptic shape of the vortex on the airfoil that, moving away along the wake, again assumes a circular geometry. What we can see in next figure is the last plane isolines of figure 5.30.

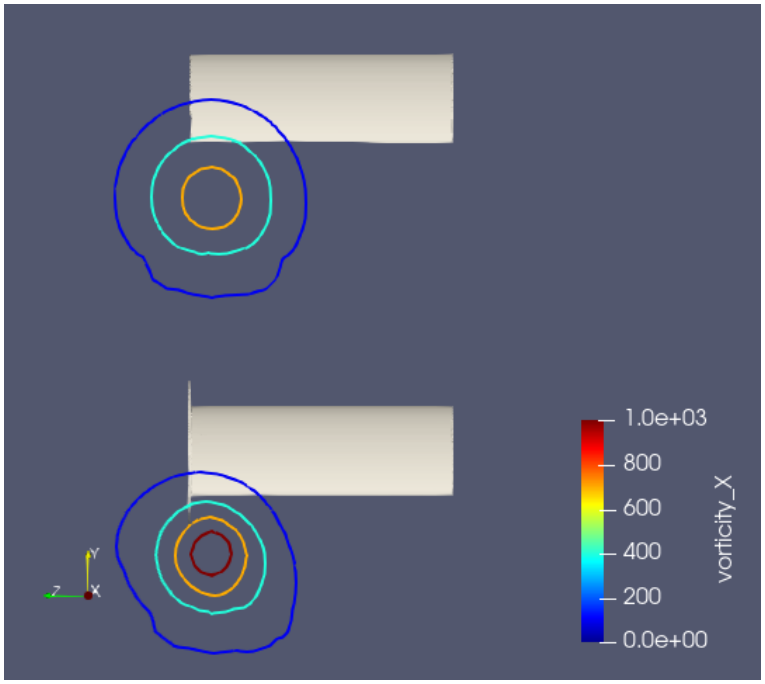

Figure 5.31: Vorticty isolines at 6c distance from leading edge for NoEP and EP20 wing

This visualization make us understand that in the far wake the effect of this kind of endplate is to increase the vorticity without significantly modify vortex dimension.

All the effects described so far result in a little reduction in drag that we summarise in the next figure.

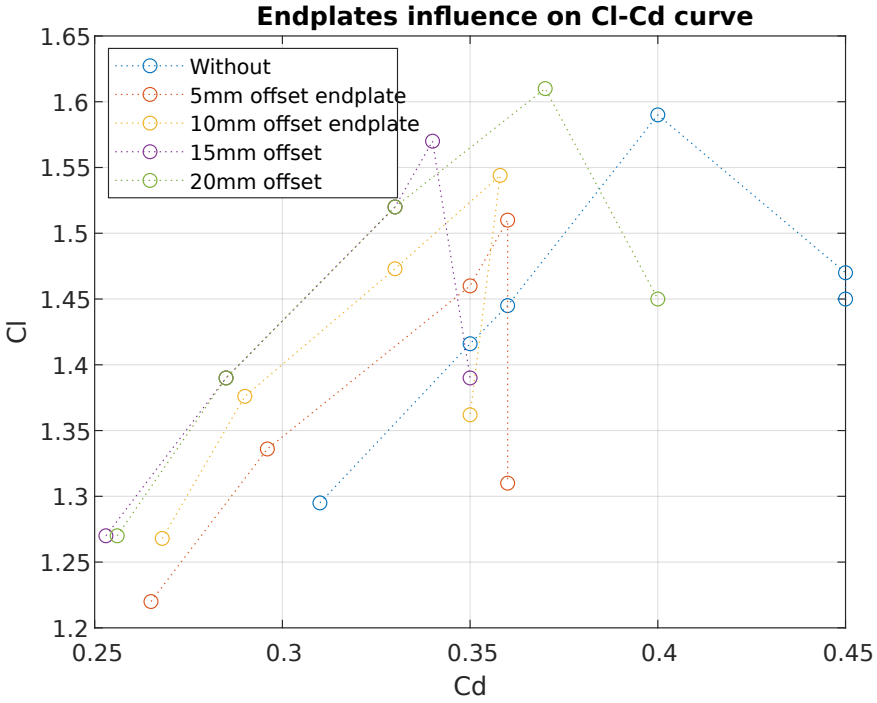

Figure 5.32: $Cl - \alpha$ for different endplates dimensions

5.5.3. Taper ratio influence

Another parameter that we know could be relevant in particular in terms of induced drag is the taper ratio. Following figure [30] represent the value of δ of equation A.16 as function of taper ratio for various AR.

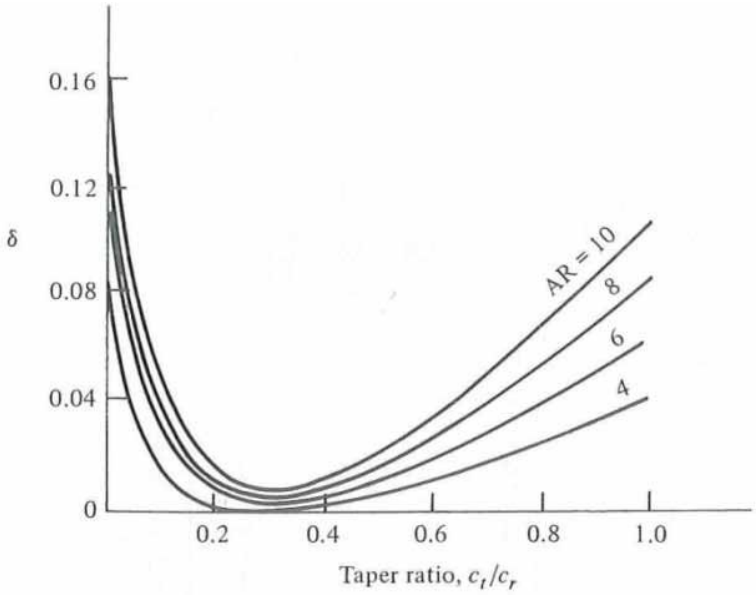

Figure 5.33: δ-taper ratio for various AR

Our purpose is to understand which taper ratio could give us the best compromise between efficiency and maximum Cl. In order to do that we tested six different tapered wing that would maintain the same wing surface. Taper ratio grows from 0.2 to 0.6 with a 0.1 step. Decreasing the taper ratio, because we maintain the same wing surface as said before, we get a larger root chord and a smaller tip chord. All these tapered wing was also compared with the untapered one. Geometries are reported in figure below with the pressure distribution on the suction side at 14° AoA.

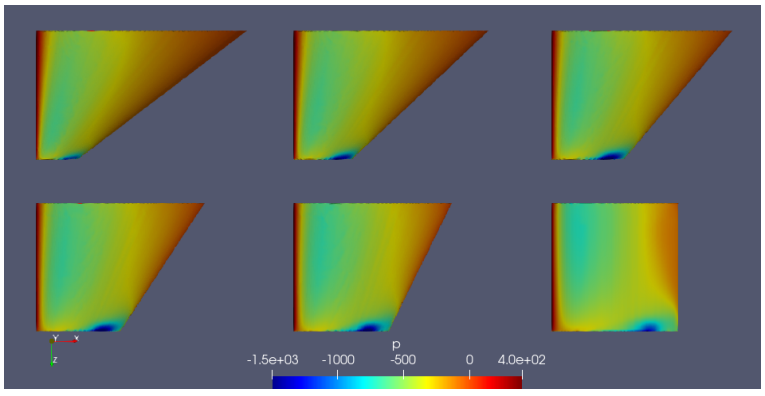

Figure 5.34: Different taper ratio geometry

We can see that low pressure region at the tip decrease with taper ratio until with taper ratio 0.2 is slightly visible.
We report the $Cl - \alpha$ and $Cl - Cd$ curves for these geometry.

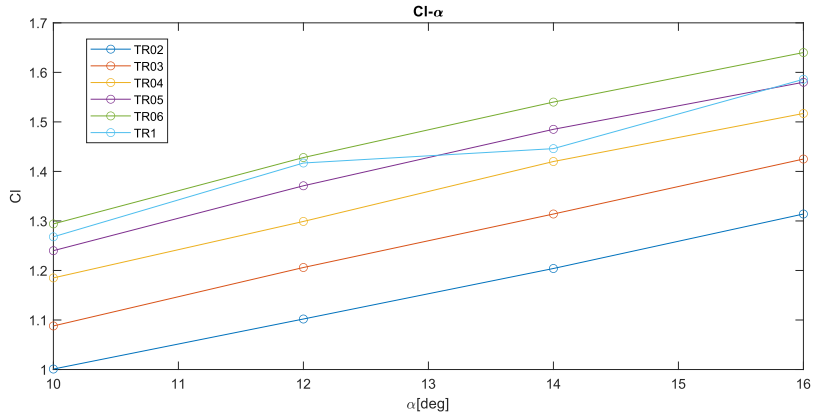

Figure 5.35: $Cl - \alpha$ for different taper ratio

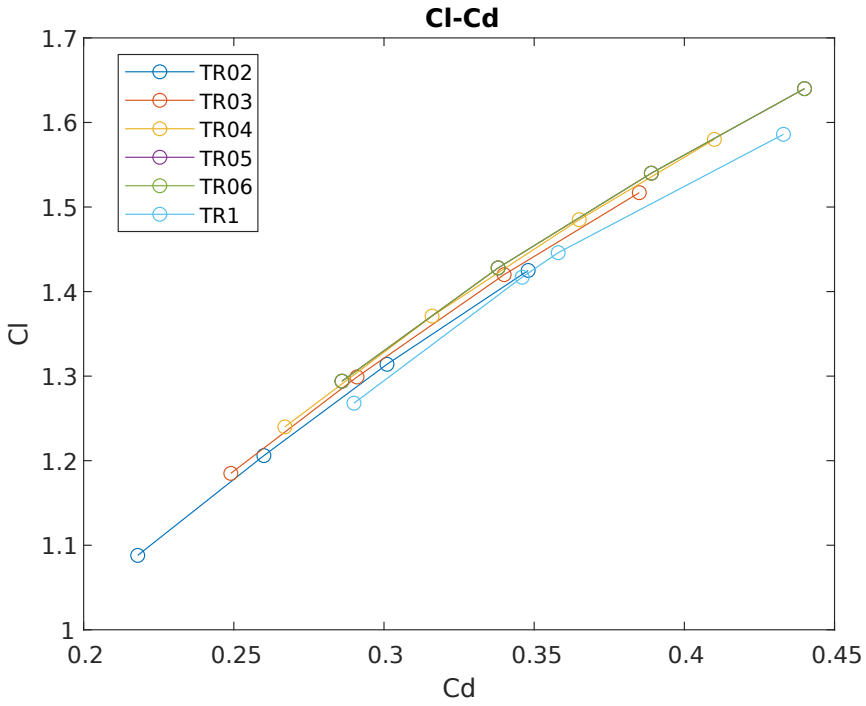

Figure 5.36: $Cl - Cd$ for different taper ratio

We can notice that taper ratio influence both Cl and Cd with any changes in the stall angle. More interesting solution is that with 0.6 taper ratio for which higher lift with higher efficiency is obtainable.

We looked also for obtaining a trend of δ of equation A.16. The procedure that follows allows to obtain only relative value: we know that elliptical wing has a δ equal to 0, instead in our case we arbitrary assign this value to the wing with less induced drag and from that we got the others. All the procedure is explained in detail below for a single

AoA. It will be repeated for all the AoA analyzed.

- we extract from CFD simulation value of Cl and Cd for all tested wings
- we calculate efficiency as Cl/Cd
- we calculate, for each wing the quantity described in following equation:

$$\frac{Cl^2}{\pi AR} \tag{5.6}$$

  that from theory is the induced drag of an elliptical wing with $\delta = 0$

- we subtract the quantity of equation 5.6 from the cd obtained from CFD simulation.

$$Cd - \frac{Cl^2}{\pi AR} \tag{5.7}$$

  At this point we got a value for each taper ratio and we select the smaller one. In this way we obtain an estimation of the sum of only viscous and pressure drag, without the induced component.

- we assumed that, keeping constant the AoA, the quantity calculated at previous point was constant for all taper ratio.
- we calculate a more accurate estimation for each taper ratio of the induced drag as follows:

$$Cd_{\mathrm{i}} = Cd - min\left[Cd - \frac{Cl^2}{\pi AR}\right] \tag{5.8}$$

- thanks to equation A.16 we get value of δ and Oswald efficiency e.

Repeating this procedure for all AoA just small variations of the value of δ are presents and the higher Oswald efficiency for all the AoA is reached by 0.6 tapered wing.
Tables with results are reported below

TR	Cl	Cd	E	$\frac{Cl^2}{\pi AR}$	$Cd - \frac{Cl^2}{\pi AR}$	Cd_i	$1+\delta$	δ	e
0.2	1.00	0.19	5.319	0.159	0.029	0.169	1.059	0.059	0.944
0.3	1.09	0.22	4.991	0.188	0.030	0.199	1.054	0.054	0.949
0.4	1.19	0.25	4.759	0.224	0.025	0.230	1.027	0.027	0.974
0.5	1.24	0.27	4.644	0.245	0.022	0.248	1.011	0.011	0.989
0.6	1.29	0.29	4.524	0.267	0.019	0.267	1.000	0.000	1.000
1	1.27	0.29	4.372	0.256	0.034	0.271	1.057	0.057	0.946

Table 5.1: δ evaluation at 10° AoA

TR	Cl	Cd	E	$\frac{Cl^2}{\pi AR}$	$Cd - \frac{Cl^2}{\pi AR}$	Cd_i	$1+\delta$	δ	e
0.2	1.10	0.23	4.812	0.193	0.036	0.216	1.115	0.115	0.896
0.3	1.21	0.26	4.638	0.232	0.028	0.247	1.065	0.065	0.939
0.4	1.30	0.29	4.464	0.269	0.022	0.278	1.034	0.034	0.968
0.5	1.37	0.32	4.339	0.299	0.017	0.303	1.011	0.011	0.989
0.6	1.43	0.34	4.225	0.325	0.013	0.325	1.000	0.000	1.000
1	1.42	0.35	4.095	0.320	0.026	0.333	1.041	0.041	0.961

Table 5.2: δ evaluation at 12° AoA

TR	Cl	Cd	E	$\frac{Cl^2}{\pi AR}$	$Cd - \frac{Cl^2}{\pi AR}$	Cd_i	$1+\delta$	δ	e
0.2	1.20	0.27	4.526	0.231	0.035	0.255	1.103	0.103	0.906
0.3	1.31	0.30	4.365	0.275	0.026	0.290	1.053	0.053	0.949
0.4	1.42	0.34	4.176	0.321	0.019	0.329	1.024	0.024	0.977
0.5	1.49	0.37	4.068	0.351	0.014	0.354	1.007	0.007	0.993
0.6	1.54	0.39	3.959	0.378	0.011	0.378	1.000	0.000	1.000
1	1.45	0.36	4.039	0.333	0.025	0.347	1.041	0.041	0.960

Table 5.3: δ evaluation at 14° AoA

TR	Cl	Cd	E	$\frac{Cl^2}{\pi AR}$	$Cd - \frac{Cl^2}{\pi AR}$	Cd_i	$1+\delta$	δ	e
0.2	1.31	0.31	4.226	0.273	0.037	0.298	1.092	0.092	0.916
0.3	1.43	0.35	4.095	0.323	0.025	0.336	1.040	0.040	0.962
0.4	1.52	0.39	3.940	0.366	0.019	0.373	1.019	0.019	0.982
0.5	1.58	0.41	3.854	0.398	0.012	0.398	1.002	0.002	0.998
0.6	1.64	0.44	3.727	0.428	0.012	0.428	1.000	0.000	1.000
1	1.59	0.43	3.663	0.401	0.032	0.421	1.052	0.052	0.951

Table 5.4: δ evaluation at 14° AoA

Next graph summarize the results of previous tables.

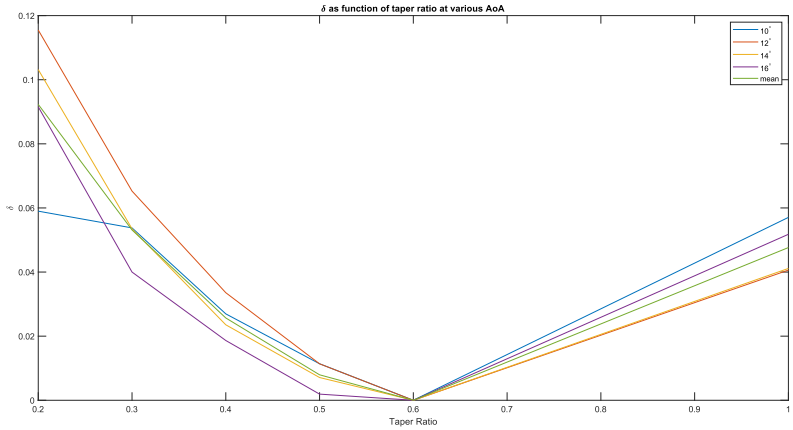

Figure 5.37: δ for different taper ratio at different AoA

This considerations lead us to the choice of 0.6 taper ratio wing that we used for further studies and developement.

5.5.4. Sweep angle influence

Sweep angle is primarily used in transonic and supersonic field, instead in subsonic field it generally does not take any advantages. However we considered it as possible interesting parameter because moving the tip back, or forth in case of negative sweep angle, with respect to the root, also the tip vortex position will change and that could have some influence on wing performance.
For this test we selected sweep angles equal to $-10°, 0°, 10°, 20°$ and $30°$. Geometries are reported in figure below with the pressure distribution on the suction side at 14° AoA.

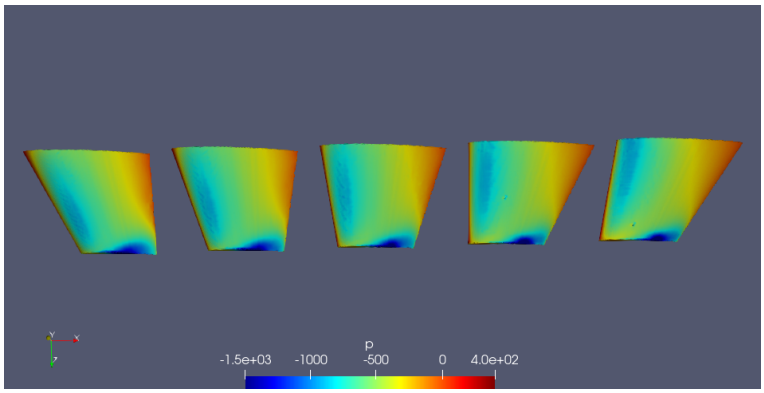

Figure 5.38: Different sweep angle geometry

In next table we report simulation results: We can not appreciate a significant variation

	F-10	F0	F10	F20	F30
Cl	1.62	1.64	1.64	1.65	1.60
Cd	0.43	0.44	0.44	0.44	0.43
E	3.80	3.75	3.72	3.72	3.75

with the sweep angle. We select a sweep angle that is the one presents the highest lift coefficient

5.5.5. Planform modification and shaped endplates

Once taper ratio and sweep angle was choosen, another planform modification has been done in order to improve plan surface. In fact, keeping constant the span, the root and tip chord, so keeping constant the encumbrances of the wing, by modifying leading edge curvature it is possible to obtain a little increase of the surface. Geometry obtained with this modification, that we will call JG0, is represented in following figure.

Figure 5.39: JG0 wing geometry

A more extensive study could be done for the planform geometry, proceeding with a parametric study and testing different curvature for the leading edge.
Fixed the planform we continued with a study on tip devices. first of all, the simple endplate of section 5.5.2 applied to this wing planform, in figure 5.42

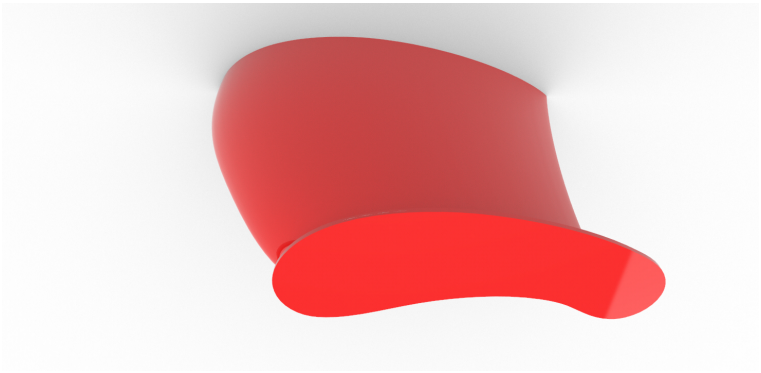

Figure 5.40: JG0 with simple endplates

In the following we will presents an analysis of different tip device solution.
In this section, we will refer to the tip device with the name of winglets, this time used with the aeronautical meaning.
Due to time and computational power constraints the following analysis departs from the quite detailed sensitivity study done so far. We limited ourselves to studying a few solutions, without thoroughly analysing all possible geometric parameters.However a considerable performance improvement was achieved thanks to this simple analysis.
First solution, that we will call JG1, presents a planar endplate which shape aims to reduce the end vortex as much as possible, while minimising the wet surface, as an increase of surface implies an increase in frictional drag. For this purpose, we relied on a visualization of the JG0 wing (5.39) In particular we plotted on a z-normal plane, located at the tip, a contour of the module of z-velocity and we imposed a threshold below which contour transparency is set to 100%. In this way is possible to see in which region z-component of the velocity, so the vortex, is stronger. This visualization was than imported as background in Rhinoceros^{TM}, so that we can use it as reference to construct geometry. Following figure show the visualization obtained and the construction lines used for the upper part of this kind of endplates.

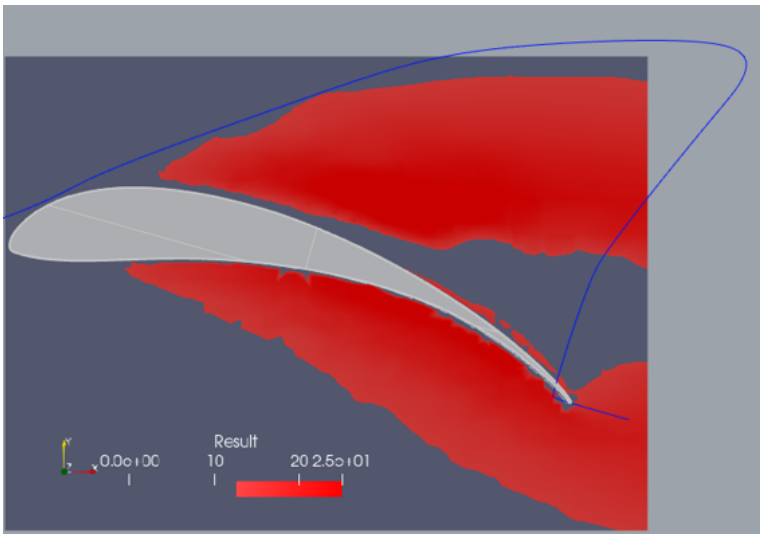

Figure 5.41: Construction Lines of JG1 enplate

Geometry obtained is reported in next figure.

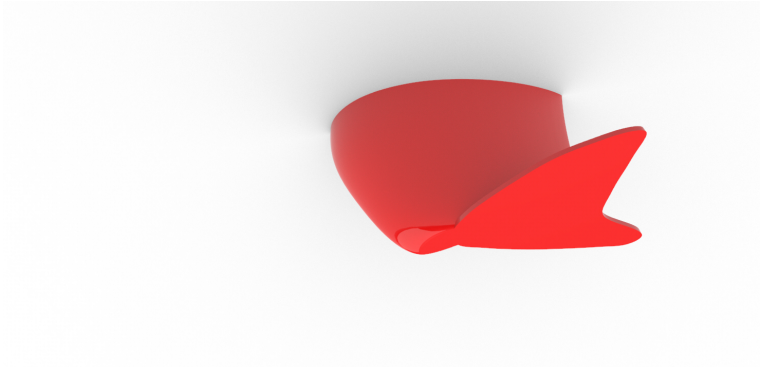

Figure 5.42: JG1 wing geometry

We can see from pressure visualization of figures 5.44 and 5.43 that the low pressure peak on the upper surface of the tip is not present anymore, which will lead to a lower lift, instead a significant benefit is given by the lower surface in which tip effects become smaller and a quite constant pressure distribution is achieved.

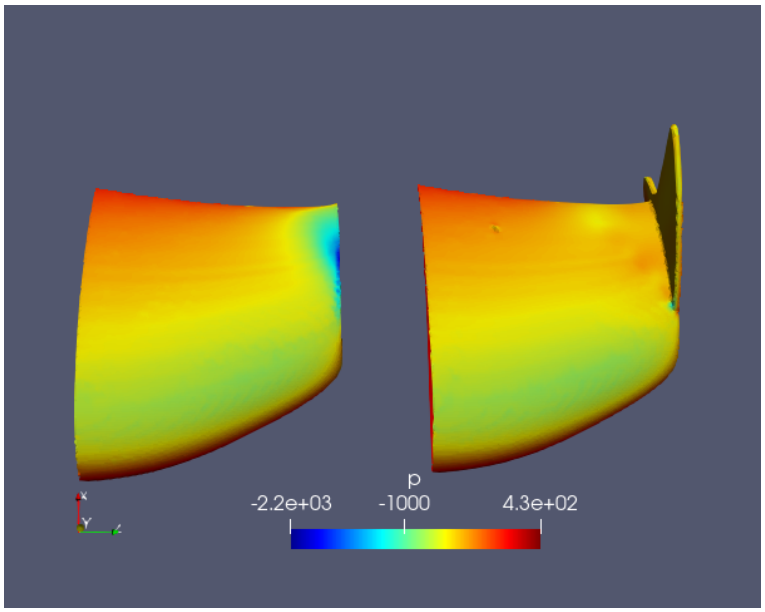

Figure 5.43: Pressure distribution on upper side of JG0 and JG1 wing at 15° AoA

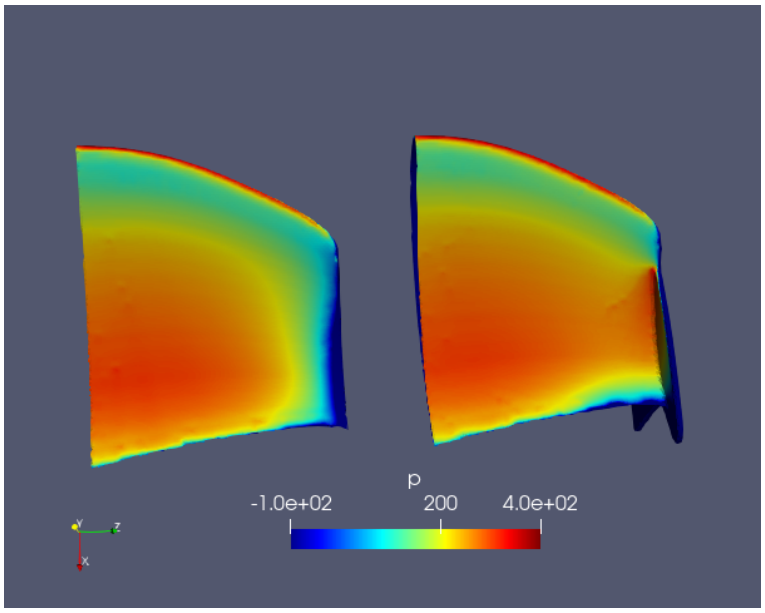

Figure 5.44: Pressure distribution on lower side of JG0 and JG1 wing at 15° AoA

This trade from pressure increase in tip zone both in lower surface both in upper surface results in a very small increase in lift coefficient that becomes 1.78 with a drag reduction equal to 3.9%.

Next solution aims to increase pressure on lower side without lose the favorable low pressure region on the upper surface. In order to do that we substitute the thin plate geometry with an shaped geometry. From the upper view, as reported in figure 5.48, the

endplate section consists of an airfoil, in particular E387. Obviously an accurate study should consider the influence of the airfoil chosen for the endplate. However, as said before, it will be lot time consuming and need a lot of computational power. We opted for the E387 because, of all the profiles studied by us is the one with higher efficiency. In fact, for this vertical winglet we don't need a higher lift as in the wing but we want just obtain a low pressure zone that mimic the one generated by the tip vortex, without excessive further increase of drag.

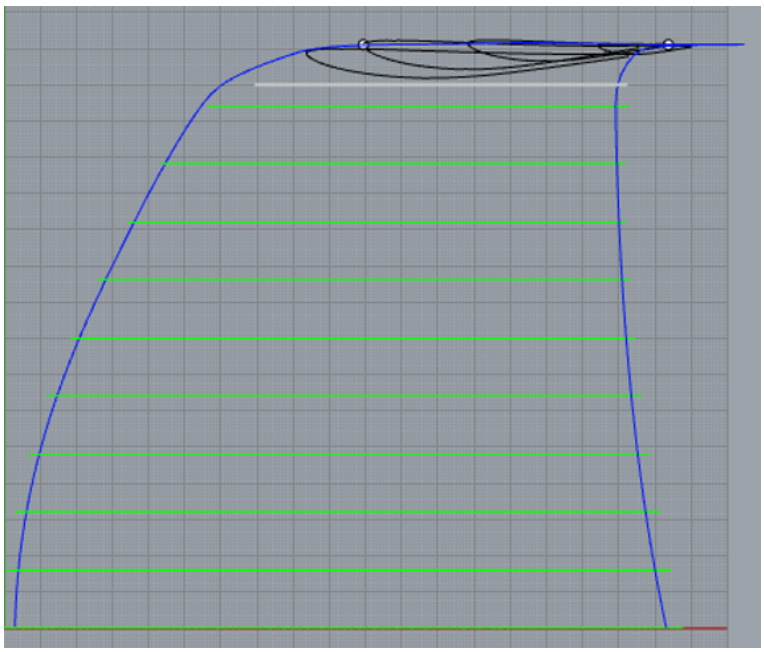

Figure 5.45: Construction line for E387 winglet

Another parameter that could be have a great influence is the angle, in y-normal plane, with respect to the freestream flow. We limited our study to two cases, first one at 0° and another one at 4° as in figure **??**

(a) 0° (b) 4°

Figure 5.46: Construction lines for differently angled winglets

An example of obtained geometry, that we will call JG2, for the 0° angle winglet, and JG3 for the for the 4° angle winglet, is reported below.

Figure 5.47: JG2 geometry

In this geometries we can see that the winglet is positioned perpendicular to the wing. Another possible parameter is the angle formed between the plane of the winglet and that of the wing, as in next figure.

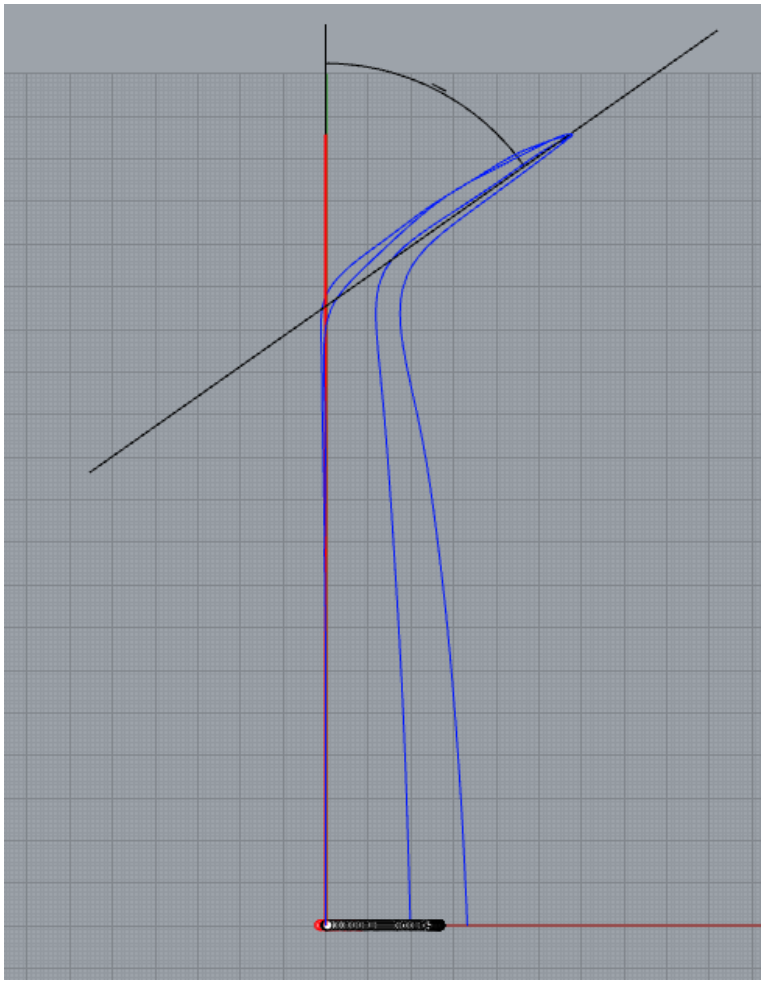

Figure 5.48: ψ angle definition

We will call this angle ψ. In order to have an idea of the influence of ψ, we analyzed also a configuration in which winglet plane forms an angle of 60° with the y-normal plane. However a similar geometry, fixed the maximum span, reduces the effective area because such a winglet has an horizontal footprint due to ψ. We now present a comparison of pressure distribution on lower side 5.49 and upper side 5.50 of the wing just described at 15° AoA.

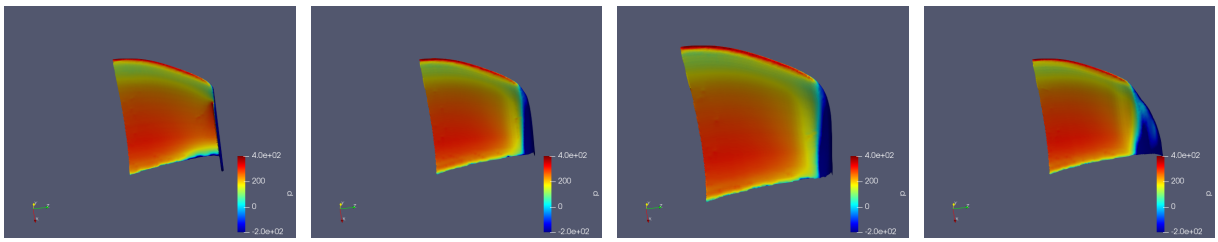

(a) JG1 (b) JG2 (c) JG3 (d) JG4

Figure 5.49: Pressure distribution on lower side of different wings at 15° AoA

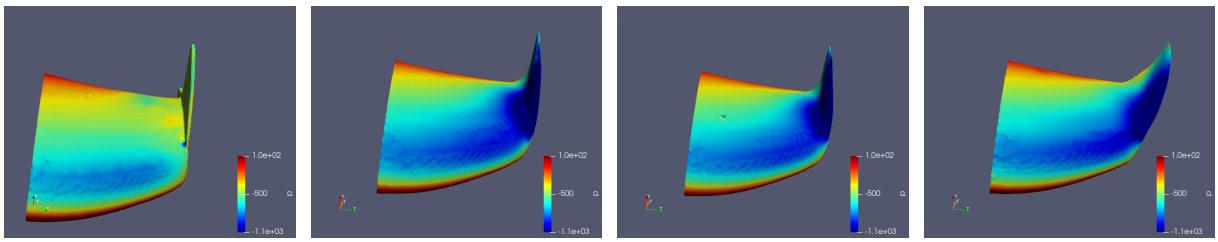

(a) JG1 (b) JG2 (c) JG3 (d) JG4

Figure 5.50: Pressure distribution on lower side of different wings at 15° AoA

Results, in terms of force coefficient, are reported in following table.

	JG1	**JG2**	**JG3**	**JG4**
Cl	1.78	1.99	1.92	1.83
Cd	0.418	0.454	0.435	0.396
E	3.8	4.38	4.41	4.62

It is clear that ψ can bring advantages in terms of efficiency and drag reduction but penalises maximum Cl, with respect having $\psi = 90$. This Cl reduction was expected because, as said before, last part of the wing is sacrificed in order to have place for the winglet. However a consistent improvement on maximum Cl was achieved by all the wing with shaped winglet. which effects are visible in figure 5.50: a consistent pressure

reduction on the upper surface is achieved thanks to the low pressure zone imposed by the E387 upper surface. However, looking at figure 5.49, we can see that missing the lower part of the winglet a little loss of pressure is present on the pressure side, near the tip. This loss drove us to design a last geometry that we will present in the following.
Regarding drag reduction is interesting to see how different solution affects streamlines (5.51) and vortex shape (6.17).

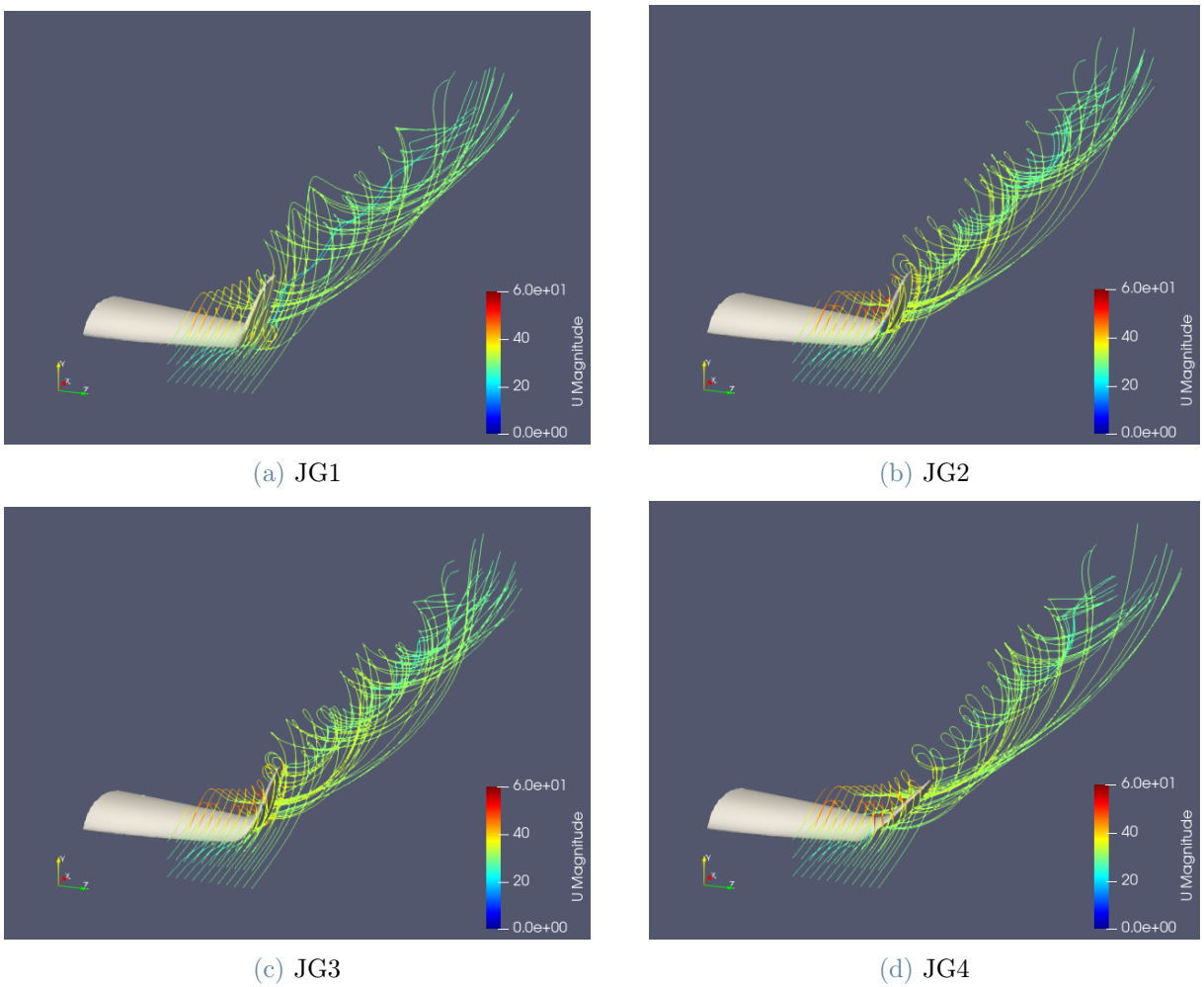

(a) JG1 (b) JG2

(c) JG3 (d) JG4

Figure 5.51: Velocity streamlines of different wings at 15° AoA

We can see that shaped winglet are more capable to avoid vortex generation, in particular the one mounted in JG4 wing. In next figure we report isolines of x-vorticity plotted on x-normal planes at various distance from the trailing edge.
In particular, distance from the leading edge is:

- 1c for the nearest plane
- 2c for the secon plane

- 4c for the third plane
- 6c for the last plane

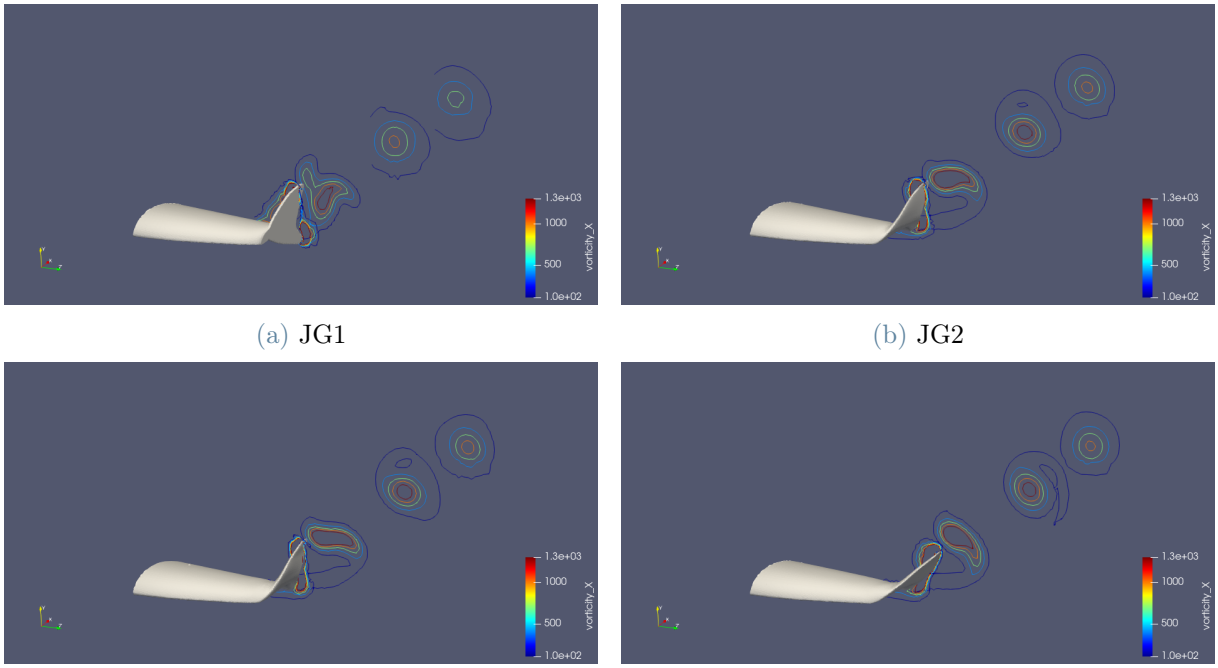

(a) JG1 (b) JG2

(c) JG3 (d) JG4

Figure 5.52: Contours of x component of the vorticity in the wake of different wings at 15° AoA

Near the trailing edge we can see strong changes in vortex shape between the flat plate endplate and the shaped winglets, with also a good reduction of initial vortex dimensions. Instead, focusing on the latest analyzed plane, at 6c from the leading edge, we can see in next figure that the shape returns to being circular for all wing geometries. However wings with shaped winglet presents higher value of x-vorticity in the far wake.

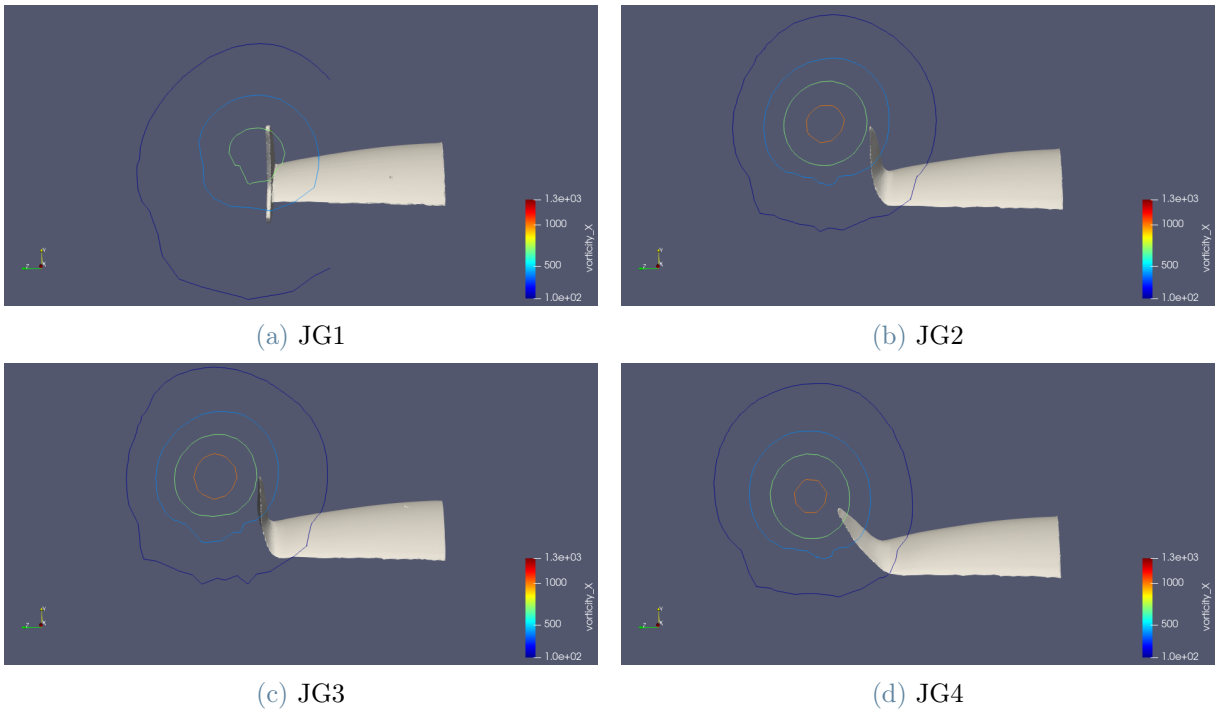

(a) JG1 (b) JG2

(c) JG3 (d) JG4

Figure 5.53: Contours of x component of the vorticity in the far wake for different wing at 15° AoA

We now present last geometry analyzed. This wing was developed from JG2, that was the one with high lift coefficient. As said before, looking at figure 5.49b, we can see a little loss of pressure in the tip zone of high pressure side. In order to reduce this pressure loss we design a lower endplate. Design technique is similar to the one used for JG1 wing. We report for clarity the visualization and the construction lines, as in figure 5.42,

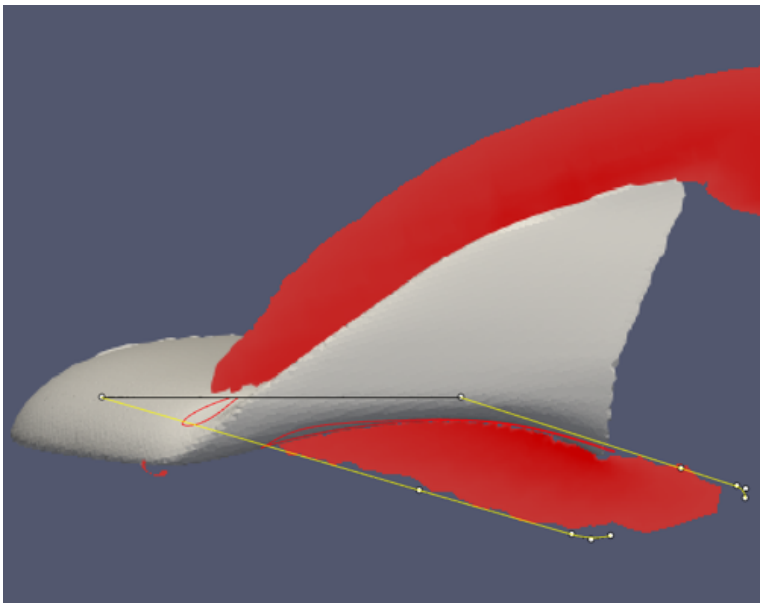

Figure 5.54: JG5 construction lines

The most important difference is that for this endplate the airfoil has been reversed in order to have the pressure side of the airfoil facing towards the wing and the lower pressure side outwards.
Resulting pressure distribution is reported in next figure with a comparison with JG2 wing in order to better capture advantages of this solution.

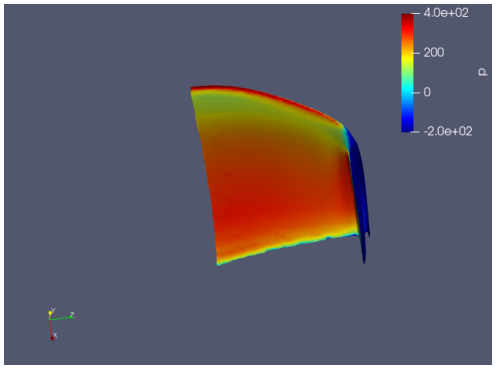

(a) High pressure side JG5

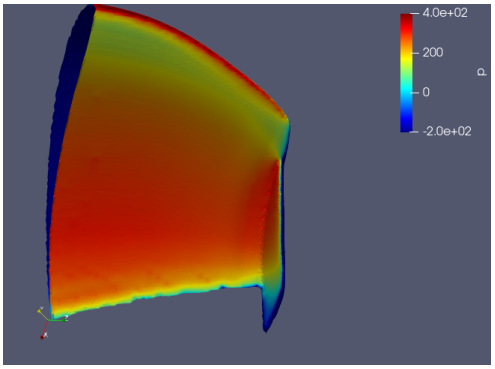

(b) High pressure side JG5

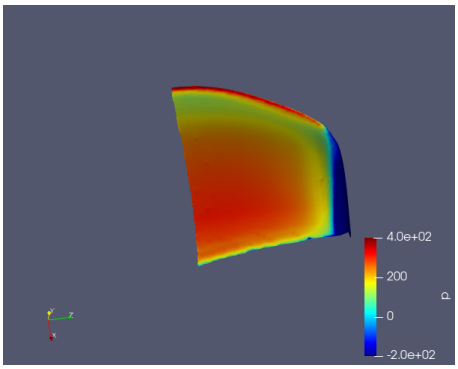

(c) High pressure side JG2

This positive variation in pressure distribution led to 0.5% increase in Cl but also to 4.4% reduction in drag coefficient, probably due to the strong modification that this solution impose on the vortex. In next figure, in fact, we can see that the combination of a winglet and a lower endplate tends, in the proximity of the trailing edge, to split the tip vortex in two smaller vortex.

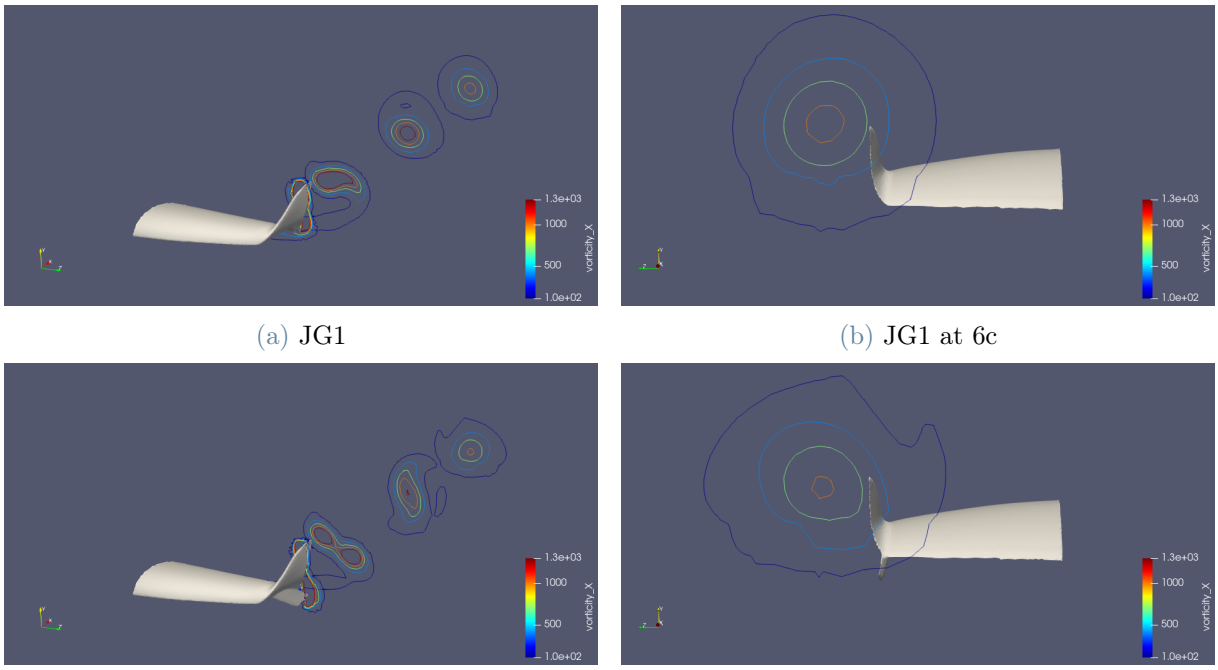

(a) JG1 (b) JG1 at 6c

(c) JG5 (d) JG5 at 6c

Figure 5.55: Contours of x component of the vorticity for JG2 and JG5 wings

5.5.6. Final geometry and further possible studies

To continue our work we chose the JG5 wing that is depicted in next figure.

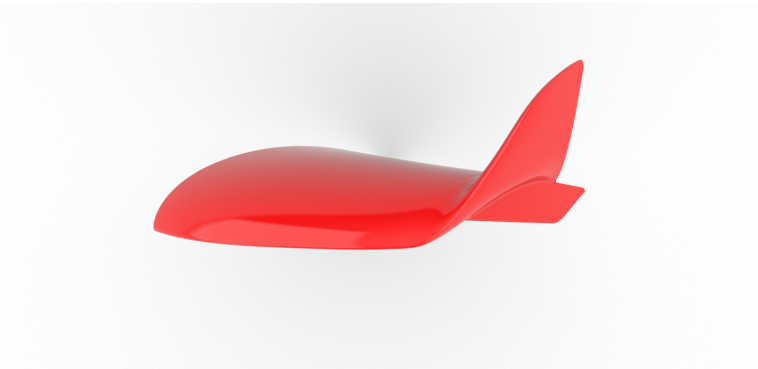

Figure 5.56: JG5 wing rendering

Our choice was driven primarily by the maximum lift coefficient obtainable. Force coefficient and efficiency are recapped in next table.

Cl	Cd	e
2.00	0.44	4.56

As said before our study was limited by time and computational power available and some aspects was neglected. It might be interesting to do a more in-depth study about planform shape, introducing a parameterisation that could take into account of curvature of leading and trailing edge. Regarding winglets used a very detailed study can be done in order to find the optimum solution. First of all it will be useful to understand the influence of the airfoil chosen for their construction, than a complete study about the angle that the winglet forms with the flow direction but also a more accurate analysis of the lateral shape of that. Furthermore, planform choice and winglet choice may not be fully independent as considered in our study. Removing this assumption test cases become much more numerous and may be required to use an optimisation method. Last interesting parameter that we neglect is the twist angle of the wing that could lead relevant benefits, specially in therms of drag as the root part of the wing, at maximum lift coefficient starts to stall before the one of tip region.

6 | Motorbike aerodynamics

6.1. Validation of the Model

In this chapter we want to push our studies even further by going to analyze the true field of air motion that invests a speed bike with the intention of dwelling on the behavior of the aerodynamic fins studied in the previous chapters, which will be mounted on the fairing of the bike itself. In the first part we will address the problem of validating the aerodynamic model, in particular leaning on the values obtained from tests of the entire motorcycle in the wind tunnel.

6.1.1. Wind Tunnel

The wind tunnel where the bike was tested is the GVPM at the Politecnico di Milano, built in 2001. It is a closed-circuit wind tunnel that, as is shown in the figure, boasts as many as two test chambers.

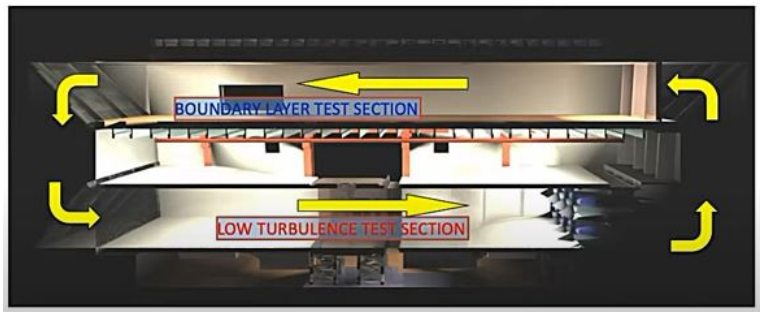

Figure 6.1: Polimi Wind Tunnel

Boundary layer test section

Representing the largest test chamber, it is really huge with dimensions: 14.84m wide x 3.84m high and 35m long. The maximum speed achievable in this section is 16m/s with velocity variations around 5% and turbulence intensity that can vary from 2% to 35%. This is in order to be able to reconstruct the Earth's boundary layer as plausibly as possible. In fact, this tunnel section is used for aeroelastic models of long span bridges, sailing yachts, static and dynamic bridges, scaled wind turbines models and wind farms.

Figure 6.2: Boundary layer test section

Low turbulence test section

The airflow is then conveyed to a much smaller section than the previous one, and low turbulence tests are done here. The low turbulence section is much smaller in size but still remains a rather large test chamber in fact it can accommodate even full size vehicles. In fact it is 4m wide, 3.84m high and 6m long, the maximum speed that can be reached is 55m/s with a very low turbulence intensity i.e. 0.1% with speed variations of 0.25%. In this test section of the tunnel, scale models of airplanes, high-speed trains, sports aerodynamics and more generally the aerodynamics of land vehicles are tested. The test chamber similarly to the boundary layer chamber has a circular support surface with a diameter of 2.5m that can rotate according to the direction of the current; in addition, the test chamber is fully movable and by means of an air levitation system can also be totally removed and used in open-jet mode if the study requires that the walls must be removed (for example, the case of helicopter rotors in hovering condition).

Figure 6.3: Low turbolence test section

Power is put into circulation by 14 motors of 100kW each independent of each other and powered by inverters. As we know, in addition to nets and honeycomb structures to stabilize the flow, being a closed-circuit tunnel it also has an air cooling system that keeps the physical characteristics of the air constant throughout the tests.

6.1.2. Motorbike model

The motorcycle tested is the Nyx, a prototype built entirely by the university's Polimi Motorcycle Factory racing department. It was created as a result of an innovative design from both an energy and aerodynamic point of view. The trellis frame architecture is built with welded steel tubulars connected through geometric constraints with numerically controlled milled aluminum plates. The motor is a three-phase Engiro 205° electric motor with 4 pole pairs capable of a rated power of 13kW and maximum power of 44kW with maximum available torque of 100Nm, all of which is powered by a custom-designed battery pack with a capacity of 8kWh managed by an internally operated BMS. As for aerodynamics, the fairing geometry had already been the result of aerodynamic studies based on CFD simulations with the aim of minimizing drag and wake size. The choice of this motorbike is strictly related to the needs to have a reliable CAD model.

6.1.3. Validation geometry and setup

In order to validate our model, we started by reproducing as faithfully as possible the domain present in the tunnel. In fact, we placed the simplified CAD model of the motor-

cycle on the platform present in the tunnel and surrounded by the tunnel walls respecting the exact dimensions. Furthermore, the domain was also extended both in front of the bike, to give space for the current to even out from the Inlet wall, and in the rear to better capture even the farthest wake. The rider is not present because, since this is a validation case, it would have been impossible to reproduce accurately enough the tonnage and exact posture of the real rider, had he been present in the tunnel tests. Tires interpenetrate the floor by 4mm in order to have a better modeling of tire footprint on the ground. In the figure below we find schematized the computational domain and the geometry used.

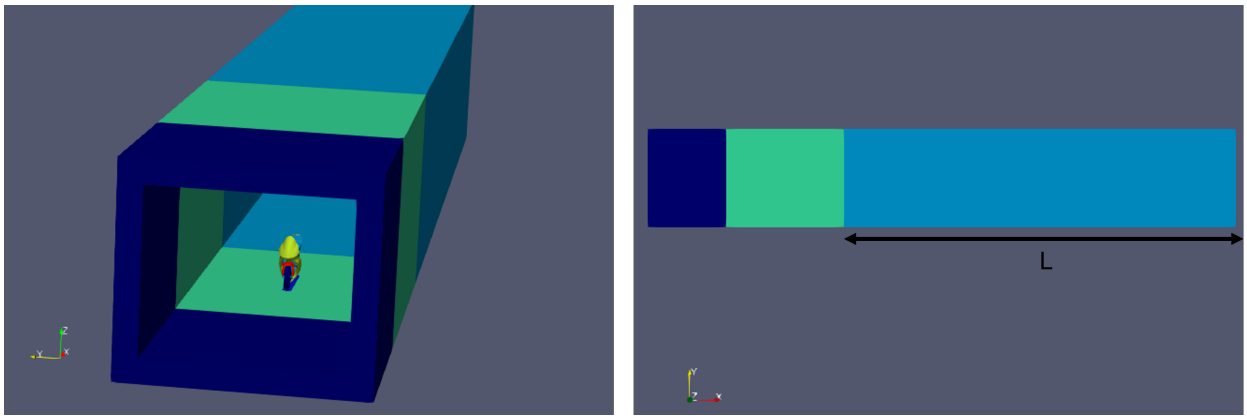

Figure 6.4: Computational domain for motorbike numerical setup validation

We can notice the presence of two additional part, not present in the real wind tunnel test section. This addition was was necessary to completely capture the wake and to have a uniform inlet pressure. At this purpose, we made a domain dependence study, first by increasing the front part of the domain (the dark blue box in figure 6.4 then going to increase the length of the domain behind the bike (the light blue box in figure 6.4) from 15m up to 20m and 25m. In the last two cases we noticed that the wake was well captured, as in figure 6.5, the sections far in the wake showed a quite uniform distribution in terms of velocity and, moreover, aerodynamic coefficients of motorbike remain unchanged.

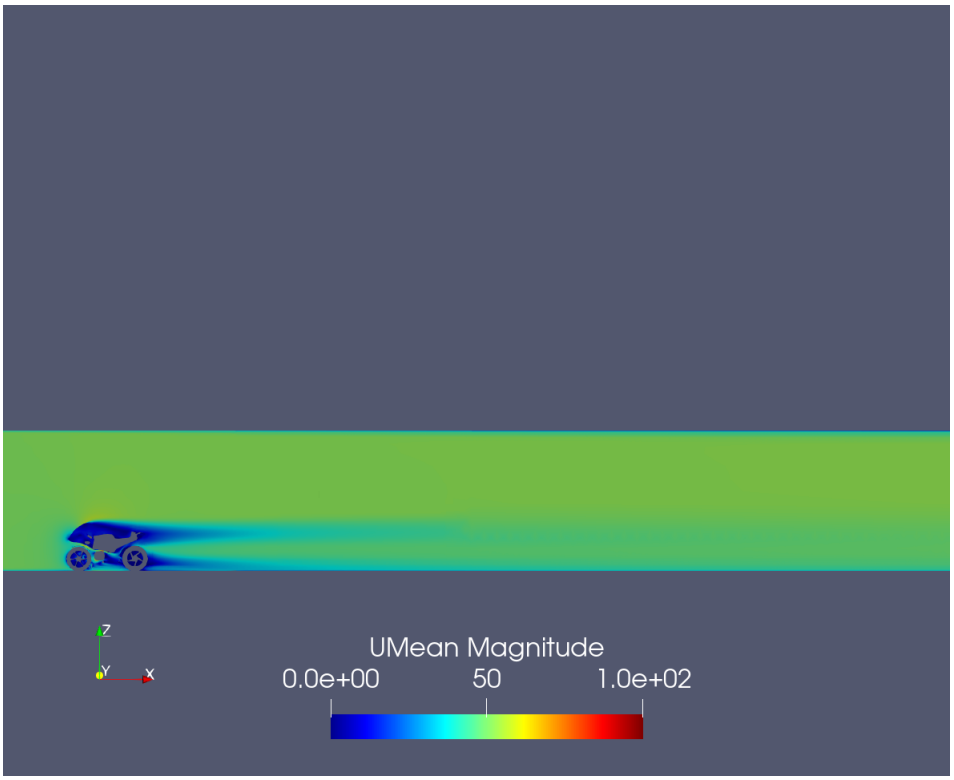

Figure 6.5: Velocity field behind motorbike in wind tunnel

Regarding the boundary conditions we set:

- INLET: 'FixedValue' conditions for the speed, set at 50m/s and 'ZeroGradient' for the Pressure.
- OUTLET: 'FixedValue' with imposed value of 0 for the Pressure, and 'ZeroGradient' for the speed.
- 'No-slip' condition on both all components of the bike and the test section walls and in the wake.
- 'Slip' condition on the wall placed before the test section, in order to avoiding a premature grow of boundary layer.

  The 'Symmetry' condition used in the case of the 3d wing study could not be used because the motorbike has some asymmetrical geometries such the presence of brake caliper only on the left. These differences are minimal but can however alter the validation result.

6.1.4. Mesh description and grid convergence

Also in this case software used is SnappyHexMesh.
The domain presents a first level of cell partitioning in the entire control volume, after which we constructed a first level 2 refinement box that extended partially in the front of the bike and to the far wake. To further refine the mesh near the complex geometry of the bike imposed an additional Level 3 refinement box that would include the entire bike, a portion of the front domain, and extend sufficiently into the wake. Additional Level 5 surface refinements were added on each component of the motorbike, as in the test section walls. A level 2 surface refinement was needed also on 'not physical' wall of the domain in order to avoid a too large discontinuity between cells and to be able, also with coarser meshes, to exactly reproduce domain dimension. We report here for clearance the resultant mesh obtained without the refinement just described.

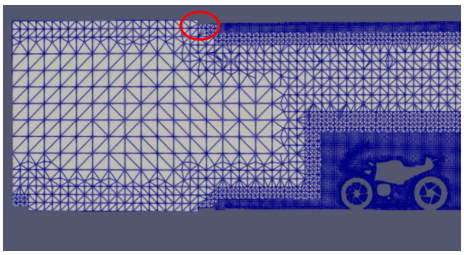

Figure 6.6: Error generated by bad mesh refinement in motorbike domain

Finally, we add 5 layers on all physical surfaces to better capture the boundary layer. Resulting mesh is reported in figures (6.7) and (6.8).

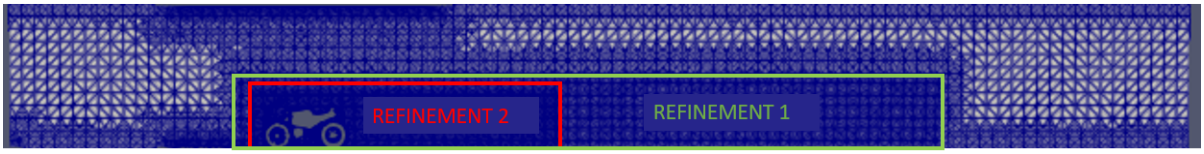

Figure 6.7: Mesh refinement boxes for motorbike numerical simulation

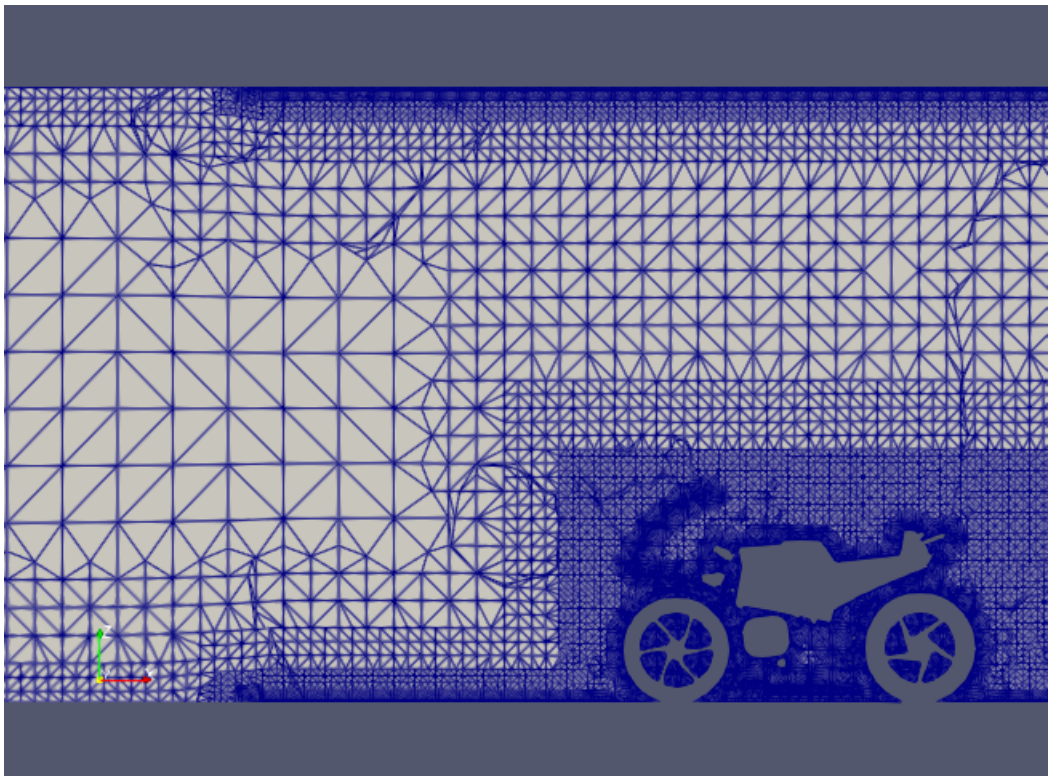

Figure 6.8: Motorbike mesh details

A grid convergence study, as in the previous sections, also in this case has been developed. In the following figure we show the trend of drag force with number of cells :

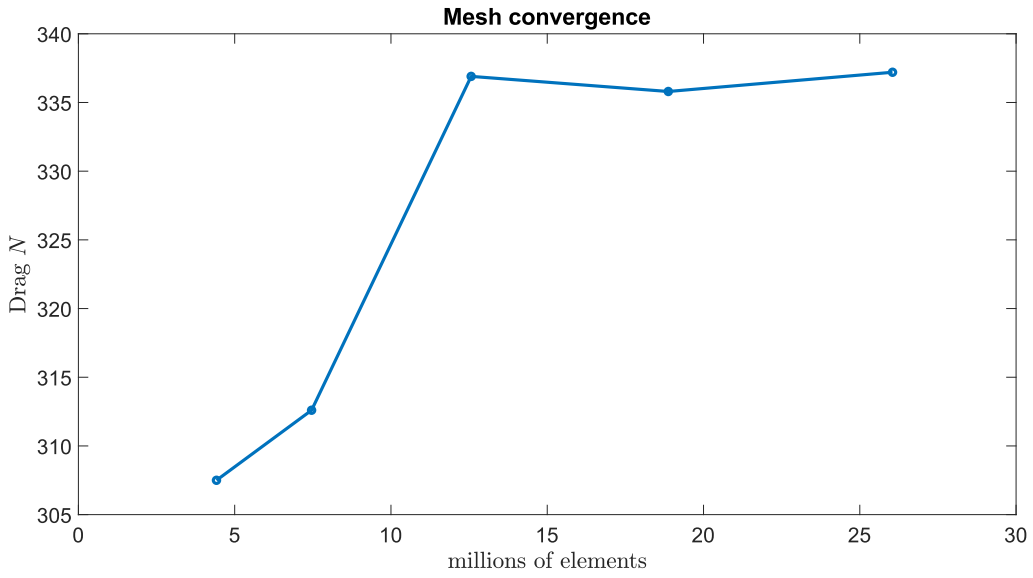

Figure 6.9: Motorbike mesh convergence

A more efficient computational model is achievable considering boundary layer displacement thickness on the test section walls. In particular it is possible, adding this thickness to the upper and lateral wall of the cad model, eliminate the layer elements, reducing the total number of cells. An estimation of displacement thickness for laminar boundary layer on flat plate was give by Blasius.

$$\delta^* = \frac{1.72x}{Re_x} \tag{6.1}$$

6.1.5. Turbulence model and numerical schemes

Again, since this is a stationary simulation we used simpleFoam as solver, with $k-\omega$ SST turbulence models in which k and ω were initialized as follows.

$$k = \frac{3}{2}(Ui)^2 \tag{6.2}$$

in which turbulence intensity $i = 0.1\%$ and U, as said before is 50m/s. Regarding ω instead we can extimate it from 6.3

$$\omega = \frac{\sqrt{k}}{l_t} \tag{6.3}$$

where l_t, turbulent length scale can be estimated with $l_t = 0.038D_h$, in which D_h is the hydraulic diameter and equal to 4.4 meters.

Solvers

Also for this case in terms of solvers we used GAMG (generalised geometric-algebraic multi-grid) for pressure and ϕ, symGaussSeidel as smoother with tolerance 1e-12 and reltol 1e-4. While for κ and ω we used PBiCGStab with DILU preconditioner with tolerance 1e-12 and reltol 1e-5.

Numerical schemes

For the numerical schemes as follows:

Divergence scheme	2°order
$\mathbf{div}(\phi, U)$	*bounded Gauss linearUpwindV grad(U);*
$\mathbf{div}(\phi, \kappa)$	*bounded Gauss Upwind;*
$\mathbf{div}(\phi, \omega)$	*bounded Gauss Upwind grad(ω);*
$\mathbf{div}((\nu Eff^* dev2(T(grad(U)))))$	*Gauss linear;*

Table 6.1: divergence schemes

residuals control

We imposed the following convergence criteria on the residuals for our simulations:

residual tolerace

Parameter	value
U	*1e-3*
p	*1e-3*

Table 6.2: residuals control

6.1.6. Validation results

Results from our CFD simulation presents an underestimation of about 10% in drag force. We had to consider that the CAD model presents some simplifications, specially in the internal zone of the motorbike. This simplification can not represent in detail the internal aerodynamic, leaving place to the air to flow undisturbed in the zone between engine and fairings. A complete CAD model would need a much more complex and computational costly numerical model, that however would not impact considerably on our external aerodynamic study. We report, in the following table, a comparison between wind tunnel results and the drag coefficient obtained averaging CFD results of last 600 iteration.

height	Wind tunnel	CFD
Drag force	337.2	368
-	-	

Table 6.3: Results comparison between wind tunnel and CFD

6.2. Motorbike in real operating conditions

In this section we are going to analyze the aerodynamics of the motorcycle no longer placed in the wind tunnel but in more circuit-like conditions. In particular, we will focus on comparing motorcycles with simple fairing and with the addition of fins. We will try two different setup configurations (straight and lean bikes) and multiple mounting positions of the fins on the fairing.
In order to reproduce the current conditions outside the tunnel, we made some modifications to the validation model used previously.

6.2.1. Numerical model

After validating the computational model by reconstructing as faithfully as possible the conditions that were present in the tests performed in the wind tunnel, we want to obtain some results with conditions that are as similar as possible to those that the bike will encounter once it hits the track. Below we explain each one by one the changes made to the validation model to best fit our case of interest:

Geometry and setup We started from the model just presented for the validation case adding the rider on the bike's seat. During validation, in fact, the rider was not present

since it would have been difficult to reproduce both the rider's position and tonnage in terms of CAD modeling.
The second change concerns the computational domain: whereas before we found the motorcycle positioned in the center of the domain surrounded by the tunnel walls and resting on a platform with stationary wheels in this case the tunnel walls have been removed and the dimensions of the domain have changed slightly. In fact, we modified the height of the domain by increasing it by two meters and the width by increasing it by 1m on each side.

Boundary conditions

Some modification was also made on the boundary conditions in fact by removing the tunnel walls and analyzing only half of the domain the conditions at the walls became:

- Upperwall: from no-slip wall to slip wall boundary condition
- Lowerwall: from no-slip wall to fixedValue for velocity to simulate ground velocity and zero gradient for pressure
- FrontandBack: from no-slip wall to slip wall boundary condition
- Wheels: from simple no-slip condition to rotatingWallVelocity condition imposed to the tyres.

We didn't model the rotation of spoke of the wheels because an unsteady simulation with a moving mesh would have required too much computational cost. Furthermore MRF (moving reference frame) does not give accurate results and the implementation of a more accurate model goes beyond the objectives of the thesis. Moreover, since non-symmetrical geometries were of minor importance and, as said before, involved only brake calipers we decide, for straight line motion, to simulate just half of the domain. The use of just half domain allowed us, being simulations faster and less computational consuming, to trying out different solutions. Regarding cornering motion obviously we used the entire domain.

Mesh

Regarding the mesh, the exact same settings used in the fourth mesh of validation case have been kept. Even if the third mesh was in agreement with the finer ones we chose to be conservative and use the fourth one in order to be sure to well capture the flow field also when winglets will be installed. Mesh setup was just adapted to the changes done to the geometry: we added layers on the rider and we remove them from the domain wall,

as, this time, are modeled as slip wall.

6.2.2. Rectilinear motion

Initially, we did a first simulation without winglets. Its results was used both for comparative purposes, both to, through Paraview visualization, understand which position on the fairings was the most convenient to place winglets. In order to do that, we visualized the p_{tot} on some plane, parallel to the ground, at various height. Results are reported below

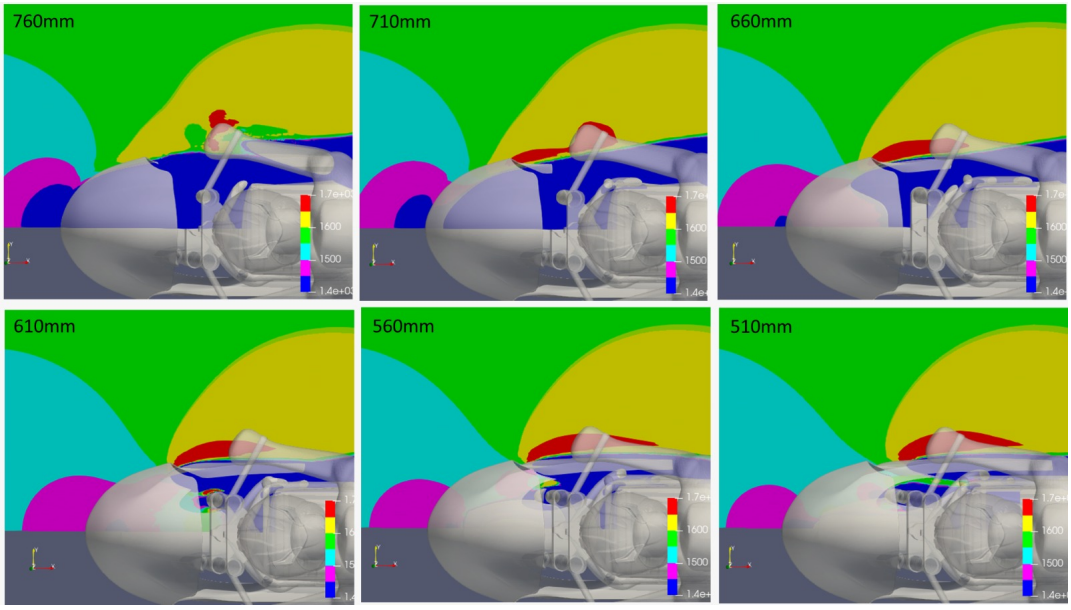

Figure 6.10: p_{tot} contours around motorcycle on planes at different heights from the ground

We can notice, descending with height, the growth of an high total pressure area that we expect to be beneficial for the functioning of the winglets. We did not analyse lower zone because we had to ensure that during cornering, at high lean angle, winglets do not touch the ground. Moreover, more we move down in the fairings, more our simplification done on the wheels becomes unacceptable. Another parameter to take into account is the local flow direction. In particular the flow could not be aligned with freestream flow, acquiring a speed both in y both in z direction. An induced velocity in z direction would change the effective angle of attack of the winglets, instead an induced y velocity would generate a not desired sweep angle. To take into account of this flow direction changes, we plot on the same plane used for the p_{tot} the side and the 'vertical' angle. Knowing the variation of direction we can modify the placement of the winglets such that they works in a condition as possible similar to the one in which they was designed.

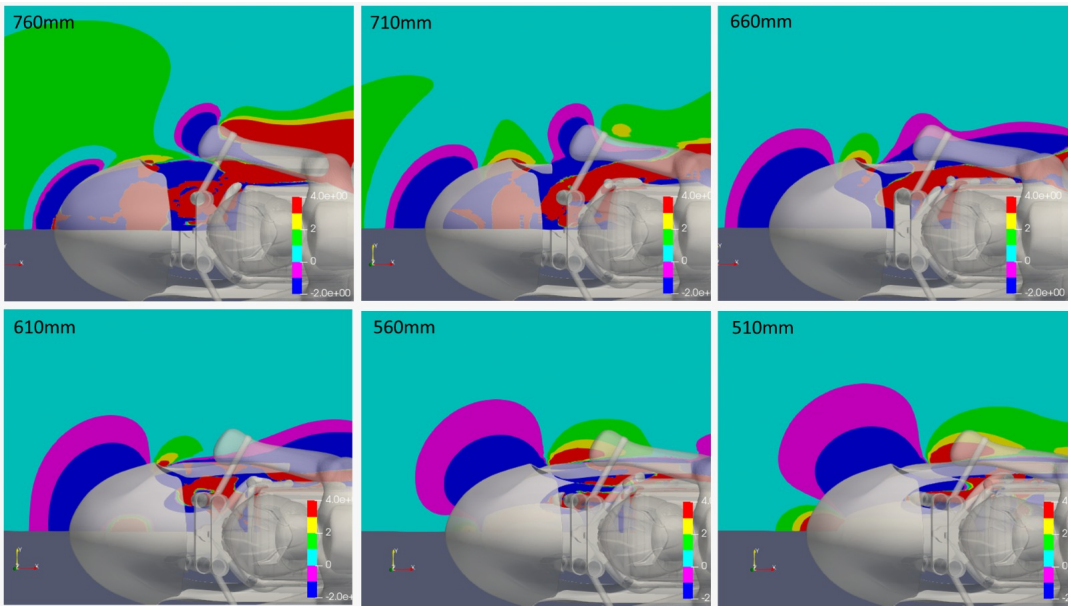

Figure 6.11: Sideslip angle contours around motorcycle on planes at different heights from the ground

We can notice that it is difficult to find a region of constant side angle. However it is possible to consider an averaged side angle, giving more importance to the zone in which endplates are placed. A very similar difficulty was found also for the fairing induced angle of attack, in figure 6.12

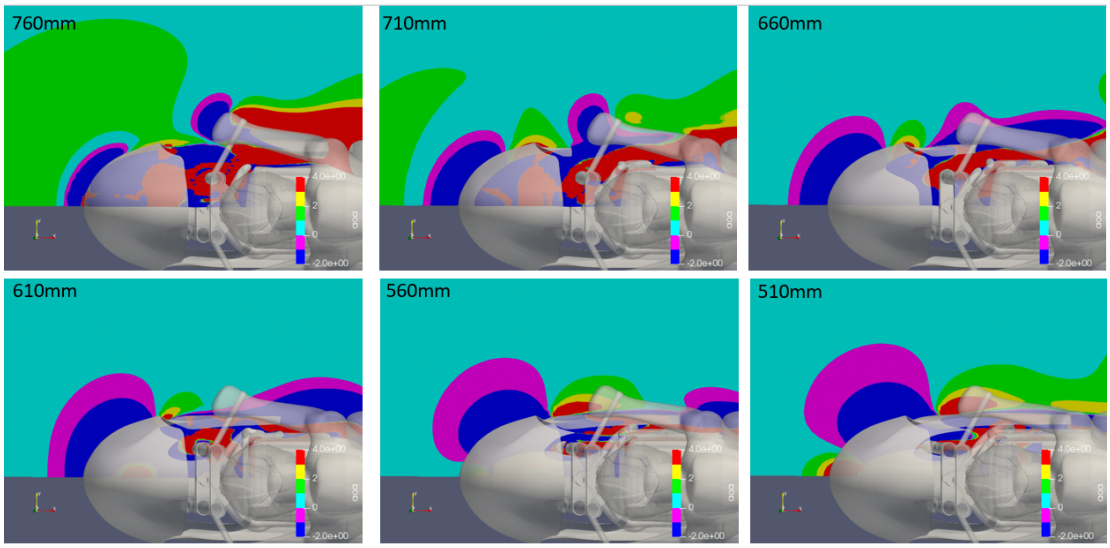

Figure 6.12: Induced angle of attack contours around motorcycle on planes at different heights from the ground

In some cases was not possible to place the winglets in the highest p_{tot} zone because

fairings terminate before. An example is that of figure 6.13 in which at 760mm from the ground winglets are obliged to stay ahead.

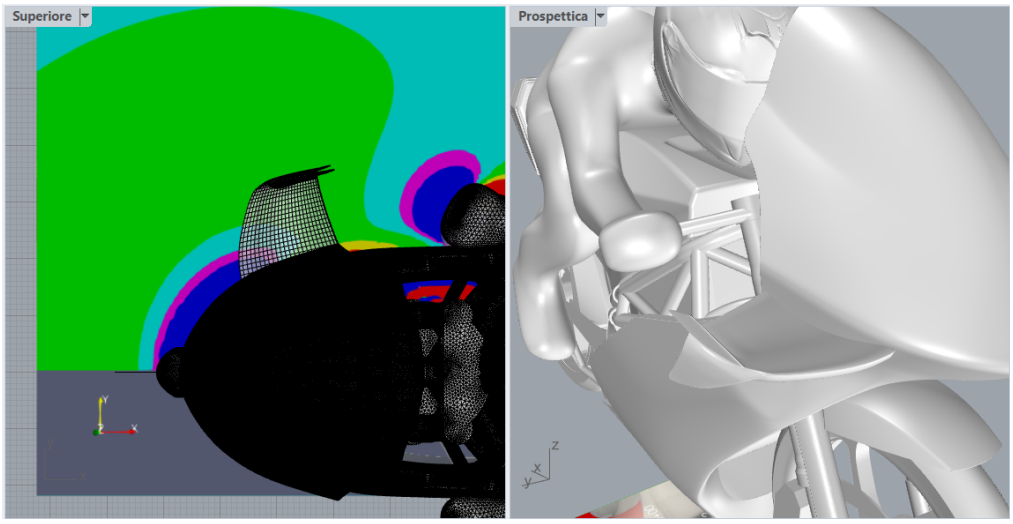

Figure 6.13: Winglet placement at 760mm high from the ground

We can notice also that the winglet has been rotated along z-axis to compensate the side angle.

In the Table 6.4 all the results obtained are collected, in particular the overall aerodynamic coefficients of the whole bike and of isolated winglets, varying the mounting height. The cases shown in the previous images for the 510mm and 550mm heights were not even taken into account since the ground clearance would have limited the rider in terms of lean angle.

height	Cl	Cd	Cl wing	Cd wing
without	-0.045	0.43	-	-
610	-0.27	0.47	-1.92	0.421
660	-0.25	0.48	-1.88	0.421
710	-0.15	0.46	-1.39	0.338
760	-0.17	0.46	-1.52	0.354

Table 6.4: motorbike with winglets

More interesting solution is the one obtained fixing the winglets at 610mm of height. In addition to force coefficient results, it is interesting to see how winglets modify whole motorbike aerodynamic.

We can see from streamlines visualization of figure 6.14b how winglets upwash deflects upward the flow, making it converge behind the tail.

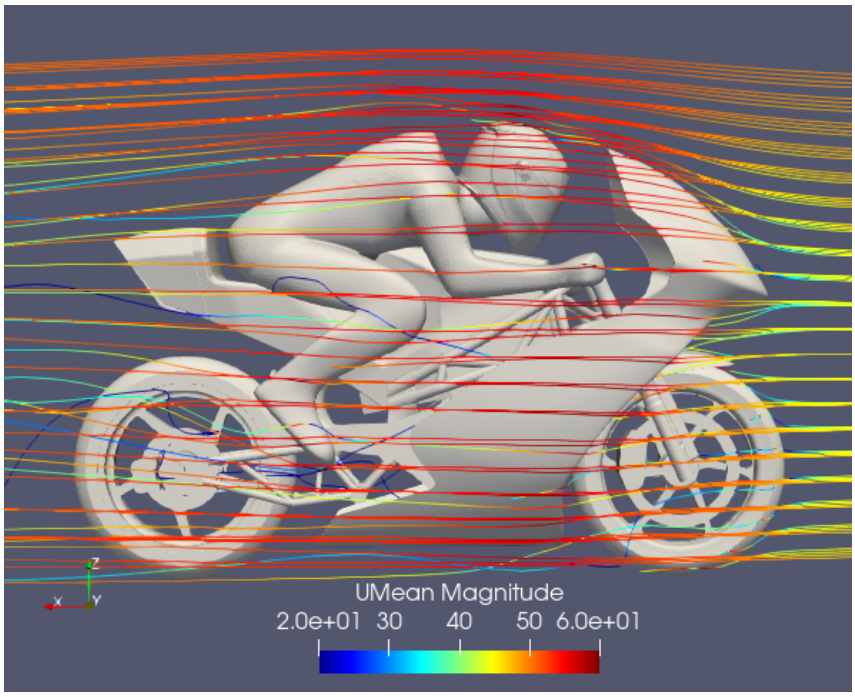

(a) base motorbike

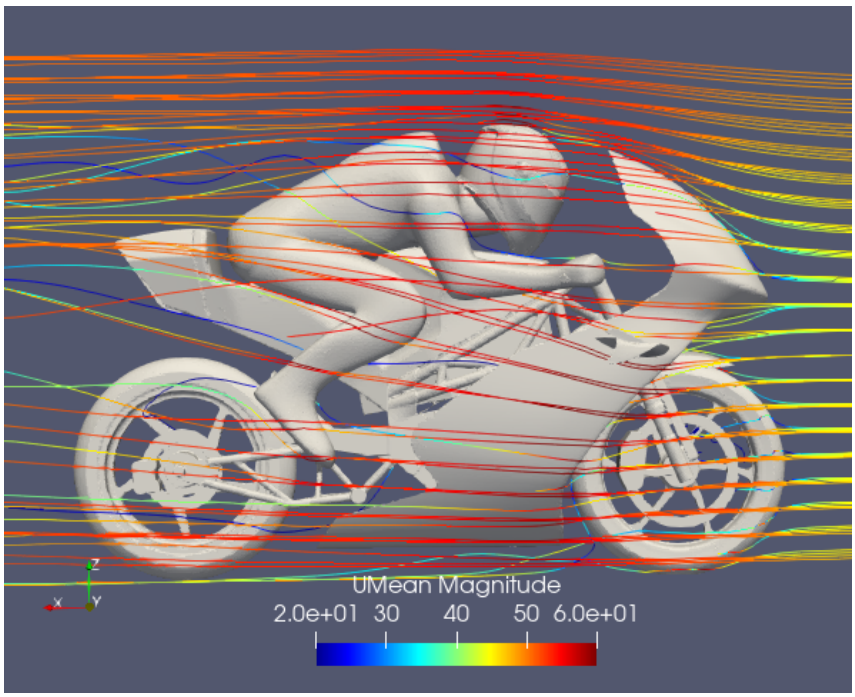

(b) motorbike with winglets

Figure 6.14: Streamlines visualization comparison around motorbike

This streamlines deflections reflects in a modification of the wake, as observable in figure

below, where we plotted, on a plane placed 3m behind the rear wheel pin, the contour of vorticity.

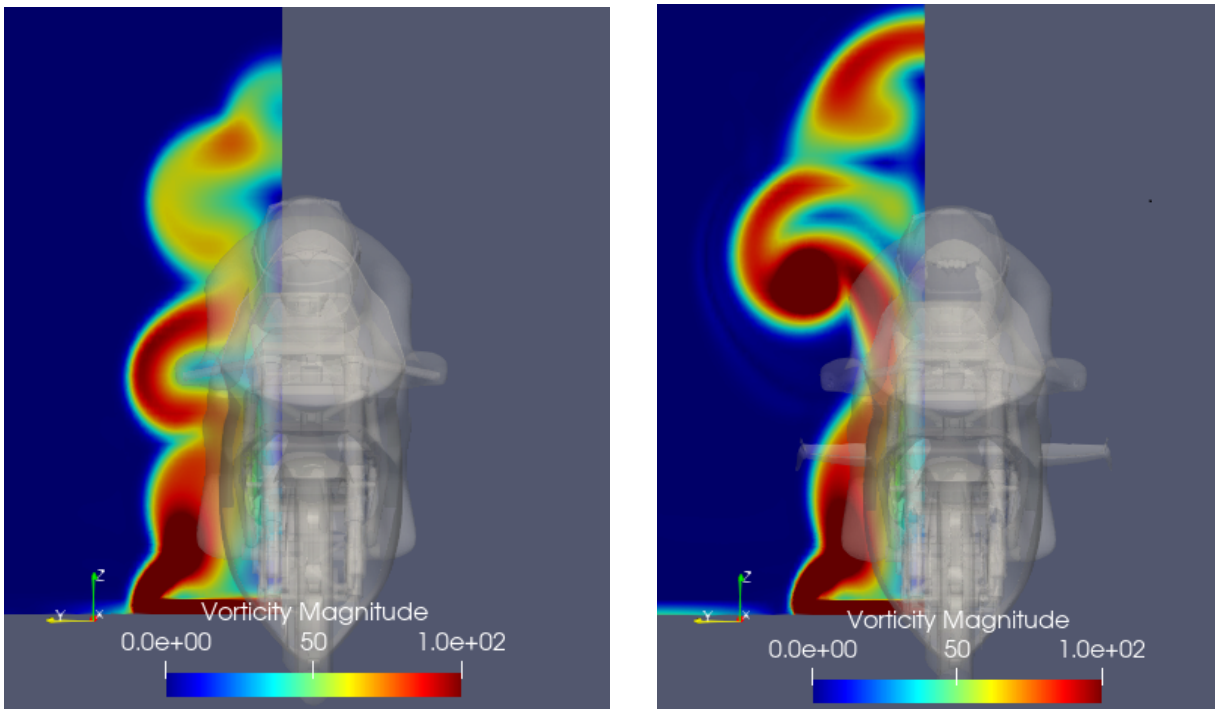

(a) base motorbike (b) motorbike with winglets

Figure 6.15: Wake vorticity comparison on a plane behind the motorcycle

We can see that winglets make the wake narrower in the zone behind the pilot and tends to move the wake upward. This can be an advantage because during competition, in particular during long straight, it is common practice to use the wake of the bike in front to decrease drag force. Produce an higher wake does not impact directly on performance but reduce reduces that of opponents. Finally we can see that the whole wake is dominated by the wing tip vortex. From that, we can understand that winglets could be optimized, instead of to maximize the lift, to control wake shape, reducing in size or moving where is convinient.

6.2.3. Cornering

As described in section 2.3.4 no advantages can be obtained from winglets at mid-corner if, during cornering, they behave as in rectilinear motion. Our work focus on determine if it is feasable to obtain, correctly placing the winglets, an interaction between with the pilot. To do so we had to make some adjustments to our model. First of all, the bike was tilted 50 degrees from the vertical, and consequently the rider's position in the saddle

was changed drastically to suit the case (Figure 6.16). We did not limit in move the pilot but we re-draw it using Human builder function of Catia. In addition, since motorbike no longer lies on vertical plane, the symmetry of the problem is lost, therefore we had to use the entire domain. In next figure is depicted the leaned bike and the pilot position.

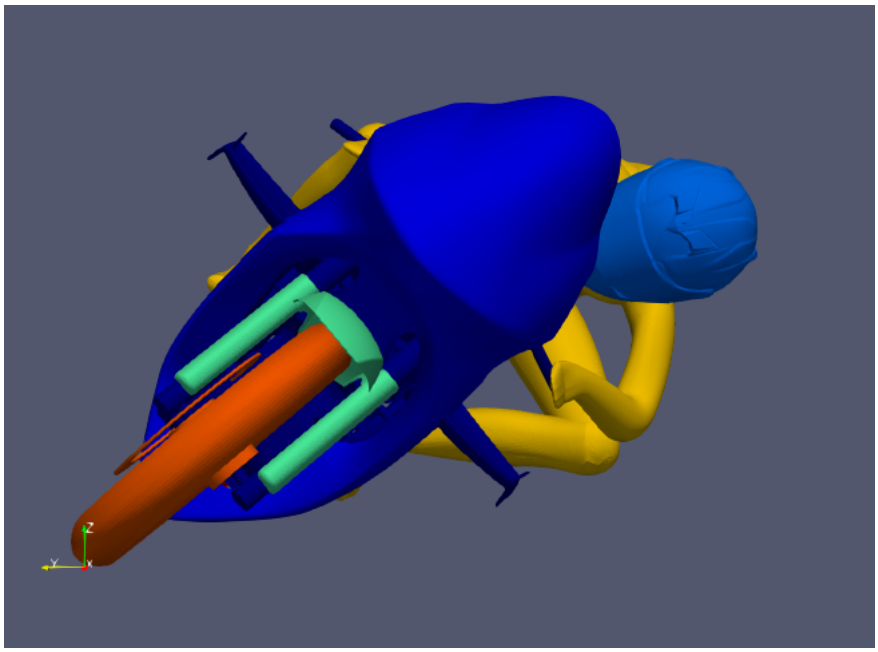

Figure 6.16: leaning bike geometry

Before proceeding testing the winglets we decide to repeat the study on total pressure did for placement choice, in figure 6.10. In this way we can analyze if some locking occurs.

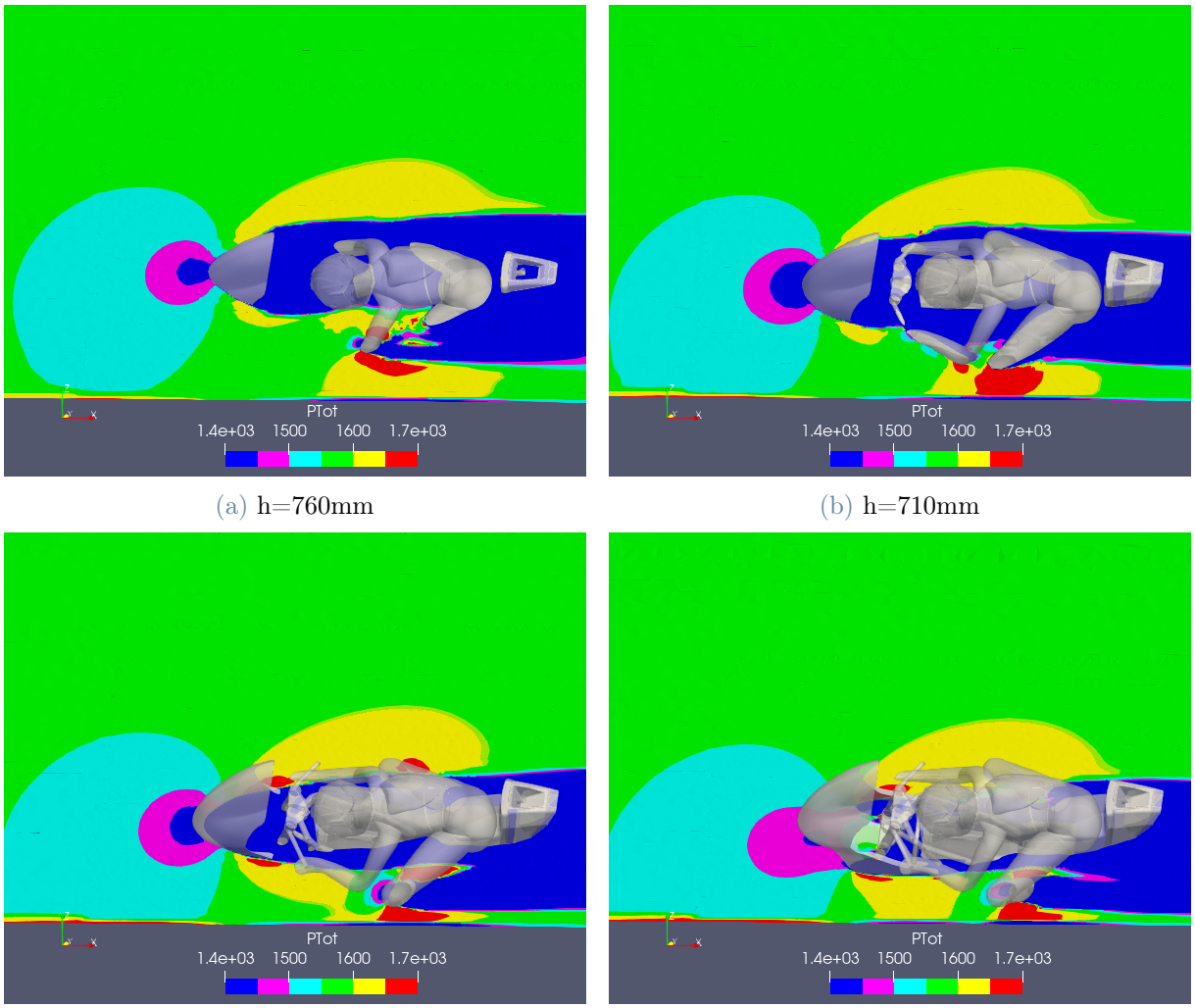

(a) h=760mm (b) h=710mm

(c) h=660mm (d) h=610mm

Figure 6.17: p_{tot} contours around the motorcycle in cornering condition on planes at different heights above the ground

From this study, we can see that the only zone in which pilot consistently reduce the total pressure is the rear zone, in the wake. A very little reduction is visible also in the front of the knee at an height of 660mm but however is not exploitable because

- its extension is not sufficient to cover winglet planform
- the winglets in that position would disturb the pilot's movements.

This analysis showed us that installing winglets with a dihedral angle, as proposed in the work done by Vojtech Sedla [25], would not produce any advantages so we have maintained the position unchanged as in figure 6.5. In the Table 6.5 below, the aerodynamic

coefficients of the entire motorbike with and without winglets are collected; they have also been written in body axes, thus following the 50-degree rotation with respect to the x-axis.

	ground axes			body axes	
	Cl	**Cd**	**Clat**	**Cl**	**Cd**
without winglets	0.12	0.73	0.00	0.08	0.73
with winglets	0.00	0.74	0.08	-0.06	0.74

Table 6.5: aerodynamic coefficient in cornering

In the two figures 6.18 below, we plotted streamlines in the area adjacent to the fin positioned in the inner part of the corner to confirm the absence of interaction between the wing and the pilot.

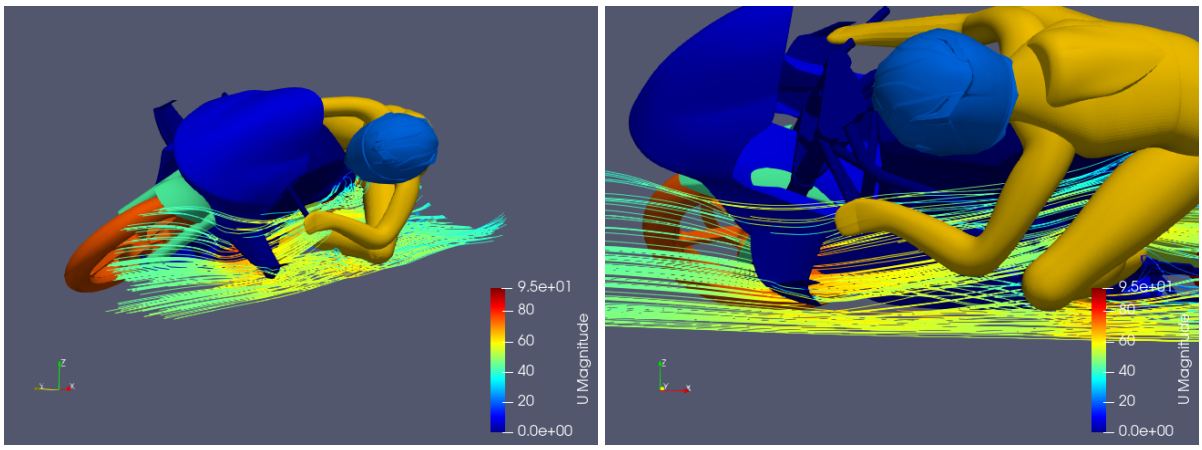

Figure 6.18: streamlines visualization around internal motorbike winglet during cornering motion

6.2.4. Aerodynamic results applied to dynamic model and lap time simulator

We now apply aerodynamic results just presented at dynamic model discussed in chapter 2. Motorbike chosen for the final test is the high power one. In contrast to previous, aerodynamic coefficients differ from straight and cornering motion.

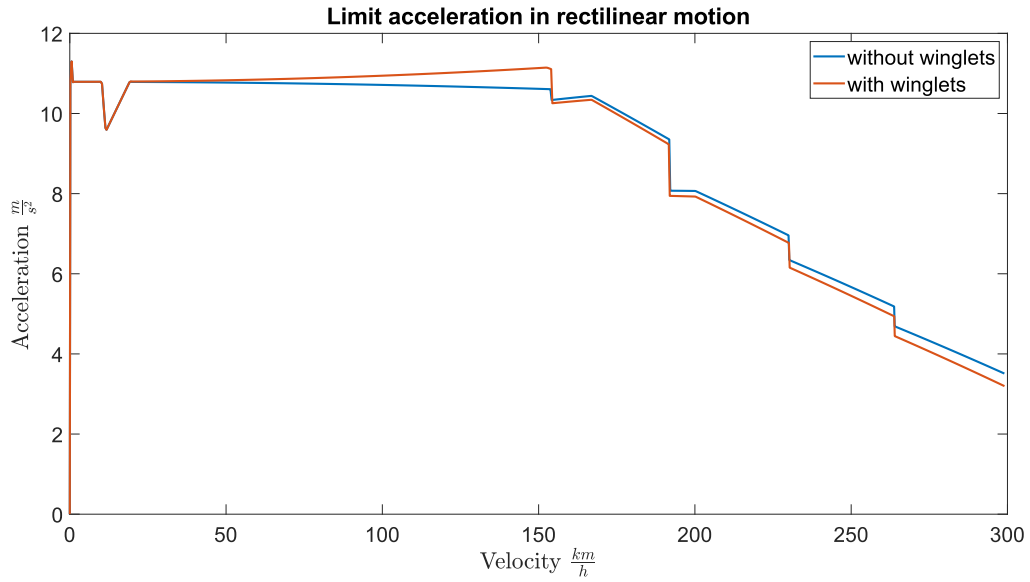

Figure 6.19: Limit acceleration during rectilinear motion

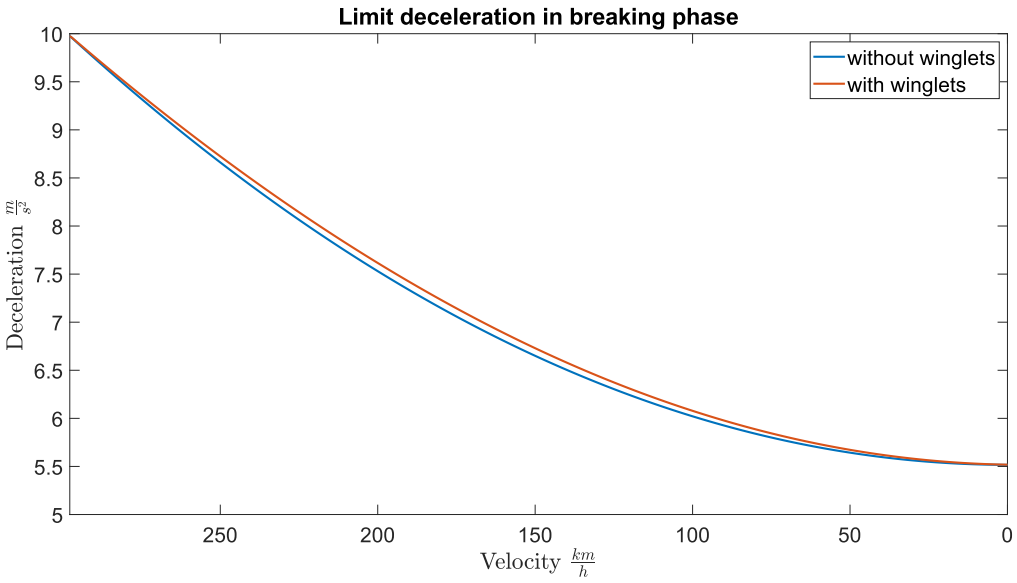

Figure 6.20: Limit deceleration during rectilinear motion

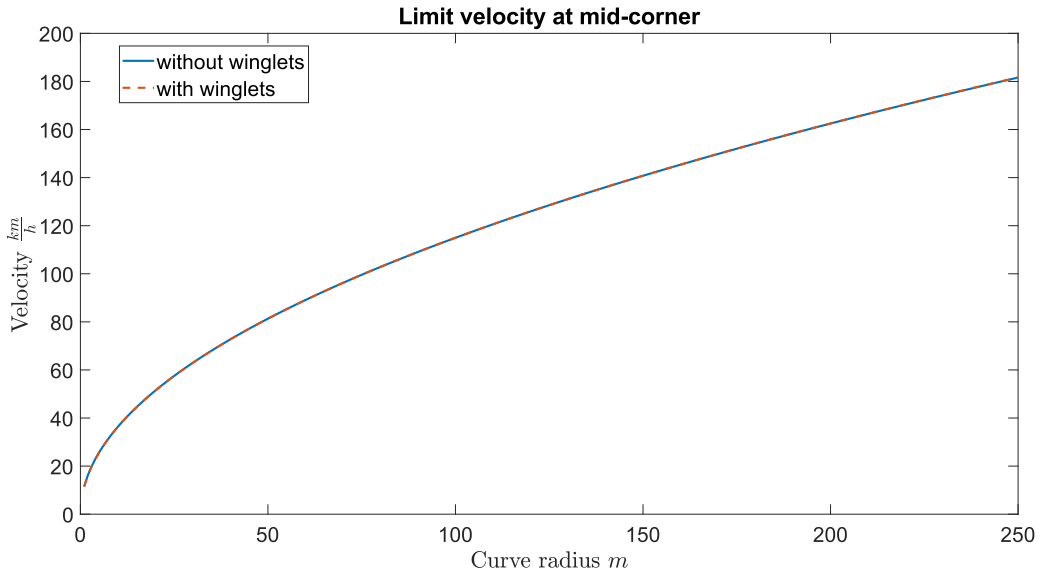

Figure 6.21: Limit velocity at mid-corner

Similar considerations to the ones done so far in chapter 2 can be done here with calculated aerodynamic coefficients: we can see a speed range, till about 150 km/h, in which a consistent improvement was achieved. Going to higher speed instead, the drag addition reduces maximum acceleration. However an increase in handling and stability could be obtained. Stability analysis is beyond the scope of our studies, however we report below, in figure 6.22 the comparison between front, rear and total wheel loads on both configuration, with and without winglets.

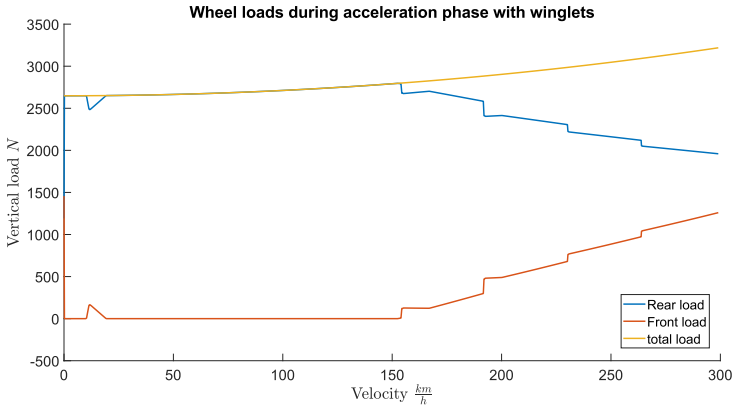

(a) With winglets

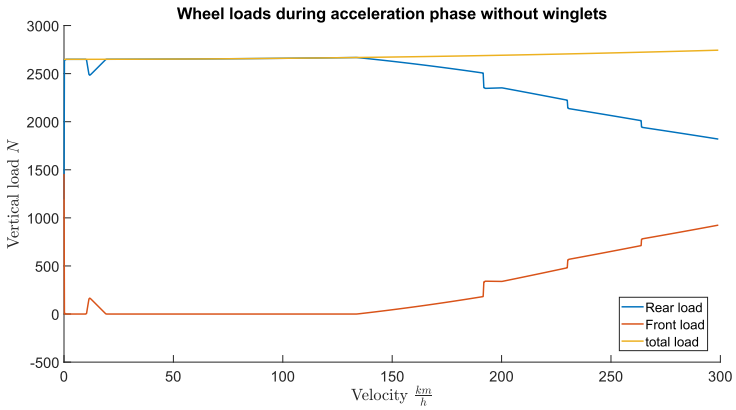

(b) Without winglets

Figure 6.22: Comparison between wheel loads on motorbike with and without wings

During braking phase instead we got an improvement at all speed and during cornering any changes can be observed. From this plots it is not clear if some advantages can be obtained by installing this winglets. For this reason it was necessary to implement the lap time simulator described in chapter 2.
As said before, we choose Mugello circuit as test track because it is a very fast circuit, and, as visible in figure 6.19 high speed represent the most critical condition. Despite the unfavorable conditions we obtain an estimated lap time reduction of 0.4s, results that, in motorcycle racing, is a very good result.

7 | Conclusions and future developements

The objective of this thesis was to analyze the actual contribution made by the introduction of aerodynamic winglets on the fairings of a race bike. This work was divided into four basic steps that give way to the main chapters of the thesis: the choice of the most appropriate aerodynamic profile, the design of a finite wing following well-fixed targets, the study of the aerodynamics of the entire motorcycle, and the integration of the latter into a simplified dynamic model. All fluid dynamic analyses were carried out by CFD simulations using OpenFOAM^{TM}, while the design and engineering part was done with the help of CAD modeling software including Rhino and Catia. In the first phase, we set ourselves the goal of finding an aerodynamic profile appropriate for motorsport. In fact, the airfoil must have good performance for low Reynolds numbers, a lift curve at varying angle of attack that is quite smooth, with high lift values and a soft stall characteristics. After comparing by means of CFD simulations, the performance of three airfoils the choice fell on the mshd profile, previously developed following aft loading as the direction that maximize downforce, while still maintaining a level of concave pressure recovery that ensures stability under different operating conditions and 'soft stall' characteristics. After this first preliminary phase, we moved to three-dimensional analysis, studying the influence of the profile for low aspect ratio wings, we specifically saw an overall decrease in performance. Having fixed the chord and geometry of the mshd profile, we moved on to the design of the actual wing. At this stage, multiple geometric aspects were considered, with the main intent of maximizing downforce. In particular, we found a decrease in drag by changing the Taper Ratio and an increase in lift by changing the planform of the wing. Working on the sweep angle, on the other hand, did not show any noteworthy trends, since this usually has more influence in the transonic range. Finally, the influence of endplates of different shape and size was studied, but unlike wings with higher Aspect Ratio, the tip vortex is still dominant. CFD simulations on the whole motion were divided as follows: Once the validation of the data of the motorcycle without a rider was finished, comparing the data with the wind tunnel at Politecnico di Milano , the motorcycle with

the addition of the rider was analyzed in straight and leaning motion. Regarding the straight bike, with the adoption of winglets there was a noticeable increase in downforce and an inevitable increase in drag, looking at the wake vorticity also shows an upward shift of the most vortical zone, this aspect may bother competing riders to take advantage of the wake and overtake. During cornering there was no particular benefit, moreover the idea of the locking effect of the inner wing to disable its aerodynamics in our case does not occur at all. Finally, the simplified dynamic model with the integration of aerodynamics summarized the results by showing that, with the adoption of the winglets, there are excellent benefits in acceleration and braking, especially if the bike is more engine-performing. In cornering, on the other hand, no improvement is noticeable. Considering the fact that on a track the acceleration and braking phases are numerous, simulating a circuit with the simplified lap time simulator, the adoption of fins led to the reduction of about 5 tenths of a second in terms of lap time. Finally, we would like to provide some advice and improvements to be adopted for further development. Regarding our motorbike numerical model, it would be advisable to modify the aerodynamic model used for the motorcycle with the introduction of an accurate model for wheels rotation. Moreover the availability of a 3D scan of the rider would allow for more accurate modeling of the rider in both straight and cornering motion. Regarding winglets design, we limited our study, not analyzing all possible parameters and analyzing them separately, considering them as they were fully independent. Furthermore, once installed on the fairings a local optimization through adjoint method could take some advantages that can not be considered studying the winglets simply attached to a flat plate.
Regarding dynamic model there is a lot of room for improvement, for example

- considering all rotational inertia contributions
- introducing a more accurate tyre model such as Pacejka tire model
- introducing suspension damping
- modeling the system not only at mid corner but in all phase of cornering motion

Bibliography

[1]

[2] J. D. Anderson. *Fundamentals of aerodynamics*. McGraw-Hill, 5th edition, 2011. ISBN 0073398101.

[3] G. Angle. Aerodynamic drag reduction of a racing motorcycle through vortex generation. 09 2003. doi: 10.4271/2003-32-0037.

[4] R. A. Baurle. Modeling of high speed reacting flows: Established practices and future challenges. 2004.

[5] T. Cebeci and J. Cousteix. Modeling and computation of boundary-layer flows: Laminar, turbulent and transitional boundary layers in incompressible flows. 1998.

[6] I. C. Cheeseman. Fluid-dynamic lift. dr.-ing s. f. hoerner and h. v. borst. dr.-lng s. f. hoerner and h. v. borst hoerner fluid dynamics, brick town. 1975. 499 pp. illustrated. £29.20. *The Aeronautical Journal (1968)*, 81(798):276–277, 1977. doi: 10.1017/S0001924000032784.

[7] G. M. Cole and T. J. Mueller. Experimental measurements of the laminar separation bubble on an eppler 387 airfoil at low reynolds numbers. 1990.

[8] V. Cossalter. *Motorcycle dynamics*. Lulu, 2nd edition, 2006. ISBN 9781447532767.

[9] R. Dagur, V. Singh, S. Grover, N. Sethi, and B. Arora. Design of flying wing uav and effect of winglets on its performance. *Int J Emerg Technol Adv Eng*, 8(3), 2018.

[10] L. Davidson. Fluid mechanics, turbulent flow and turbulence modeling. 2020.

[11] M. G. el Hak. Control of low-speed airfoil aerodynamics. *AIAA Journal*, 28:1537–1552, 1990.

[12] R. A. Eppler. Turbulent airfoils for general aviation. *Journal of Aircraft*, 15:93–99, 1978.

[13] D. Fintelman, H. Hemida, M. Sterling, and F.-X. Li. A numerical investigation of

the flow around a motorbike when subjected to crosswinds. *Engineering Applications of Computational Fluid Mechanics*, 9:528 – 542, 2015.

[14] M. Genç, G. Özkan, H. Açikel, M. Kiriş, and R. Yildiz. Effect of tip vortices on flow over naca4412 aerofoil with different aspect ratios. *EPJ Web of Conferences*, 114: 02027, 01 2016. doi: 10.1051/epjconf/201611402027.

[15] InSella. 2021 ducati desmosedici gp. URL `https://immagini.insella.it/sites/default/files/news_anteprima/2021/05/miller_1.jpg`.

[16] J. Katz. High-lift wing design for race-car applications. *SAE transactions*, 104: 2822–2828, 1995.

[17] J. G. Lowry and E. C. Polhamus. A method for predicting lift increments due to flap deflection at low angles of attack in incompressible flow. 1957.

[18] J. G. Lowry and E. C. Polhamus. A method for predicting lift increments due to flap deflection at low angles of attack in incompressible flow. 1957.

[19] K. W. Mcalister and R. Takahashi. Naca 0015 wing pressure and trailing vortex measurements. 1991.

[20] F. R. Menter. Two-equation eddy-viscosity turbulence models for engineering applications. *AIAA Journal*, 32:1598–1605, 1994.

[21] F. R. Menter, M. Kuntz, and R. Langtry. Ten years of industrial experience with the sst turbulence model. 2003.

[22] M. Palanivendhan, D. Nagpal, D. Rao, J. Philip, and M. Ganapathi. Design and analysis of an aerodynamic kit for a two wheeled race motorcycle. *Materials Today: Proceedings*, 45, 03 2021. doi: 10.1016/j.matpr.2021.02.635.

[23] L. Quartapelle and F. Auteri. *Fluidodinamica incomprimibile*. Casa Editrice Ambrosiana, 2013. ISBN 8808185397.

[24] S. Sathaye, J. Yuan, and D. Olinger. Lift distributions on low-aspect-ratio wings at low reynolds numbers for micro-air vehicle applications. volume 1, 08 2004. ISBN 978-1-62410-025-3. doi: 10.2514/6.2004-4970.

[25] V. Sedlák. Motorcycle cornering improvement : An aerodynamical approach based on flow interference. 2012.

[26] M. S. Selig and J. J. Guglielmo. High-lift low reynolds number airfoil design. *Journal of Aircraft*, 34:72–79, 1997.

[27] M. S. Selig and M. D. Maughmer. Generalized multi-point inverse airfoil design. 1991.

[28] B. Simon, V. Cossalter, M. Massaro, and M. Peretto. Application of the "optimal maneuver method" for enhancing racing motorcycle performance. *SAE International Journal of Passenger Cars - Mechanical Systems*, 1, 04 2008. doi: 10.4271/2008-01-2965.

[29] J. C. Sivells and R. H. Neely. Method for calculating wing characteristics by lifting-line theory using nonlinear section lift data. 1947.

[30] A. Somerville, M. Marino, G. Baxter, and G. Wild. Understanding box wing aircraft: essential technology to improve sustainability in the aviation industry. *Aviation*, 20: 129–136, 07 2016. doi: 10.3846/16487788.2016.1195076.

[31] P. R. Spalart. A one-equation turbulence model for aerodynamic flows. 1992.

[32] R. F. Spivey. Blade tip aerodynamics-profile and planform effects. 1968.

[33] P. Sriram, A. Gopalarathnam, and A. Misenheimer. High-downforce airfoil design for motorsports. *SAE International Journal of Materials and Manufacturing*, 5:478–489, 2012.

[34] G. E. Torres and T. J. Mueller. Low aspect ratio aerodynamics at low reynolds numbers. *AIAA Journal*, 42(5):865–873, 2004. doi: 10.2514/1.439. URL `https://doi.org/10.2514/1.439`.

[35] C. Y. Tung, S. L. Pucci, F. X. Caradonna, and H. A. Morse. The structure of trailing vortices generated by model rotor blades. 1981.

[36] T. Van Dijck. Computational evaluation of aerodynamic forces on a racing motorcycle during high speed cornering. 2015, 03 2015. doi: 10.4271/2015-01-0097.

[37] D. Viieru, R. Albertani, W. Shyy, and P. G. Ifju. Effect of tip vortex on wing aerodynamics of micro air vehicles. *Journal of Aircraft*, 42(6):1530–1536, 2005.

[38] R. T. Whitcomb. A design approach and selected wind tunnel results at high subsonic speeds for wing-tip mounted winglets. 1976.

[39] D. C. Wilcox. Formulation of the k-omega turbulence model revisited. 2007.

[40] F. Wortmann. The quest for high-lift. 1974.

A | Lifting-line theory

The first attempt to quantitatively model such a phenomena was made by Prandtl with the classical lifting-line theory. He modeled the wing and the downstream wake as a large number of horseshoe vortex placed side by side as shown in figure A.1, forming a main vortex, named bounded vortex, responsible for the lift, and a large number of free vortex in the wake.

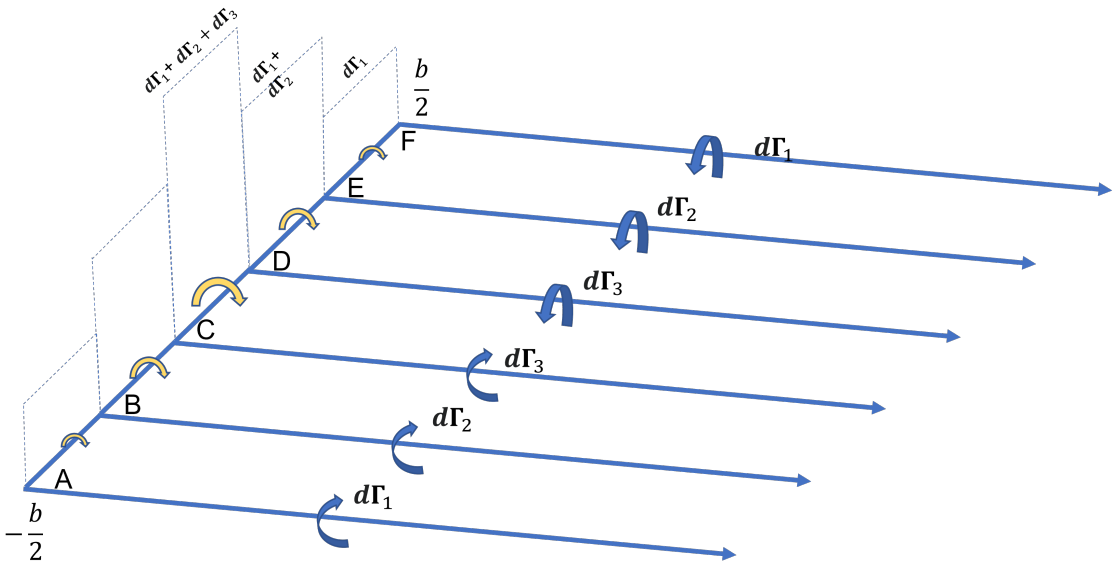

Figure A.1: Horseshoe vortex of lifting line theory

We can notice, in agreement with Helmoltz theorem, that the variation of circulation in the lifting line is due to a variation in the wake, according to equation (A.1).

$$\Gamma\left(z+\Delta \mathrm{z}\right)-\Gamma\left(z\right)=-\gamma_{wake}\left(z\right)\Delta \mathrm{z} \tag{A.1}$$

Taking the limit for Δz tends to 0 we obtain

$$\frac{d\Gamma\left(z\right)}{dz}=-\gamma_{wake}(z) \tag{A.2}$$

Once we obtained the equation that link wake circulation with lifting-line circulation we had to find an equation to find $\Gamma(z)$. In order to do that, we had to introduce some hypothesis: firs of all we suppose that, at each section of the wing, 2d thin airfoil theory is applicable.
We can now write an equation for $c_l(z)$:

$$c_l(z) = 2\pi \left[\alpha_{EFF}(z) - \alpha_{l=0}(z)\right] \tag{A.3}$$

in which α_{EFF} is the effective angle.// Introducing a second hypothesis for which both the angle of attack both the induced angle could be retained small so that

$$\alpha_{ind}(z) \approx \frac{v_{ind}(z)}{U_\infty} \tag{A.4}$$

in which U_∞ is the freestream velocity, and introducing the Kutta-Jukowski theorem we get

$$\frac{\Gamma(z)}{\pi |U(z)| C(z)} + \frac{v_{ind}(z)}{U_\infty} = -\alpha(z) + \alpha_{l=0}(z) \tag{A.5}$$

To estimate $v_{ind}(z)$ we can integrate the equation for rectilinear vortexes and obtain

$$v_{ind}(z) = \frac{1}{4\pi} \int_{-\frac{b}{2}}^{\frac{b}{2}} \frac{d\Gamma(\xi)}{d(\xi)} \frac{d\xi}{z-\xi} \tag{A.6}$$

From equation (A.5) and equation (A.6) arise the lifting line equation of Prandtl and Lanchester: [23]

$$\frac{\Gamma(z)}{\pi |U(z)| C(z)} + \frac{1}{4\pi U_\infty} \int_{-\frac{b}{2}}^{\frac{b}{2}} \frac{d\Gamma(\xi)}{d(\xi)} \frac{d\xi}{z-\xi} = -\alpha(z) + \alpha_{l=0}(z) \tag{A.7}$$

We notice that eq. A.7 is a integral-differential equation because the unknown $\Gamma(z)$ is present inside the integral as a derivative. Boundary conditions have to be imposed at the extremes of the wing. From a physical point of view the correct conditions are that the circulation becomes zero to the extremes.
Once $\Gamma(z)$ is solved it is possible to find the induced AoA that is responsible for induced drag.

$$\alpha_{ind}(z) = \frac{1}{4\pi U_\infty} \int_{-\frac{b}{2}}^{\frac{b}{2}} \frac{d\Gamma(\xi)}{d(\xi)} \frac{d\xi}{z-\xi} \tag{A.8}$$

Due to this induced angle lift and drag directions become rotated and the horizontal

component of the lift, that will be opposed to wing direction, is called induced drag.

$$d_{ind}(z) = -l(z)\sin\alpha_{ind}(z) \approx -l(z)\alpha_{ind(z)} = \rho U\Gamma(z)\alpha_{ind}(z) \tag{A.9}$$

By integrating along the span eq A.9 and dividing by dynamic pressure it is possible to find the induced drag coefficient:

$$Cd_{ind}(z) = \frac{2}{US}\int_{-b/2}^{b/2}\Gamma(z)\alpha_{ind}(z)dz \tag{A.10}$$

Particular attention was given to the case of elliptical circulation distribution in which the circulation distribution is prescribed by following equation: A.11

$$\Gamma(z) = \Gamma_0\sqrt{1-\left(\frac{2z}{b}\right)^2} \tag{A.11}$$

Main properties of this kind of wing are:

- the downwash, and so the induced angle, are constant along the span
- the induced drag coefficient is proportional to the square of the lift coefficient and inversely proportional to the AR, accordingly to the following equation

$$Cd_{ind} = \frac{Cl^2}{\pi AR} \tag{A.12}$$

General lift distribution can be treated considering the transformation A.13

$$z = \frac{-b}{2}\cos\theta \tag{A.13}$$

and writing the general circulation distribution as a Fourier sine series A.14

$$\Gamma(\theta) = 2bU_\infty\sum_{n=1}^{N}A_n\sin n\theta \tag{A.14}$$

replacing this expression for the circulation into the Prandtl-Lanchester equation we get:

- $$Cl = A_1\pi AR \tag{A.15}$$

- $$Cd_{ind} = \pi AR\ A_1^2 \left[1 + \sum_2^N n \left(\frac{A_n}{A_1}\right)^2\right] = \frac{C_L^2}{\pi AR}(1+\delta) = \frac{C_L^2}{\pi eAR} \tag{A.16}$$

in which $e \leq 1$ is named Oswald efficiency. [2] Looking at equation A.12 we can notice the importance of elliptical wing in which $e = 1$ and so it can be taken as reference for the efficiency of the wing.
Another interesting parameter, as mentioned before, is the slope of the lift curve. We define Cl_α as $dCl/d\alpha$ that from lifting line theory results to be

$$Cl_\alpha = \frac{a_0}{1 + (a_0/\pi AR)(1+\tau)} \tag{A.17}$$

where a_0 is the lift slope of 2d airfoil section.

B | Navier-Stokes equations

The governing equations, which describe the behavior of a generic viscous fluid, are called Navier-Stokes equations (or balance equations) and represent a set of partial derivative differential equations, which are supplemented by appropriate boundary conditions and initial conditions. They consist of: continuity equation: expresses the principle of conservation of mass momentum balance equation: expresses the change in momentum due to the action of the resulting motion due to the action of the resultants of external forces energy balance equation: states that, the change in the unit time of the total energy of the fluid, contained in the control volume, added to the net flow of total energy across the faces of the control volume, equals the sum of the power of the forces acting on the fluid element and the net flow of thermal energy transmitted to the fluid element by conduction If the fluid is assumed Newtonian, the equations in differential form reduce to:

- $$\frac{\partial \rho}{\partial t} + \frac{\partial(\rho u_i)}{\partial x_i} = 0 \tag{B.1}$$

- $$\frac{\partial(\rho u_i)}{\partial t} + \frac{\partial[\rho u_i u_j]}{\partial x_j} = \frac{\partial \sigma_{ij}}{\partial x_i} \tag{B.2}$$

- $$\frac{\partial(\rho E)}{\partial t} + \frac{\partial \rho u_i H}{\partial x_j} = \frac{\partial(\tau_{ij} u_i)}{\partial x_j} + \frac{\partial}{\partial x_i}(k\frac{\partial T}{\partial x_j}) \tag{B.3}$$

The spatial variable is xi , is the density, ui is the velocity vector, E is the total energy, H is the total enthalpy, k is the thermal conductivity coefficient, ij is the stress tensor viscous and T is the temperature.

The equations defining energy and enthalpy are:

$$E = e + \frac{1}{2} u_i u_i \tag{B.4}$$

$$H = h + \frac{1}{2} u_i u_i \tag{B.5}$$

where e is the internal energy per unit mass and h the entalphy. The term σ_{ij} represents the stress tensor, which can be separated into a conservative part and a dissipative term:

$$\sigma_{ij} = -p\delta_{ij} + \tau_{ij} \tag{B.6}$$

where $-p_{ij}$ is the thermodynamic pressure tensor. In most fluids, viscous stresses depend almost entirely on the rate of deformation. A fluid in which the viscous stress tensor is assumed proportional to that parameter is called a Newtonian fluid: τ_{ij} s_{ij} with:

$$s_{ij} = \frac{1}{2}(\frac{\partial u_i}{\partial x_j} + \frac{\partial u_j}{\partial x_i}) \tag{B.7}$$

Including the viscosity coefficients and considering all components of the stress tensor viscous and the velocity of strain tensor, the proportionality bond is given as: $\tau_{ij} = C_{ijkl}$ S_{kl} where C_{ijkl} is a fourth-order tensor containing the viscosity coefficients. Assuming isotropy of the fluid, it is possible to state that the latter term contains only two coefficients (μ and λ, of the first and second order, respectively). Therefore, the previous constitutive relation is simplified to:

$$\tau_{ij} = 2\mu s_{ij} + \lambda s_{mm}\delta ij \tag{B.8}$$

with:

$$s_{mm} = \frac{\partial u_m}{\partial x_m} \tag{B.9}$$

$$\lambda = -\frac{2}{3}\mu \tag{B.10}$$

and then:

$$\tau_{ij} = 2\mu s_{ij} - \frac{2}{3}(\mu s_{mm})\delta_{ij} \tag{B.11}$$

In the case of incompressible flows, the density ρ is constant and the governing equations are simplified. On the other hand, if compressibility is considered, the equation of state must be taken into account:

$$\rho = \frac{p}{\frac{R}{M}T} \tag{B.12}$$

where the temperature T is obtained by solving the energy equation.